

V<sub>p</sub>/V<sub>s</sub> ESTIMATION FROM MULTICOMPONENT SEISMIC DATA  
FOR IMPROVED CHARACTERIZATION OF A TIGHT  
SANDSTONE GAS RESERVOIR,  
RULISON FIELD, COLORADO

by  
Eldar Guliyev

A thesis submitted to the Faculty and the Board of Trustees of the Colorado School of Mines in partial fulfillment of the requirements for the degree of Master of Science (Geophysics).

Golden, Colorado

Date 01/24/07

Signed: \_\_\_\_\_



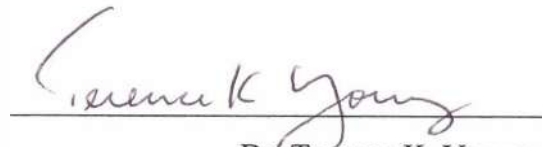
Eldar Guliyev

Approved: \_\_\_\_\_



Dr. Thomas L. Davis

Thesis Advisor



Dr. Terence K. Young

Department Head

Geophysics

## **ABSTRACT**

My thesis focuses on building and implementing a workflow for velocity ratio -  $V_p/V_s$  volume estimation. This research emphasizes the use of both pure shear and converted wave data for  $V_p/V_s$  estimation through traveltime calculations resulting in interval  $V_p/V_s$  and the impedance inversion of seismic reflectivity introducing high resolution  $V_p/V_s$ .

Impedance inversion and  $V_p/V_s$  estimations provide valuable information for improved reservoir characterization. The stack of producing sandstones and their general trend in the investigated reservoir is described and modeled by the high resolution velocity ratio volumes. The presented methodology produces robust outcomes, as seismic derived  $V_p/V_s$  is well correlated with log derived  $V_p/V_s$ .

$V_p/V_s$  velocity ratio is a determinant of reservoir rock quality in the tight gas sandstone environment. The presence of gas lowers the velocity ratio below 1.6. My estimates of  $V_p/V_s$  from multicomponent seismic data confirm this result. Analysis of obtained  $V_p/V_s$  volumes in combination with the results from other independent studies performed on the field data reveal a good agreement between reservoir rock quality and velocity ratio values.

## TABLE OF CONTENTS

ABSTRACT.....	iii
LIST OF FIGURES.....	viii
LIST OF TABLES.....	xix
ACKNOWLEDGMENTS.....	xx
 Chapter 1 INTRODUCTION.....	 1
1.1 Characterization And Production Challenges.....	1
1.2 Previous Studies Of the Vp/Vs Application.....	3
1.3 Research Objectives.....	6
1.4 Thesis Outline.....	7
1.5 Geological Setting Of The Piceance Basin.....	7
1.5.1 Piceance Mesaverde Williams Play.....	8
1.5.2 Petroleum System Of The Piceance Basin.....	9
1.5.3 Tectonic Evolution Of The Piceance Basin.....	9
1.6 The Study Area: Rulison Field.....	12
1.6.1 Production History.....	12
1.7 Seismic And Well Log Data Set.....	15
1.8 Seismic Data Quality.....	22

Chapter 2 METHODOLOGY FOR TRAVELTIME-BASED Vp/Vs ESTIMATION.....	30
2.1 Chapter Introduction.....	30
2.2 Workflow For Interval Vp/Vs Estimation.....	30
2.3 Well Correlation To Multicomponent Seismic Data.....	32
2.3.1 Well Tie Of PP Seismic Data.....	33
2.3.2 Well Tie Of SS Seismic Data.....	35
2.3.3 Well Tie Of PS Seismic Data.....	35
2.4 Interval Vp/Vs Estimation.....	38
2.5 Summary.....	39
Chapter 3 METHODOLOGY FOR SEISMIC IMPEDANCE INVERSION OF MULTICOMPONENT SEISMIC DATA.....	41
3.1 Chapter Introduction.....	41
3.2 Frequency Bandwidth Of The Seismic Data.....	41
3.3 Workflow For Impedance Derived Vp/Vs Estimation.....	43
3.4 Model-Based Inversion Technique.....	45
3.5 Compressional And Shear Wave Data Inversion.....	48
3.6 Converted Wave Data Inversion Trough Pseudo S-Impedance Estimation.....	53
3.6.1 Corrections For Pseudo S-Impedance From Differential Modeling.....	57
3.7 Summary.....	61

Chapter 4 METHODOLOGY FOR Vp/Vs ESTIMATION FROM IMPEDANCE INVERTED DATA.....	64
4.1 Chapter Introduction.....	64
4.2 High Resolution Vp/Vs Volume.....	64
4.2.1 Seismic Inversion As A Tool For High Resolution Vp/Vs Estimation .....	64
4.3 Vp/Vs Volume Calculation.....	65
4.4 Quality Test At A Distant Well.....	74
4.5 High Resolution Vp/Vs Failure As A Time Rescaling Tool.....	75
4.6 Summary.....	76
Chapter 5 ANALYSIS AND INTERPRETATION OF Vp/Vs RESULTS.....	79
5.1 Chapter Introduction.....	79
5.2 Interval Vp/Vs Interpretation.....	79
5.3 Impedance Derived Vp/Vs Interpretation.....	81
5.3.1 Three Dimensional Representation Of The Vp/Vs Results.....	84
5.3.2 Comparative Analysis Of Vp/Vs With Time-Lapse Observations.....	90
5.3.3 Depth Conversion.....	93
5.3.4 The Sensitivity Of Generated Vp/Vs Volumes To The Lithological Components Of The Reservoir.....	96
5.3.5 Data Slicing.....	100

5.3.6	Prospect Identification.....	113
5.4	Summary.....	114
Chapter 6	CONCLUSIONS AND RECOMMENDATIONS.....	121
6.1	Conclusions.....	121
6.2	Recommendations For Future Research.....	122
Appendix A	PSEUDO DENSITY DERIVATION FOR STRATIGRAPHIC INVERSION OF POSTSTACK PS CONVERTED WAVE DATA.....	124
REFERENCES	.....	128

## LIST OF FIGURES

Figure 1.1	Piceance basin location (courtesy: TICORA, 2002).....	3
Figure 1.2	Location of major fields producing gas from reservoirs in Mesaverde Total Petroleum System, Piceance Basins, Colorado. Rulison field is marked red. (modified from USGS Digital Data Series 69-B).....	10
Figure 1.3	Depositional and stratigraphic framework of the Piceance basin (internet source: <a href="http://www.searchanddiscovery.com/documents/abstracts/2005hedberg_vail/abstracts/extended/yurewicz/images/fig01.htm">http://www.searchanddiscovery.com/documents/abstracts/2005hedberg_vail/abstracts/extended/yurewicz/images/fig01.htm</a> ).....	11
Figure 1.4	Schematic cross section illustrating gas migration model for the Mesaverde in the Piceance Basin (courtesy: Scheevel and Cumella 2005).....	13
Figure 1.5	Petroleum system events chart showing interpreted timing of elements and processes related to hydrocarbon generation and accumulation in Piceance basin. Water block refers to hydrocarbon trapping by capillary seal. Peak generation refers to maximum depth of burial. Events chart format modified from Magoon and Dow (1994).....	13
Figure 1.6	Tectonic history of Piceance basin, Rulison field area (courtesy: Kuuskraa et al. 1997).....	14
Figure 1.7	Development of the major Fractures in the Rulison field, Piceance basin (courtesy: Kuuskraa. et al. 1997).....	14
Figure 1.8	Rulison Field annual production volumes for Wasatch Formation and Mesaverde Group reservoirs and annual well counts for the same reservoirs from 1969 to the end of 1998. (From Hemborg, 2000).....	16
Figure 1.9	Rulison field annual production volumes and annual well counts from 2000 to the end of 2005 (the data used are from COGIS).....	16



Figure 1.10	Location of RCP's 4D 9C survey area and some wells involved in the research (courtesy: Williams).....	18
Figure 1.11	Time section of compressional wave data. Presented is inline 18. The main reservoir interval of interest in this study is between the UMV and Cameo .....	23
Figure 1.12	Time section of fast shear wave data. Presented is inline 18. Notice the difference in reflectivity in the main reservoir interval between the P- and S- wave data.....	24
Figure 1.13	Time section of fast converted wave data. Presented is inline 18. Four horizons are demonstrated, reflecting four main events involved in the well tie.....	24
Figure 1.14	Time structure of the top of the reservoir, UMV-shale horizon. The horizon was picked on: a) compressional wave data; b) converted wave data; c) shear wave data.....	25
Figure 1.15	Time structure of the bottom of the reservoir, CAMEO-coal horizon. The horizon was picked on: a) compressional wave data; b) converted wave data; c) shear wave data.....	26
Figure 1.16	Isochron between the top and the bottom of the reservoir. The difference was estimated on: a) compressional wave data; b) converted wave data; c) shear wave data.....	27
Figure 1.17	Signal RMS amplitude maps estimated from PP wave data within the window size of 10 ms. The data displayed: a) UMV horizon; b) Cameo horizon; c) Middle of the reservoir at 1000 ms in PP time.....	28
Figure 1.18	P-wave fold for all offset, RCP 2003 survey (Jansen, 2005).....	29
Figure 1.19	Usable S-wave fold with 4,000 ft maximum offset, RCP 2003 survey (Jansen 2005).....	29

Figure 2.1 General workflow chart for interval  $V_p/V_s$  estimation..... 31

Figure 2.2 Well tie to the PP seismic data. a) The portion of the time section is correlated with the P-wave well log by matching the events on composite trace (red curve) and synthetic trace (blue curve); b) The extracted wavelet with a constant phase in the time domain; c) Frequency domain of the wavelet; d) Cross correlation plot demonstrating a zero-phase symmetric waveform at zero time with correlation coefficient of about 0.70..... 34

Figure 2.3 Well tie to the SS seismic data. a) The portion of the time section is correlated with the S-wave well log by matching the events on composite trace (red curve) and synthetic trace (blue curve); b) The extracted wavelet with a constant phase in the time domain; c) Frequency domain of the wavelet; d) Cross correlation plot demonstrating a zero-phase symmetric waveform at zero time with correlation coefficient of about 0.73..... 36

Figure 2.4 Well tie to the PS seismic data. a) The portion of the time section is correlated with the S-wave well log by matching the events on composite trace (red curve) and synthetic trace of stacked offset range (blue curve); b) The extracted wavelet with a constant phase in the time domain; c) Frequency domain of the wavelet; d) Cross correlation plot demonstrating a zero-phase symmetric waveform at zero time with correlation coefficient of 0.75..... 37

Figure 2.5 Seismic time sections in PP time domain : a) Compressional wave data; b) Shear wave data; c) Converted wave data. With the right  $V_p/V_s$  all the picked horizons must be lined up..... 40

Figure 3.1 Frequency domain of compressional wave data in PP time:  
a) original unfiltered; b) after the high frequency was cut..... 42

Figure 3.2 Frequency domain of multicomponent seismic data:  
a) converted wave data in PS time; b) filtered compressional wave data in PS time;

c) shear wave data in SS time; d) filtered compressional wave data in SS time.....	42
Figure 3.3    Workflow chart for impedance derived Vp/Vs estimation.....	44
Figure 3.4    Regional stress map ( <a href="http://www.world-stress-map.org">www.world-stress-map.org</a> ). Rulison result of N45W rotation agrees with the stress map obtained from borehole breakouts.....	46
Figure 3.5    Model based inversion flowchart (modified from Russell 1988).....	47
Figure 3.6    P-wave acoustic impedance model within the interval from Mesaverde to Cameo-coal. The black curve is P-impedance estimated from velocity and density logs and filtered to the seismic frequency bandwidth.....	49
Figure 3.7    S-wave impedance model within the interval from Mesaverde to Cameo-coal. The black curve is S-impedance estimated from velocity and density logs and filtered to the seismic frequency bandwidth.....	49
Figure 3.8    Inversion QC analysis of: a) P-wave data in PP time b) S-wave data in SS time. The inverted interval is between MSVRD and CAMEO marks. Blue curve represents impedance estimated from well log. Black curve is the earth model created by extrapolating the well logs. Red curve is the result of inversion. The match between real and estimated acoustic impedance is 0.8 for P-wave data and 0.7 for S-wave data. Arrows indicate the zones of distinguished errors in the inversion results.....	51
Figure 3.9    P-wave impedance result after applying model based inversion algorithm to the seismic data. Inserted curve is high frequency cut P-impedance calculated from the well logs.....	52
Figure 3.10   S-wave impedance result after applying model based inversion algorithm to the seismic data. Inserted curve is high frequency cut S-impedance calculated from the well logs.....	52
Figure 3.11   Calculated pseudo density log. The blue curve representing pseudo density has lower values than those of the red curve, tool registered	

and normalized bulk density. The pseudo impedance results, as a product of pseudo density and S-wave velocity have lower values than normal impedance as well.....	55
Figure 3.12 The crossplot and histogram of pseudo and normal density logs.....	56
Figure 3.13 Pseudo $\hat{S}$ -impedance model estimated from pseudo density $\hat{\rho}$ and S-wave velocity log data.....	57
Figure 3.14 Inversion analysis of PS data, where pseudo S-impedance is modeled through the pseudo density estimation. Correlation coefficient, estimated within Mesaverde – Cameo interval is about 0.73.....	58
Figure 3.15 Comparison of S-impedance (left) generated from SS amplitudes and pseudo S-impedance (right) generated from PS amplitudes. The amplitudes are lower on the right image, which could be expected from lower pseudo density values.....	59
Figure 3.16 Comparison of attributive S-impedance (left) and corrected pseudo S-impedance (right) after differential modeling corrections are applied.....	60
Figure 3.17 The crossplot of impedance values after the differential modeling corrections have been applied. The X axis is represented by S-impedance amplitudes from PS-wave data, the Y axis is represented by S-impedance amplitudes from SS-wave data. The slope of the regression line is $Y=1.42X-9328$ .....	61
Figure 3.18 The histograms of S-impedance amplitudes. a) S-impedance generated from SS-wave data. The mean value is 20724 and deviation number is 1796. b) S-impedance generated from PS-wave data. The mean value 209405 and deviation number 1673 are very close to the ones above. c) Both SS-wave (blue curve) and PS-wave (red curve) generated impedance data.....	62
Figure 3.19 QC of the corrected pseudo impedance volume. Left screen shows	

the correlation between original shear impedance log (blue curve) and synthetically generated impedance volume (red curve). The right screen displays the noticeable improvement in correlation that is obtained after the applied corrections.....	63
Figure 4.1 Seismic wiggle traces color coded with: a) Spatially interpolated log Vp/Vs data; b) high resolution Vp/Vs estimated from PP and S11 wave seismic data.....	67
Figure 4.2 Vp/Vs inline 18. Sections are estimated from: a) PP-S11 data set, b) PP-PS1 data set. The shown interval is in between top of Mesaverde and top of Cameo.....	70
Figure 4.3 Comparison of Vp/Vs traces (black curves) and Vp/Vs log (red curve). The data shown are obtained from: a) PP-S11 data set in PP time; b) PP-PS1 data set in PS time.....	71
Figure 4.4 Correlation of Vp/Vs estimated from PP-S11 data set (red curve) at well RWF 332-21 location and log derived Vp/Vs. Estimated correlation coefficient for UMV-Cameo interval is about 0.5, for the middle reservoir 0.77.....	72
Figure 4.5 Correlation of Vp/Vs estimated from PP-PS1 data set (red curve) at well RWF 33-21 location and log derived Vp/Vs. Estimated correlation coefficient for UMV-Cameo interval is about 0.69, for the middle reservoir 0.67.....	73
Figure 4.6 Comparison of Vp/Vs traces from PP-PS1 data set and Vp/Vs log from dipole sonic run in well RWF 441-20.....	75
Figure 4.7 Correlation of Vp/Vs estimated from PP-PS1 data set (red curve) at well RWF 441-20 location and log derived Vp/Vs. Estimated correlation coefficient for UMV-Cameo interval is about 0.39, for the middle reservoir 0.62.....	77
Figure 4.8 P-wave data transferred to SS time domain. The image on the	

left represents time section obtained after interval Vp/Vs application. The right image demonstrates the application of impedance derived Vp/Vs for rescaling of the original vertical axis. Erroneous disposition of the traces is obtained on the right image.....	78
Figure 5.1 Interval Vp/Vs covering the zone between UMV-shale and Cameo-coal (reservoir interval). Left map represents the results from compressional and shear wave data. The map on the right is from compressional and converted wave data.....	80
Figure 5.2 The percent difference map between Vp/Vs data slices generated from PP-SS and PP-PS data combination, and histogram of the data shown on color bar. The high fold area is outlined by the dashed ellipse.....	80
Figure 5.3 Interval Vp/Vs slices within the reservoir interval obtained from: a) PP-S11 data sets; b) PP-PS1 data sets. Overlaid bubbles represent estimated b) ultimate recovery provided by William Production. The color of the bubbles displays certain amount of gas in BCF. The high fold area is outlined by the dashed ellipse.....	82
Figure 5.4 Net sand thickness map from Williams Production (a) versus Vp/Vs map generated from PP-S11 (b). The slices were generated within the reservoir UMV – Cameo interval. The areas of thick net sand sections are correlated with the areas of low Vp/Vs.....	83
Figure 5.5 Seismic horizons dipping slightly in the Eastern direction. The corresponding events from top are: top of Mesaverde, top of UMV gas and top of Cameo coal.....	85
Figure 5.6 Seismic horizons colored with Vp/Vs values. The inserted vertical section from the estimated Vp/Vs volume assists in distribution analysis of velocity ratio.....	86
Figure 5.7 Impedance derived Vp/Vs volume estimated within Mesaverde – Cameo interval. The yellow-reddish colors represent low Vp/Vs.....	87
Figure 5.8 Impedance derived Vp/Vs volume estimated within Mesaverde – Cameo	

interval. The low values below 1.6 are highlighted representing potential gas charged sandstone zones.....	88
Figure 5.9 Impedance derived Vp/Vs volume estimated within Mesaverde – Cameo interval. The abnormally low values below 1.5 are highlighted representing potential overpressured gas charged zones.....	89
Figure 5.10 Histogram of Vp/Vs values distribution within the reservoir interval.....	90
Figure 5.11 Inline 50 comparing: a) Vp/Vs cross section; b) Percent S-impedance difference between 2003 and 2004 surveys, estimated from S11 data. The sequence of low and high Vp/Vs values constrained by a black box corresponds to the area where no time-lapse changes are observed. The areas of normal Vp/Vs correspond more to significant 4D difference.....	92
Figure 5.12 A random inline and crossline from the volume of percent impedance difference between 2003 and 2004, and low Vp/Vs time slice. The enclosing section is shown in the right. Time-lapse anomalies are not present in the areas of low Vp/Vs.....	93
Figure 5.13 A random line of seismic wiggle traces in the middle of the survey colored with: a) P-wave velocity generated from impedance inversion of compressional wave data; b) S-wave velocity generated from impedance inversion of shear wave data. Both sections are shown in PP time.....	95
Figure 5.14 Vp/Vs section transformed to depth domain with: a) P-wave velocity; b) S-wave velocity. Shown inline 18 presents a good correlation between well tops and depth converted horizons. The same events correspond to slightly different vertical scale on two images. It can be concluded that both velocity volumes are usable for depth conversion.....	97
Figure 5.15 Location of the wells included in lithological model building.....	98

- Figure 5.16 The cross-section of the model built by interpolating gamma ray log results from 73 wells. The color bar represents API values with a cutoff at 80. The black curve is the log  $V_p/V_s$  estimated from dipole sonic log. Low  $V_p/V_s$  correspond to low gamma ray zones..... 99
- Figure 5.17 The cross plots of gamma ray versus: a) P-impedance; b) S-impedance; c)  $V_p/V_s$ . The color code is the depth interval bounded by UMW and Cameo well tops. The red line on each plot represents the average numbers and displays the general trend of the scattered points..... 102
- Figure 5.18 Reservoir volume sliced in the middle and colored with  $V_p/V_s$  values. The stacked layers form the volume. Each layer can be examined individually to provide more detailed and accurate interpretation.....103
- Figure 5.19 Depth interval slices generated within the 5400-5500 ft interval:  
a)  $V_p/V_s$  computed from PP-S11; b)  $V_p/V_s$  computed from PP-PS1;  
c) interpolated gamma ray model. The dashed ellipse outlines the seismic high fold coverage..... 105
- Figure 5.20 Depth interval slices generated within the 5500-5600 ft interval:  
a)  $V_p/V_s$  computed from PP-S11; b)  $V_p/V_s$  computed from PP-PS1;  
c) interpolated gamma ray model. The dashed ellipse outlines the seismic high fold coverage..... 106
- Figure 5.21 Depth interval slices generated within the 5600-5700 ft interval:  
a)  $V_p/V_s$  computed from PP-S11; b)  $V_p/V_s$  computed from PP-PS1;  
c) interpolated gamma ray model. The dashed ellipse outlines the seismic high fold coverage..... 107
- Figure 5.22 Depth interval slices generated within the 5700-5800 ft interval:  
a)  $V_p/V_s$  computed from PP-S11; b)  $V_p/V_s$  computed from PP-PS1;  
c) interpolated gamma ray model. The dashed ellipse outlines the seismic high fold coverage..... 108
- Figure 5.23 Depth interval slices generated within the 5800-5900 ft interval:  
a)  $V_p/V_s$  computed from PP-S11; b)  $V_p/V_s$  computed from PP-PS1;  
c) interpolated gamma ray model. The dashed ellipse outlines the seismic high fold coverage..... 109



Figure 5.24	Depth interval slices generated within the 5900-6050 ft interval: a) Vp/Vs computed from PP-S11; b) Vp/Vs computed from PP-PS1; c) interpolated gamma ray model. The dashed ellipse outlines the seismic high fold coverage.....	110
Figure 5.25	Depth interval slices generated within the 6200-6300 ft interval: a) Vp/Vs computed from PP-S11; b) Vp/Vs computed from PP-PS1; c) interpolated gamma ray model. The dashed ellipse outlines the seismic high fold coverage.....	111
Figure 5.26	Depth interval slices generated within the 6300-6400 ft interval: a) Vp/Vs computed from PP-S11; b) Vp/Vs computed from PP-PS1; c) interpolated gamma ray model. The dashed ellipse outlines the seismic high fold coverage.....	112
Figure 5.27	A prospect identified around well RWF 332-21 at depth 5500 ft. The vertical sections are represented by Vp/Vs values below 1.6, where inline is PP-S11 and crossline – PP-PS1 data sets. The horizontal section is percent impedance time-lapse change. The curve displays gamma ray log registered in the well.....	115
Figure 5.28	The zoomed in segment of well RWF 332-21, showing deviation of gamma ray curve towards lower values in the area of zero impedance change.....	116
Figure 5.29	Abnormally low Vp/Vs values are very well correlated with low gamma ray from RWF 332-21 in the zone of interest.....	117
Figure 5.30	A prospect identified around well RWF441-20 at depth 6228 ft. The vertical sections are represented by Vp/Vs values below 1.6, where inline is PP-S11 and crossline – PP-PS1 data sets. The horizontal section is percent impedance time-lapse change. The curve displays gamma ray log registered in the well.....	118
Figure 5.31	The zoomed in segment of well RWF 441-20, showing deviation of gamma ray curve towards lower values in the area of zero impedance change.....	119

Figure 5.32 Abnormally low  $V_p/V_s$  values are very well correlated with low gamma ray from RWF 441-20 in the zone of interest..... 120

## LIST OF TABLES

Table 1.1	Acquisition parameters for 2003 and 2004 seismic data (acquired by Solid State).....	17
Table 1.2	P-P data processing flow (processed by Veritas Geoservices).....	19
Table 1.3	P-S data processing flow (processed by Veritas Geoservices).....	20
Table 1.4	S-S data processing flow (processed by Veritas Geoservices).....	21
Table 5.1	Relative abundance (percentage) of phyllosilicate mineralogy from XRD (Rojas 2005).....	98

## **ACKNOWLEDGEMENTS**

I acknowledge all the people involved and dedicated to the RCP project at Colorado School of Mines, its sponsors for their financial support, guidance and the experience they are ready to share with students in order to make them understand the existing problems with a research and build the knowledge needed for successful results. I recognize the contribution of Williams Oil Company. Provided data, maps and figures along with the suggestions became an essential part of this research.

I would like to express my sincere appreciation to Dr. Thomas L. Davis for being not only research but also a life advisor and for his understanding and support during these years of study. I would specially like to thank Reinaldo Michelena (iReservoir.com) for his essential help and mentoring, which made this research a success. Further I extend my thanks to my research committee members, Professors Ilya Tsvankin and Yaoguo Li. Their contribution and practical advice sharpened my knowledge about the topic of investigation. I greatly appreciate the experienced revisions of my work provided by Dr. Steve Hill and Dr. Terry Young.

Finally, I would like to thank all the faculty and staff of Geophysics department for their tenderness and willingness to help in any situation. My great gratitude is going to the friends I met at school, Jyoti Behura, Xiaoxia Xu, Matthew Silbernagel, Gerardo Franco and many others without whom I would not have been able to see all the fun in this academic process.

## **CHAPTER 1**

### **INTRODUCTION**

The research is conducted within the Reservoir Characterization Project (RCP) at Colorado School of Mines. The aim of the project is to develop and apply multi-component, time-lapse seismology techniques and to integrate them with other geological, geophysical and petroleum engineering disciplines for improved reservoir recovery.

Phases X and XI of the project include study of the tight gas sandstone and coalbed reservoir of Rulison field, which is a part of the Piceance basin located in Western Colorado (Figure 1.1). The unconventional gas bearing reservoir requires a special approach to help unlock gas in place in the Piceance basin (Johnson et.al. 1987). Characterization of the reservoir by means of seismically derived Vp/Vs is potentially one of these approaches and the purpose of this thesis is to test its application.

#### **1.1 Characterization And Production Challenges**

Unconventional gas is a great potential hydrocarbon resource. Along with discovered and developed conventional reservoirs, more attention is now being drawn to unconventional gas from tight sandstone reservoirs. The discovery and production of sandstone bodies containing producible gas is the main goal for operating companies in the Rocky Mountain Region. The gas-rich play at Rulison field, located in the western part of Colorado, involves discontinuous sandstones. These bodies would require a significant number of wells to be drilled, which is not economically and environmentally beneficial. Sweet spots or areas of higher reservoir quality need to be identified to optimally position wells. The characterization of a tight gas sandstone reservoir is a

challenge and all available techniques, methods and data resources in conjunction with a multidisciplinary approach are needed to understand and assess the full potential of the gas accumulation at Rulison field.

The study area exhibits very complex geology, creating a highly heterogeneous reservoir environment. The reservoir consists of a mixture of sandstone, shale and shaly sandstones. Unlike conventional reservoirs, the tight gas sandstones (defined because of low porosity and permeability), bear no free water. The water is concentrated above the reservoir and an unusual aspect of the reservoir is a continuous gas column with no free water over an interval of up to 2000 feet.

Traditionally, this type of the reservoir is developed and produced by hydraulic fracturing the production interval. The gas flow is naturally maintained by pressure. To increase the gas flow from in-situ depositions to the producing well and consequently to the surface, specifically mixed fluid is pumped into the reservoir interval at high pressure. This causes fractures to open and increase the permeability of the rocks.

The production from unconventional gas reservoirs, such as Rulison field becomes very costly and challenging. Because of the reservoir heterogeneity, the approach chosen in the industry is to complete multiwells with dense spacing hoping that gas bearing sandbodies can be penetrated and produced. An often encountered problem is establishing the sandbodies' connectivity from well to well even at 10 acre (660 ft) spacing. Another problem is determining what intervals are flowing and which are not as these wells are depleted over the production interval.

Unconventional tight gas exploration and exploitation generally ignores seismic application as a characterization tool for this type of reservoirs. The reason is low reflectivity of conventionally acquired compressional wave data, especially in the gas saturated section. Acquisition of 9-C seismic surveys and dipole sonic logs by RCP within the area of study are changing the landscape of seismic applications to tight gas.

Multicomponent seismic brings the opportunity to analyze P-wave and S-wave type velocity. In combination, these parameters provide better characterization tool, than

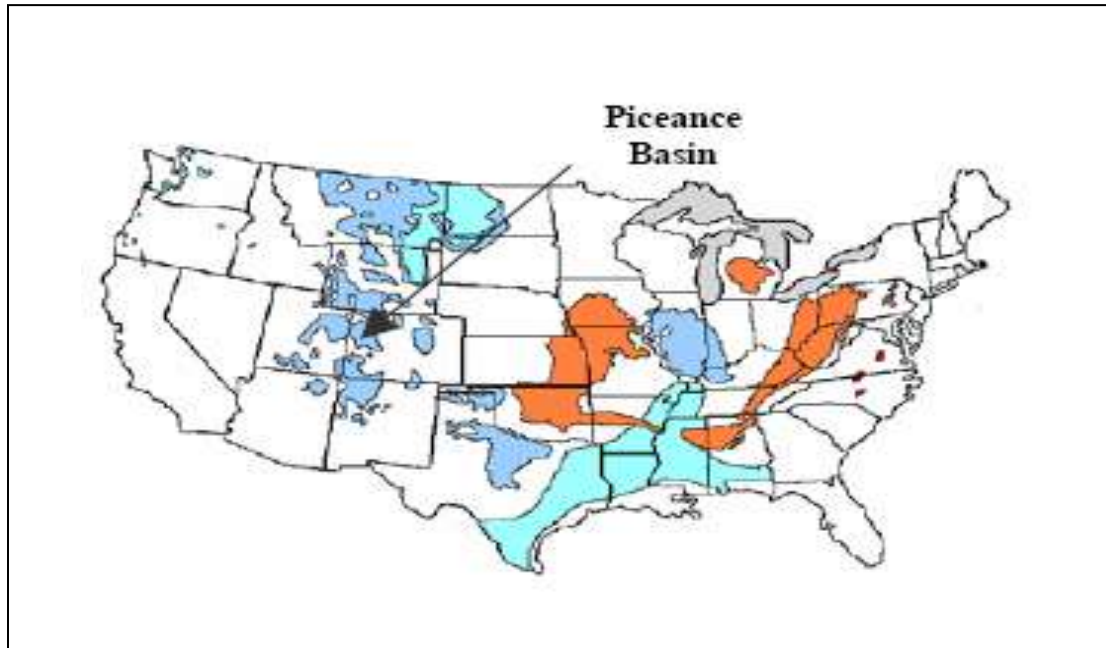


Figure 1.1 Piceance basin location (courtesy: TICORA, 2002).

each single of them. The studies conducted by researchers at different time emphasize the fact that velocity ratio of compressional and shear wave velocity –  $V_p/V_s$  can be used for rock quality determination.

## **1.2 Previous Studies Of The $V_p/V_s$ Application**

Many studies were conducted to understand the relationship between  $V_p/V_s$  and reservoir parameters. This subchapter summarizes the analytical framework of these studies.

Multicomponent seismic data are necessary for improved reservoir characterization and monitoring. Tatham and McCormack (1991) indicted that virtually any change in the structure or composition of a solid will induce change in the propagation characteristics of elastic waves. Considerable work has been done in

laboratories to understand the dependence of elastic properties on lithology. Anderson and Liberman (1996) measured elastic moduli and velocities in typical rock-forming minerals. Pickett (1963) determined unique  $V_p/V_s$  values for clean, well-consolidated sandstones, dolomites and limestones and constructed the diagram where each lithology type concentrates within its own  $V_p/V_s$  line. Later, a group of researchers including Nations (1974), Kithas (1976), Benzing (1978), extended the Pickett diagram with the results from well logs. Typical sedimentary rocks were studied by Domenico (1984). His measurements revealed ranges of  $V_p/V_s$  for such rocks, as water-saturated sandstone, calcareous sandstone, limestone and dolomite.  $V_p/V_s$  values of unconsolidated marine shales, about 2.6, estimated by Hamilton (1979) were recently updated with consolidated shale  $V_p/V_s$ , extracted from seismic data. Various values for different samples of shales are reported by a number of researchers. For example, the Grayson shale has an estimated  $V_p/V_s$  of 2.43 and above (Geyer and Martner, 1969), the Pierre shale ranges from 2.7 for low (McDonal et al. 1958) and 2.93 for high (Krishnamurthi and Balakrishna 1953). Tatham and McCormack (1991) explain that shale cores suffer irreversible changes in being transferred from the borehole to the laboratory that cannot be corrected by restoring the sample to the original in-situ conditions. So, the core measurements have such disadvantages as uncertainties in the precise composition, volume and condition of the sample being measured.

P-waves and S-waves are very sensitive to porosity variations. Some early empirical relationships between velocity and porosity for very soft, unconsolidated, marine sediments were derived by Wood (1949) and verified by Hamilton (1972). Equations proposed by Pickett (1963) were analyzed by Domenico (1984). The samples of clastic silicate rocks, studied by Castagna et al. (1985), provided an empirical relationship, which also includes clay content.

Pore fluid content versus  $V_p$  and  $V_s$ , and  $V_p/V_s$  was widely covered in the literature. Domenico (1976) concluded that P-wave and S-wave velocities are relatively insensitive to mixtures of gas and liquid pore fluids up to liquid saturation level of about



90 percent. At this point, his graph demonstrated a rapid increase of compressional wave velocity, while shear wave velocity stayed almost unchanged.

Variations in pore shape affect  $V_p$  and  $V_s$ . This theory was described by Toksöz et al. (1976). One can apply the model, built by Toksöz, for  $V_p/V_s$  prediction in rocks with various aspect ratios of pores (Tatham and McCormack 1991).

Pore shape can play a significant role in anisotropy. Anisotropic environment has a significant effect on the wave propagation. For instance, entering anisotropic medium, a S-wave splits into fast and slow propagating shear waves. P-wave velocity also differs with the direction, along or across the fractures. To compute velocities of those elastic waves, a method was developed by Crampin (1978). An experiment was conducted on a solid sample with small concentration of parallel cracks. The elastic anisotropy for Chelmsford granite, Chicopee shale, and Berea sandstone was laboratory measured (Lo et al., 1986). P-wave and S-wave anisotropy exhibited different behavior while differential pressure was changed in each of these rocks.

Tatham and McCormack (1991) showed differential pressure, depth of burial, and consolidation as a function of velocity ratio. These relationships were established based on core samples of limestone and sandstone. The results confirmed fundamental morphological differences in carbonate and clastic pores.

Increasing temperature with depth changes  $V_p$  and  $V_s$ . This topic was covered by Timur (1977), who concluded that for a large set of sedimentary rocks, average decrease for P-wave velocity was 1.7 and for S-wave – 0.9 percent for a 100° C rise in temperature. For oil-saturated sandstones, however, velocity decrease of about 35 % was recorded for both types of waves as temperature increased for a 100° C (Tosaya et al. 1984).

The recent research by Rojas (2005) conducted at Rulison field confirmed the importance of the velocity ratio -  $V_p/V_s$  parameter for the reservoir characterization. Her work is directly related to the current research in that it quantifies  $V_p/V_s$  variations due to changes in pressure, lithology and pore fluid in tight gas sandstones. Tight sandstones

will typically have a  $V_p/V_s$  lower than 1.7, while shales will have  $V_p/V_s$  higher than 1.7. Typically, the presence of gas-saturated sandstones lowers the  $V_p/V_s$  to 1.6 and below. The overpressured zones can affect velocity ratio and decrease  $V_p/V_s$  values to as low as 1.4. Thus,  $V_p/V_s$  is an important geophysical parameter for tight gas reservoir characterization at Rulison field. Promising results from Rojas (2005) laboratory measurements motivated the presented work.

### **1.3 Research Objectives**

This research is focused on developing a methodology for  $V_p/V_s$  velocity ratio estimation from multicomponent seismic traveltimes and amplitudes and its application to reservoir characterization and prospect delineation in the tight gas reservoir at Rulison field. I develop a technique to output a small sampled  $V_p/V_s$  volume over the reservoir interval at Rulison field. The volume helps to foster and develop cooperation between geologists, geophysicists, petrophysicists and engineers.

The main study objectives include:

- a) Use multicomponent seismic data for developing a workflow for  $V_p/V_s$  estimation with an improved vertical resolution in contrast to traveltime estimations. I involve a detailed analysis and testing of the results from each of the applied methods and steps. Thus, this work may serve as guidance for the future application of the workflow in a tight gas sandstone environment.
- b) Analyze the difference of output  $V_p/V_s$  while applying PP-S11 and PP-PS1 combinations. This procedure enhances the interpretability and reliability of the results.
- c) Convert the  $V_p/V_s$  values to reservoir parameters through the tie with rock physics laboratory measurements of the cores. Lithology, fluid content and pressure conditions influence the propagation characteristics of compressional and shear waves. The  $V_p/V_s$  velocity ratio is an input component for 3D reservoir modeling and characterization.

I show that estimated Vp/Vs volumes are tied back to the well log data. This fact provides us with confidence in the results and confirms the applicability of the used methodology in the area of investigation.

#### **1.4 Thesis Outline**

The thesis research is explained in six chapters. The first chapter provides an introduction to the area of investigation, geological settings and background information. The methodology applied and workflow for Vp/Vs estimation from multicomponent seismic data is provided in Chapter 2. Described is the seismic interpretation as the beginning of the process. Modeling of multicomponent subsurface recordings, wavelet extraction, well tie, picking horizons on seismic data and proper time domain calibration are the main procedures for interval Vp/Vs calculation. The applied model-based inversion for impedance is explained in chapter 3 and the results of P- and S-impedance are demonstrated. The methodology for Vp/Vs derivation from seismic amplitudes is presented in chapter 4. Chapter 5 covers interpretation of the Vp/Vs results and their applicability for the tight gas reservoir characterization. Chapter 6 summarizes the conclusions deduced from the research, and indicates the possibilities for future work in this area.

#### **1.5 Geological Setting Of The Piceance Basin**

The Piceance basin occupies about 4,000 mi<sup>2</sup> and is bounded on the west by the Douglas Creek arch, on the north by the Axial fold belt, on the east by the White River uplift and on the southwest by the Uncompahgre uplift (Figure 1.2). Figure 1.2 illustrates the location of the main gas fields within the basin. Most gas production in the Piceance basin is from discontinuous fluvial sands of the Williams Fork Formation of the upper Cretaceous Mesaverde Group (McFall et. al. 1986). The sandstones and shales were deposited in a series of regressive marine and nonmarine environments (McFall et. al. 1986, Johnson 1989). Figure 1.3 is a stratigraphic section and the reservoir interval

within the Mesaverde Group. The Mesaverde Group is underlain by the marine Mancos shale and overlain by the lower Tertiary Age Fort Union and Wasatch Formations, consisting of fluvial sandstones and shales. Completions are in the Mesaverde interval, which covers about 7,225 square miles and ranges in thickness from about 2,000 feet on the west to about 6,500 feet on the east side of the basin (Johnson 1989).

### **1.5.1 Piceance Mesaverde Williams Play**

The tight gas Piceance Mesaverde Williams Fork Formation consists of low-permeability sandstones, with trapped gas in a typical continuous-type basin-center gas accumulation, containing gas downdip and water updip. This play is horizontally bounded by mapping the thermal maturity of sandstone reservoirs in the Upper Cretaceous Williams Fork, whose thickness ranges from about 1,500 ft to 4,500 ft (Johnson et al. 1987). The fluvial sandstone reservoirs vary greatly in thickness and lateral extent. Individual point bar deposits in the lower Williams Fork are typically less than 15 ft and commonly have lateral extents of 500-1000 ft. Thicker, more laterally continuous sandstones, can reach a thickness of over 100 ft and are probably the result of amalgamation (Lorenz et. al 1985, Cole and Cumella 2003). Johnson et al. (1987) mentioned that thermal maturity of the Mesaverde group is not only a major control on gas generation but also a major factor in determining reservoir quality.

Low permeability and overpressure creates a reservoir system saturated with gas rather than water (Reinecke et al. 1991). Scheevel and Cumella (2005) explain that overpressuring resulted in pervasive natural fracturing. Figure 1.4 sketches the gas migration vertically through the fracture system evolved in the lower part of the Williams Fork. The continuous gas saturated interval is overlain by a transition zone containing both gas- and water-bearing sandstones (Figure 1.4). These sandstones commonly have better porosity and permeability than those in the continuously gas-saturated interval (Scheevel and Cumella 2005).

### **1.5.2 Petroleum System Of The Piceance Basin**

The source rocks for the Williams Fork Formation are interbedded gas-prone shales, mudstones, siltstones, and coals (Johnson and Roberts 2003). Spencer (1989) claims that the gas was generated and migrated into the reservoirs in Tertiary time. Both stratigraphic and diagenetic trapping mechanisms occur in the formation. With knowledge of the source, reservoir, seal and overburden rocks, and the processes of trap formation and the generation-migration-accumulation of petroleum, one can characterize the petroleum system. A petroleum system can be defined then as a natural system that includes source rock and all related geologic elements and processes that are essential if a hydrocarbon accumulation is to exist (Magoon and Dow 1994). Figure 1.5 illustrates the petroleum system chart for the Piceance basin.

### **1.5.3 Tectonic Evolution Of The Piceance Basin**

The study of the structural and tectonic evolution of the Piceance basin indicates that basement faulting, resulting from tectonics during the Precambrian, Pennsylvanian and the Laramide and younger events have shaped the development of major fault systems. Figure 1.6 depicts the tectonic history of the area. Kuuskraa et al. (1997) indicate that a reactivated paleohorst and SW-NE directed regional shortening produced the dominant regional deformation and structures in the southeastern basin, including the Rulison Anticline. The basin has experienced WNW and EW compression from Holocene to present.

Given the structural and depositional history of the basin, the vertical overburden stress appears to be similar in magnitude to the maximum horizontal compressive stress. As a result, fracturing has occurred perpendicular to both the least and the intermediate stress orientations, creating a mix of N30°W, N60°E and N70°-80°W sub-vertical fracture

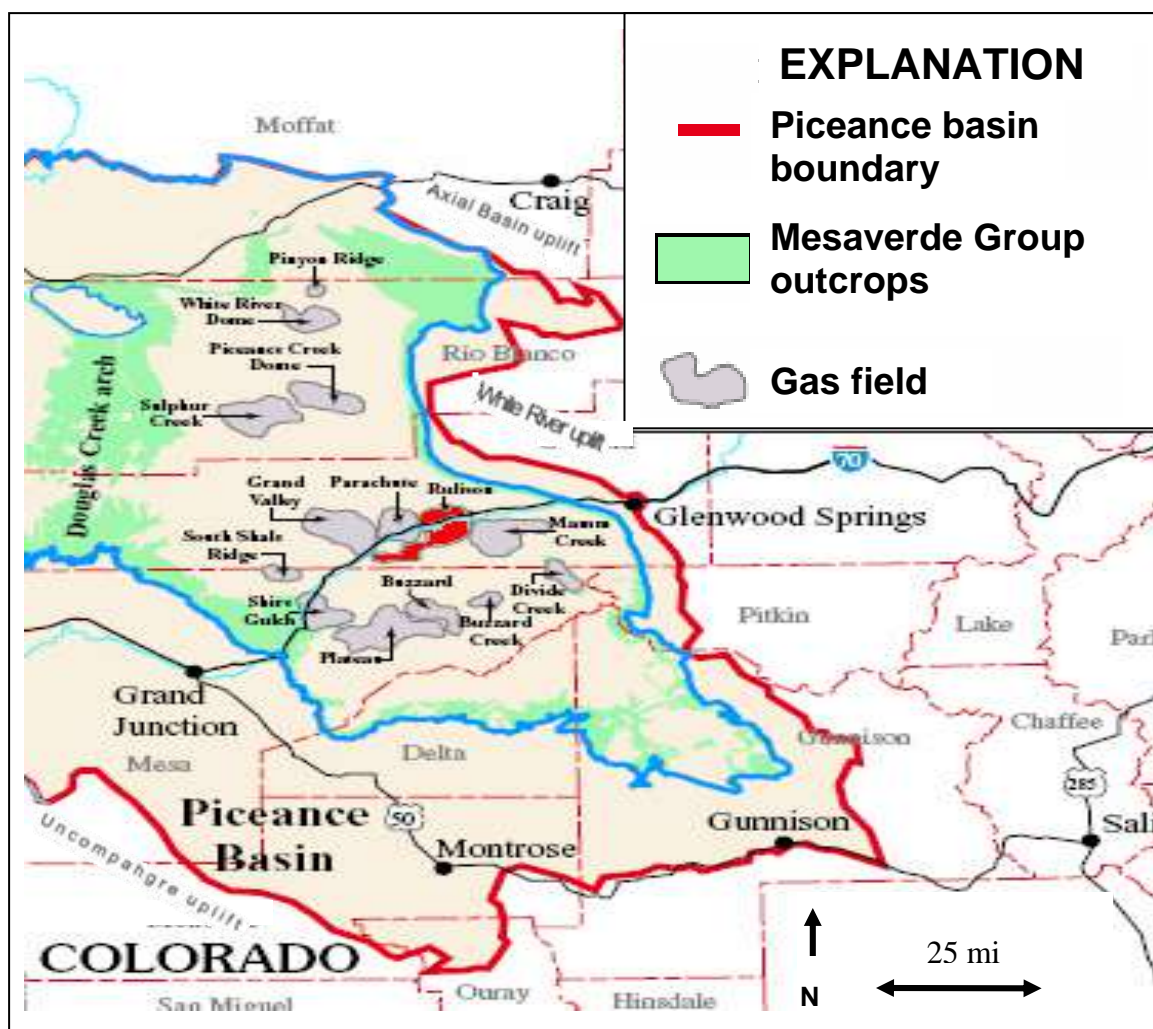


Figure 1.2 Location of major fields producing gas from reservoirs in Mesaverde, Piceance basins, Colorado. Rulison field is marked red. (modified from USGS Digital Data Series 69-B).

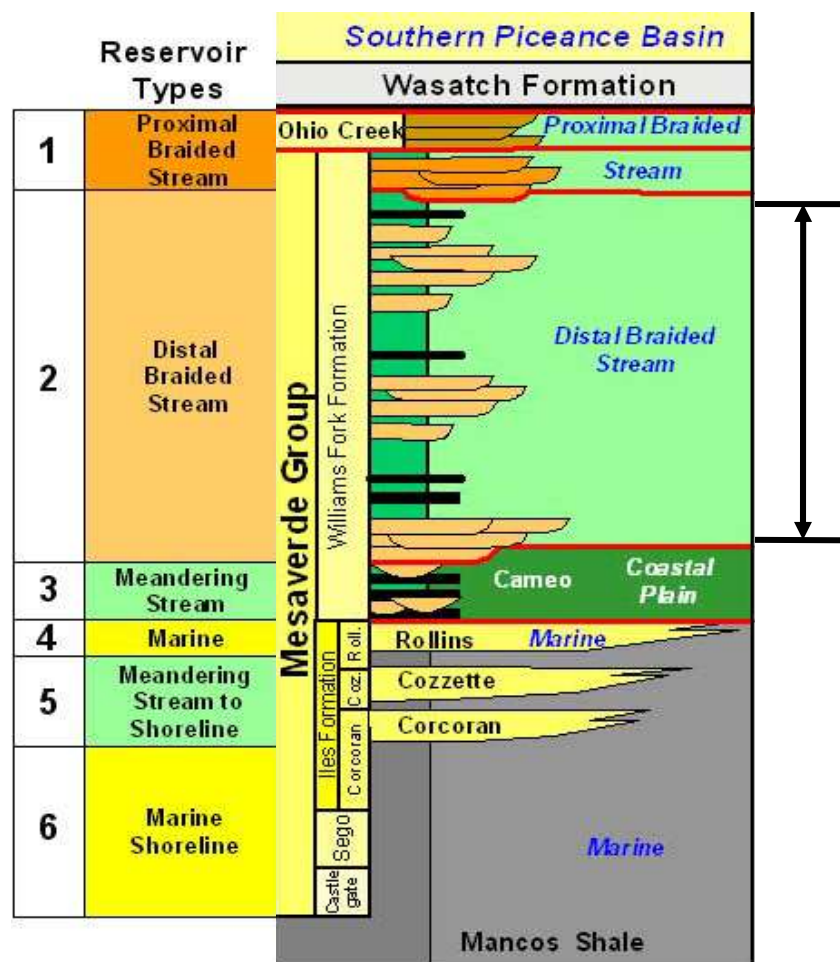


Figure 1.3 Depositional and stratigraphic framework of the Piceance basin (internet source: [http://www.searchanddiscovery.com/documents/abstracts/2005hedberg\\_vail/abstracts/extended/yurewicz/images/fig01.htm](http://www.searchanddiscovery.com/documents/abstracts/2005hedberg_vail/abstracts/extended/yurewicz/images/fig01.htm)).

trends, as shown in Figure 1.7.

## **1.6 The Study Area: Rulison Field**

Now that the complex geology of the Piceance basin is explained I will concentrate on the area of interest, Rulison field, shown in red in Figure 1.2. According to Kuuskraa et al. (1997) the Williams Fork lenticular sand formation in the Rulison field area holds a high concentration of gas in place, estimated at 160 Bcf per square mile in the sand plus another 40 Bcf per square mile in the Cameo coals. The distribution and connectivity of the fluvial tight-gas sandstones significantly impact reservoir productivity and ultimate recovery. The highly discontinuous nature of these sandstone bodies is the primary justification for 10-acre well density. This tight drilling density is necessary to intersect the relatively isolated fluvial sand bodies.

The main reservoir interval includes low permeability fluvial sandstones, shales, and coal. Heterogeneity of these fluvial deposits include large scale stratigraphic variability associated with vertical stacking patterns and structural heterogeneities associated with faults that exhibit lateral and reverse offsets. Within the various types of fluvial sandstones, internal heterogeneities caused by fractures and lateral accretionary bedding are also significant (Vargas et al. 2006).

### **1.6.1 Production History**

Piceance basin gas production began in the 1950's, sourced from the main gas fields concentrated mostly in southern portion of the basin including Rulison, Parachute, Grand Valley, Mamm Creek, and Sulphur Creek fields (U.S. Geological Survey Digital Data Series 69-B, 2005).

Rulison field experienced high growth in production during the last several years. As Hemborg (2000) indicated, average annual gas production per well during 1980 through 1989 was 32 million cubic feet (MMcft), and the averaged climbed to 84 MMcft from 1995 to 1999. This is graphically presented in Figure 1.8, annual production volumes and well counts from the Rulison field from 1970 to 1998.



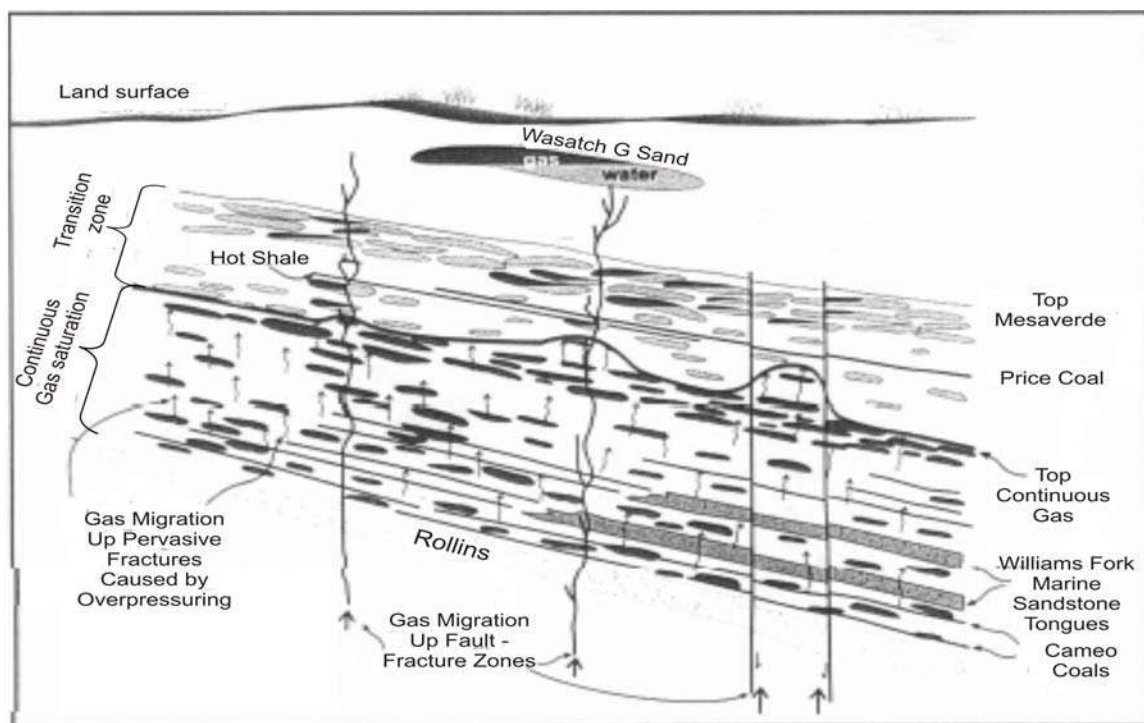


Figure 1.4 Schematic cross section illustrating gas migration model for the Mesaverde in the Piceance Basin (courtesy: Scheevel and Cumella 2005).

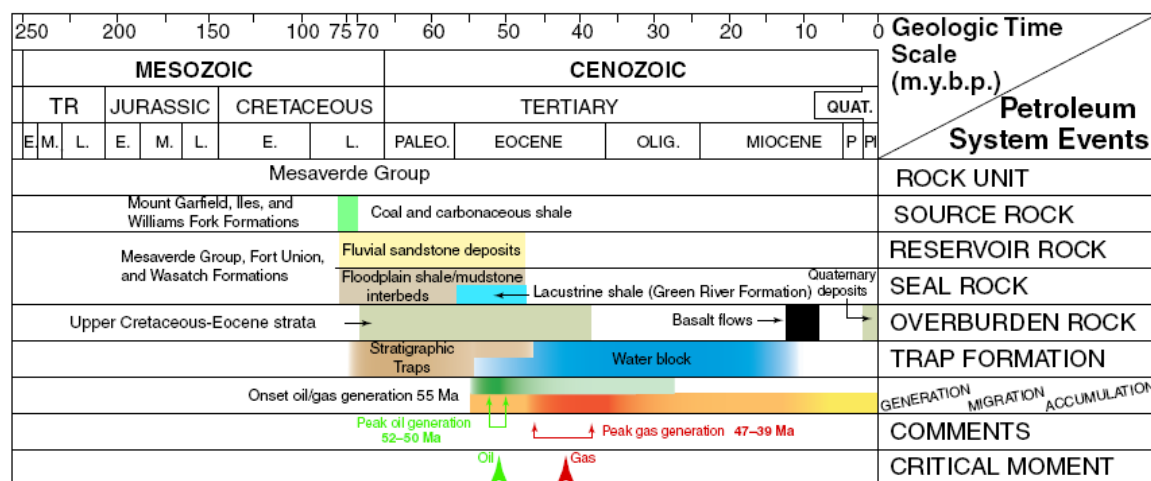


Figure 1.5 Petroleum system events chart showing interpreted timing of elements and processes related to hydrocarbon generation and accumulation in Piceance basin. Water block refers to hydrocarbon trapping by capillary seal. Peak generation refers to maximum depth of burial. Events chart format modified from Magoon and Dow (1994).


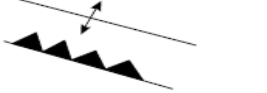


<b><i>Geologic Age</i></b>	<b><i>Structural Style</i></b>	<b><i>Schematic</i></b>
<b>Miocene to Recent</b>	<b>Regional Uplift</b>	 WNW Maximum Compression
<b>Cretaceous to Eocene</b>	<b>Laramide Thrust Faults and Related Folding</b>	 SW Directed Shortening
<b>Pennsylvanian/Permian</b>	<b>Faulting and Graben Development</b>	 NW Trending Extension
<b>Precambrian</b>	<b>Regional Crustal Shearing and Extension</b>	

Figure 1.6 Tectonic history of Piceance basin, Rulison field area (courtesy: Kuuskraa, et al. 1997).

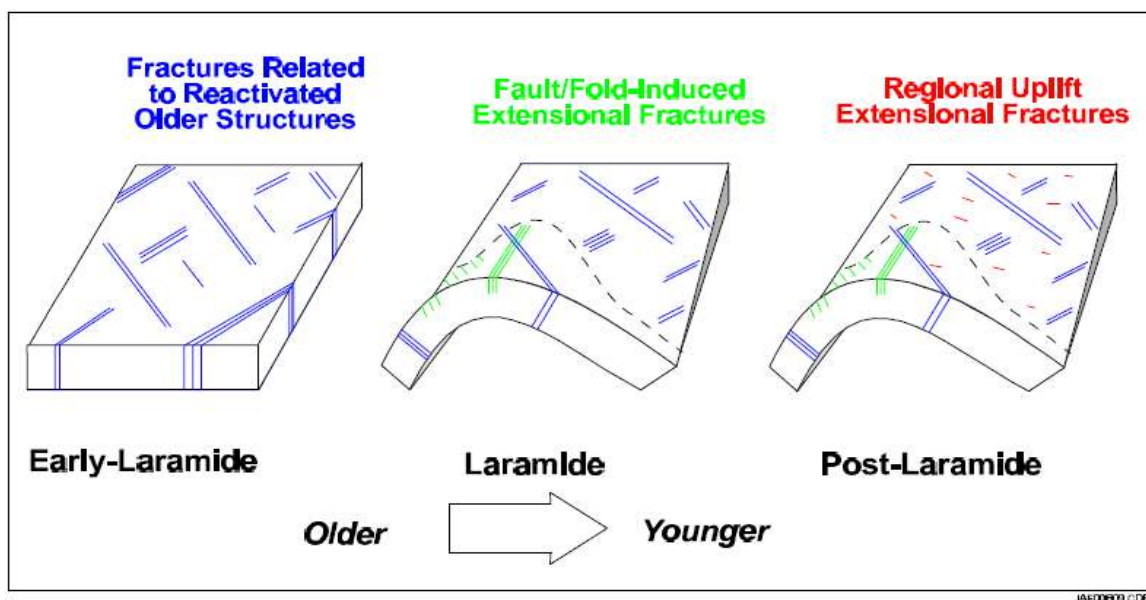


Figure 1.7 Development of the major Fractures in the Rulison field, Piceance basin (courtesy: Kuuskraa, et al. 1997).

The most recent data were obtained from COGIS (Colorado Oil and Gas Conservation Commission). Figure 1.9 indicates that production has improved significantly since 2000. At that year, the average production was 608 MMCF and by the end of 2005 it reached the point of 45290 MMCF.

### **1.7 Seismic And Well Log Data Set**

The research I concentrate on involves delineation of the lithology component of the reservoir using fully processed and stacked 3D seismic volumes including compressional, pure shear rotated for fast S11 and converted rotated for fast PS1 wave data. The RCP multicomponent seismic data I used were acquired in 2004 with the parameters summarized in Table 1.1 and the area of investigation is shown in Figure 1.10. The survey covered an area of 7260 X 8250 ft. General processing flows of P-, pure S-, and converted PS-wave data are outlined in Tables 1.2, 1.3 and 1.4. The importance of selecting the proper data processing programs, parameters, and sequences of processes to produce multicomponent seismic stacked sections for joint interpretations cannot be overemphasized (Tatham and McCormack 1991). The data were processed in a 4-D manner together with the 2003 datasets to enhance the repeatability and to extract time-lapse information. Information from wells is utilized to obtain, test and verify the results of processing. Geometrical spreading correction was applied to all volumes. Surface consistent amplitude equalization was used to preserve the amplitudes. After the trim statics, amplitude equalization was aimed to visually enhance the amplitudes. Poststack migration was followed by another amplitude equalization procedure. The last two equalizations were not to preserve the actual amplitudes.

As a result of a 10-acre infill drilling program by Williams Exploration Company, the study region within the survey has good well coverage with over 80 wells within the 2.15 mi<sup>2</sup> area. Gamma ray logs are used to simulate the distribution of sand bodies in the reservoir.

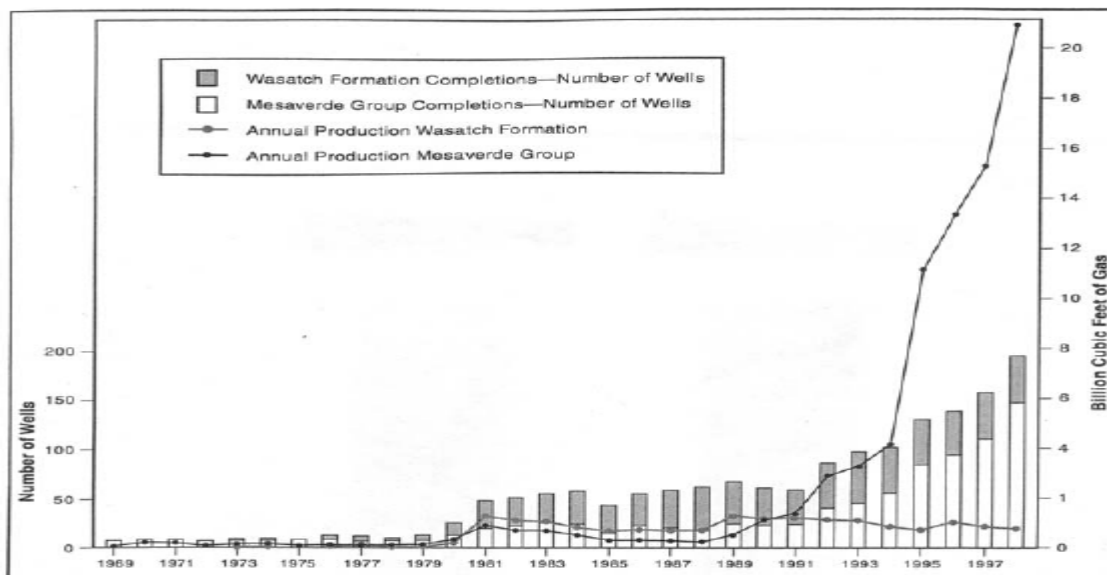


Figure 1.8 Rulison Field annual production volumes for Wasatch Formation and Mesaverde Group reservoirs and annual well counts for the same reservoirs from 1969 to the end of 1998. (From Hemborg, 2000)

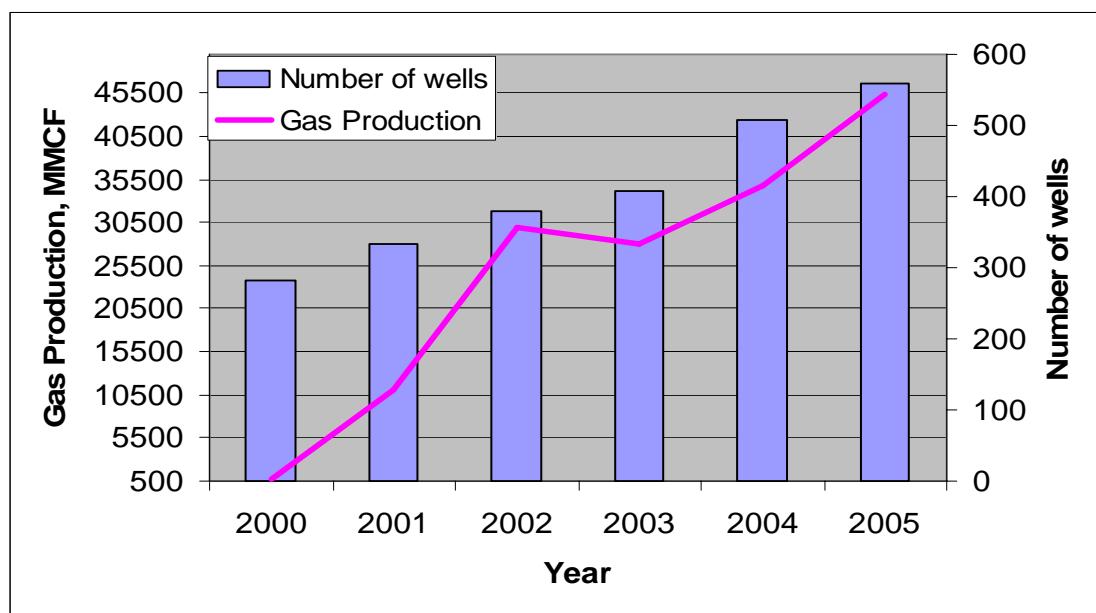


Figure 1.9 Rulison field annual production volumes and annual well counts from 2000 to the end of 2005 (the data used are from COGIS).

Sources	Receivers
Mertz 18, IVI TRI-AX, VIBPRO 3X electronics 5-120 Hz (P) and 5-50 Hz (S) 6 sweeps over 10 s 660 feet line spacing 110 feet source spacing 75 sources per line 12 lines 708 source points	I/O VectorSeis 15 s for P-source 16 s for S-source 330 feet line spacing 110 feet group spacing 66 groups per line 26 lines Static patch, all live

Table 1.1 Acquisition parameters for 2003 and 2004 seismic data (acquired by Solid State).

Velocity information is extracted from the well logs, registered within the RCP study area, and outlined in Figure 1.10. The controlling well, RWF 332-21, where a cross-dipole sonic log was run, is located in the southeast part of the survey. P- and S-wave data from this wellbore are used for the well tie involving correlation with the seismic and simple impedance model building. A blind test of the results from the study is performed on the data from a new drilled well RWF 441-20. This well contains P- and S-wave borehole velocity measurements registered by the cross-dipole sonic log tool.

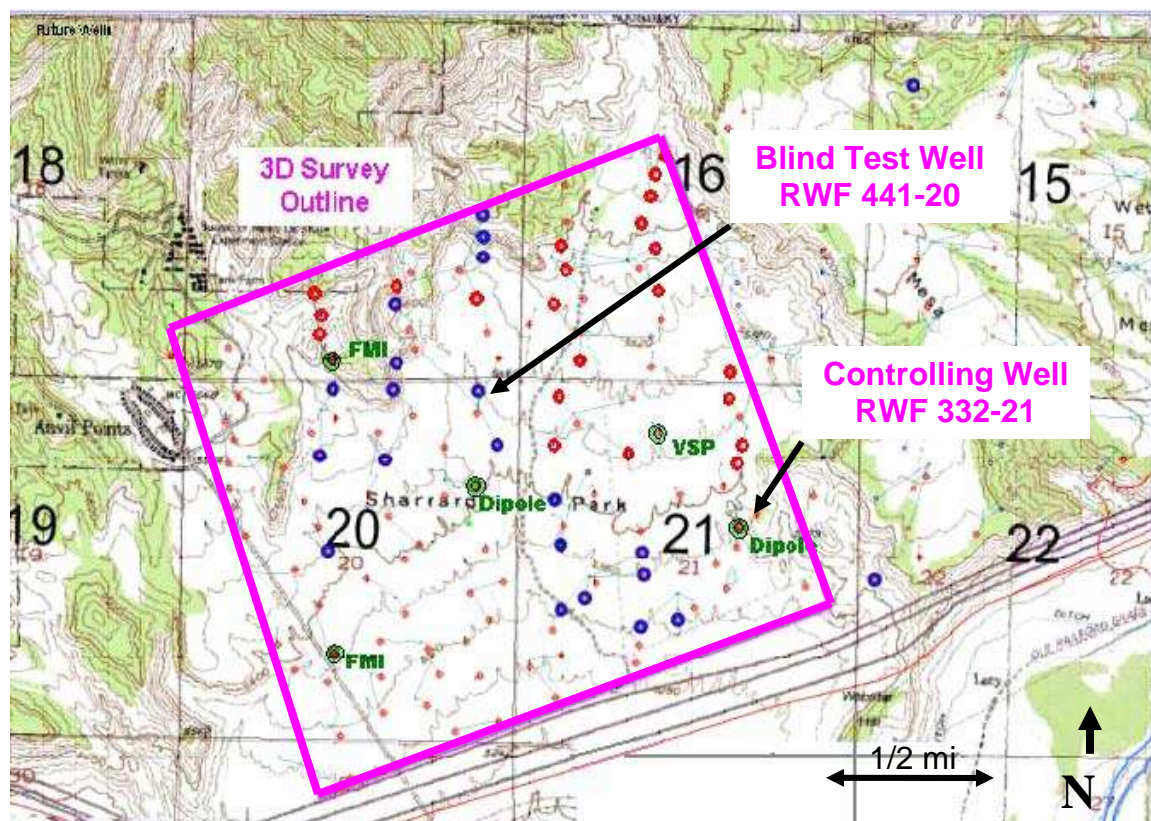


Figure 1.10 Location of RCP's 4D 9C survey area and some wells involved in the research (courtesy: Williams Oil Company).

Tilt correction for Vectorseis phone applied in Field
Demultiplex/Geometry/First Break Picks
Refraction Tomography Statics
Manual Trace Edits/Amplitude Recovery – T2
Surface Consistent Amplitude Equalization and Deconvolution
Velocity Analysis (Preliminary)
Surface Consistent Statics (Preliminary)
Velocity Analysis (Final)
Surface Consistent Statics (Final)
First Break Mutes
Trim Statics
Amplitude Equalization – Mean Scaling
Stack
Noise Attenuation (FXY Deconvolution)
Migration – Kirchhoff
Filter – 5/10-100/110 hz 0-1600 ms, 5/10-80/95 hz 1600-2800 ms
Amplitude Equalization – Mean Scaling

Table 1.2 P-P data processing flow (processed by Veritas Geoservices).

Tilt correction for Vectorseis phone applied in Field
Demultiplex/Geometry(asymptotic binning)
Manual Trace Edits/Amplitude Recovery – T2
Surface Consistent Amplitude Equalization
Rotate inline and Crossline Horizontal components using shot and receiver coordinates
Deconvolution (Surface consistent)
Velocity Analysis (Preliminary)
Horizon based station drift and long wavelength statics applied
Surface Consistent Statics (Preliminary)
Noise attenuation (Radon transform)
Velocity Analysis (Final)
Surface Consistent Statics (Final)
First Break Mutes
Trim Statics
Amplitude Equalization – Mean Scaling
Depth variant binning and stack
Migration – Kirchhoff
Filter – 4/8-50/60 hz 0-2400 ms, 4/8-35/50 hz 2400-4000 ms
Amplitude Equalization – Mean Scaling

Table 1.3 P-S data processing flow (processed by Veritas Geoservices).



Demultiplex
Geometry
Manual Trace Edits
Polarity Correction – Shot and Receiver
Amplitude Recovery – T2
Surface Consistent Amplitude Equalization
Alford Rotation – N45W
Surface Consistent Deconvolution
Source/Receiver Statics – From P-S Data
CDP Gather
Velocity Analysis (Preliminary)
Noise Attenuation – Radon Transform
Surface Consistent Statics (Preliminary)
Velocity Analysis
First Break Mutes
Trim Statics
Amplitude Equalization – Mean Scaling
Stack
Noise Attenuation (Fxy Deconvolution)
Migration – Kirchhoff
Filter – 4/8-30/40 Hz 0-3000 MS, 4/8-25/35 Hz 3000-6000 MS
Amplitude Equalization – Mean Scaling

Table 1.4 S-S data processing flow (processed by Veritas Geoservices).

### **1.8 Seismic Data Quality**

Figures 1.11 – 1.13 show migrated record sections for compressional wave, shear wave and converted wave data. Stacked data are less vulnerable to noise presence. The data are presented in their original time scale, which is the time that was spent by each wave type to pass through the same interval. The UMV-shale and Cameo-coal horizons bound the main reservoir interval. They can be easily recognized on seismic by the strong reflectors. The events are horizontally stratified in general. The time structures of both of the reservoir bounding events in Figures 1.14 and 1.15 demonstrate slightly updip structure in the south-west direction. UMV to Cameo isochron maps from multicomponent data presented in Figure 1.16 show similar trends. Seismic parameters, traveltimes and amplitude are involved in the process of  $V_p$ - $V_s$  velocity ratio estimations. RMS amplitude maps are generated from compressional wave data at the top, bottom and middle of the interval of interest (Figure 1.17). Low amplitudes appear on the edges of the survey due to low fold and inadequate aperture imaging.

Displayed in Figures 1.18 and 1.19 are pure mode fold maps for PP and SS surface registered data. As observed, the survey fold using 50'x 50' bin size is 225 at all offsets for the compressional data, and up to 65 at 4000 ft maximum offset for the shear wave data. Therefore, the actual  $V_p/V_s$  area that can be interpreted from two data set combinations, PP-S11 and PP-PS1 is concentrated towards the middle of the survey.

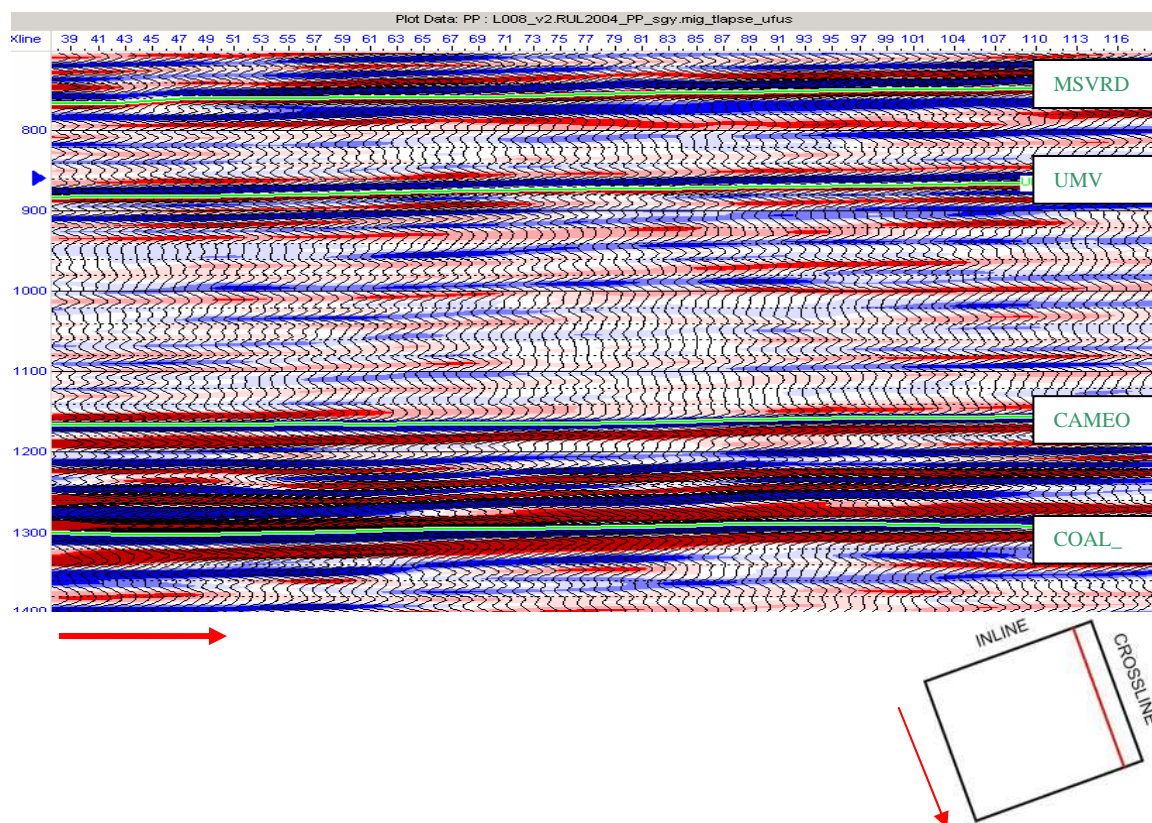


Figure 1.11 Time section of compressional wave data. Presented is inline 18. The main reservoir interval of interest in this study is between the UMV and Cameo.

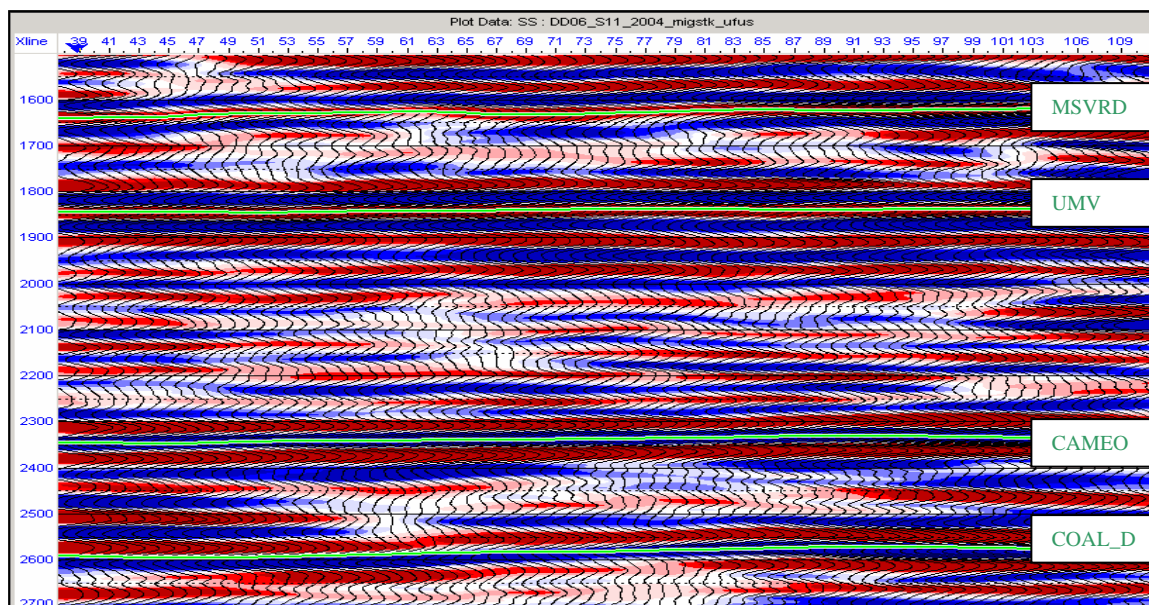


Figure 1.12 Time section of fast shear wave data. Presented is inline 18. Notice the difference in reflectivity in the main reservoir interval between the P- and S- wave data.

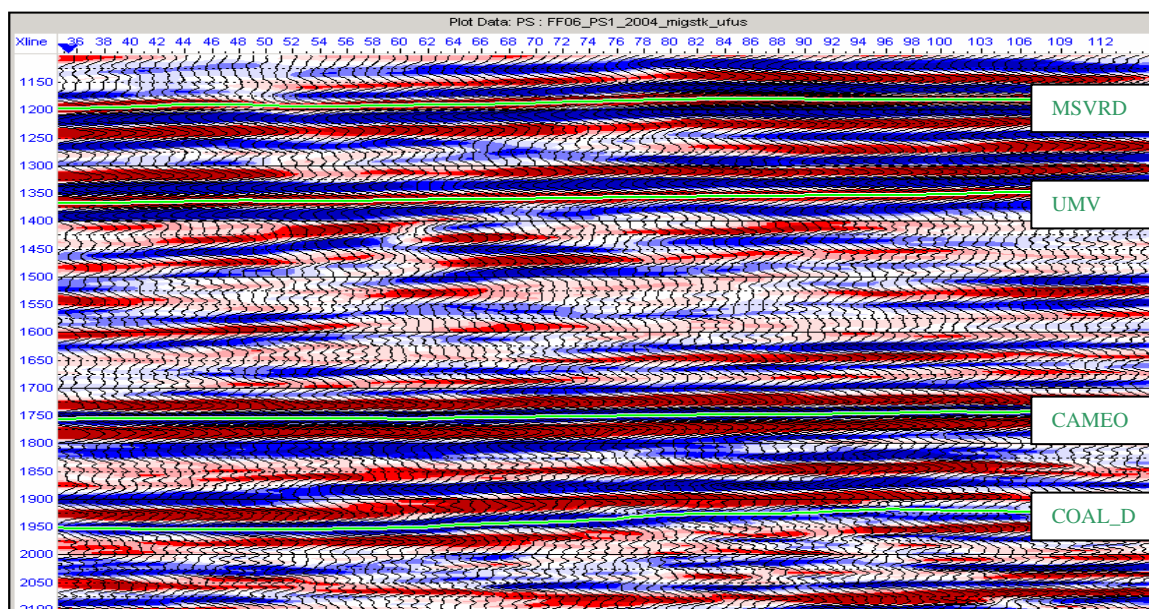


Figure 1.13 Time section of fast converted wave data. Presented is inline 18. Four horizons are demonstrated, reflecting four main events involved in the well tie.

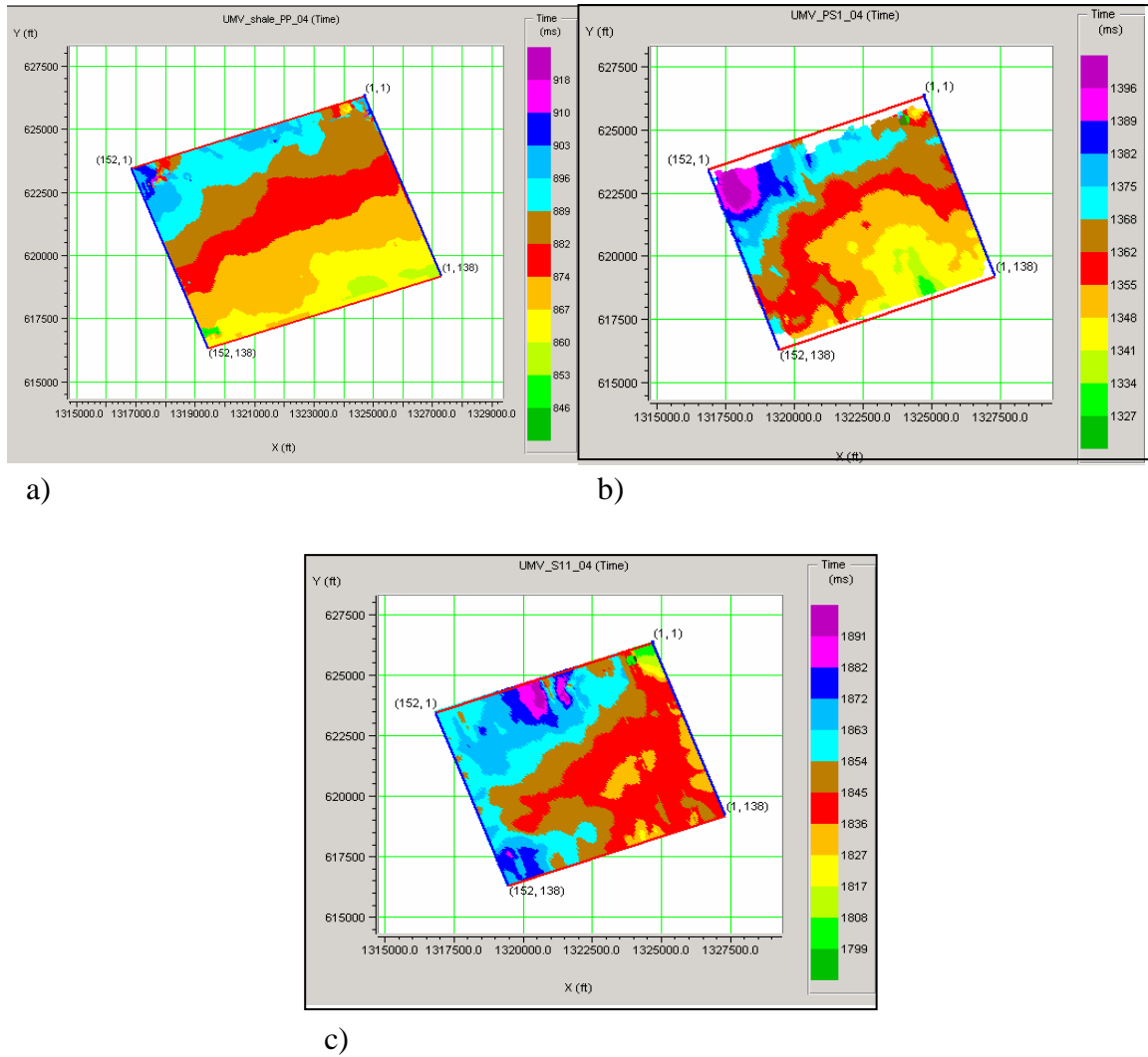


Figure 1.14 Time structure of the top of the reservoir, UMV-shale horizon. The horizon was picked on: a) compressional wave data; b) converted wave data; c) shear wave data.

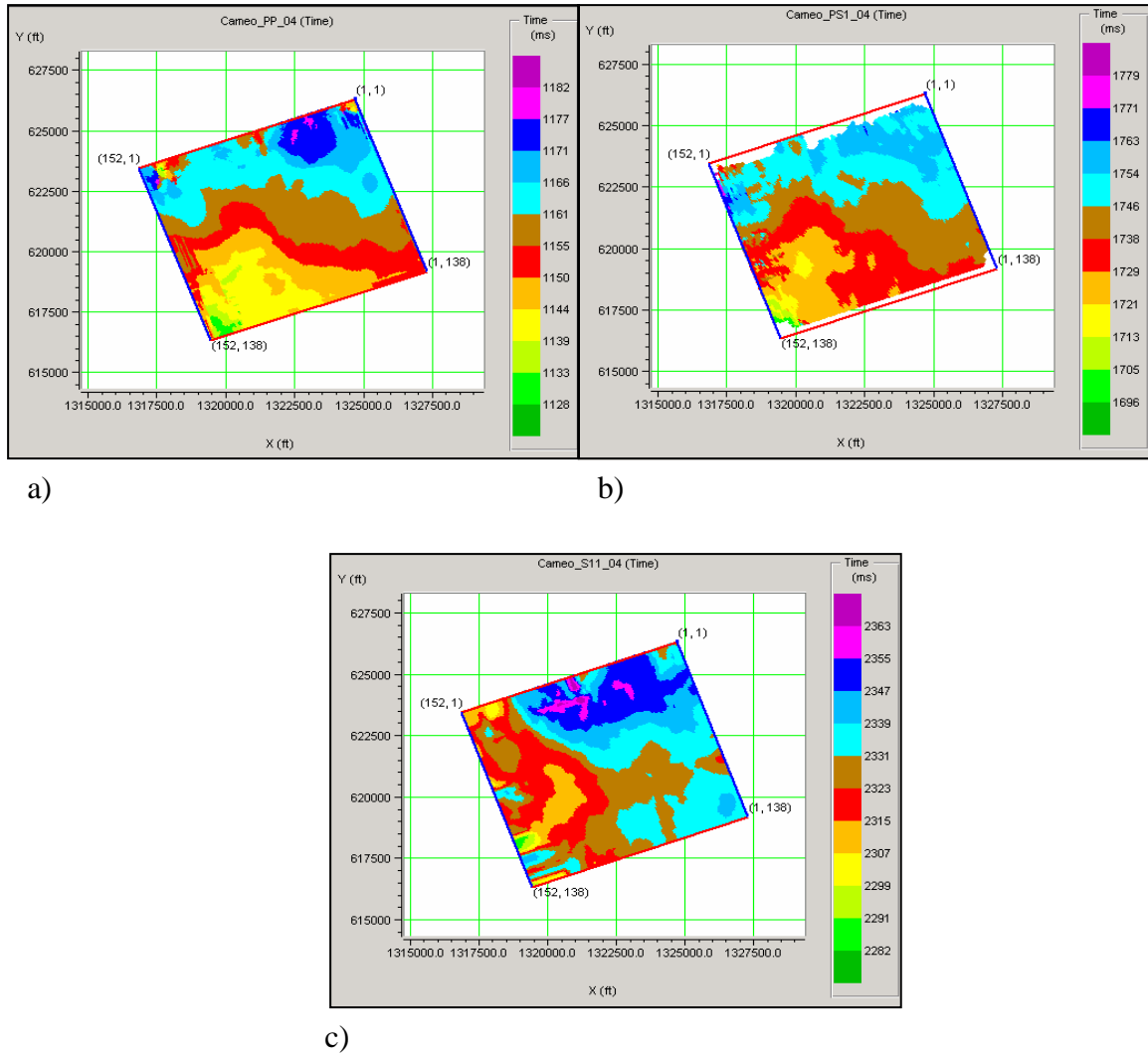


Figure 1.15 Time structure of the bottom of the reservoir, CAMEO-coal horizon. The horizon was picked on: a) compressional wave data; b) converted wave data; c) shear wave data.

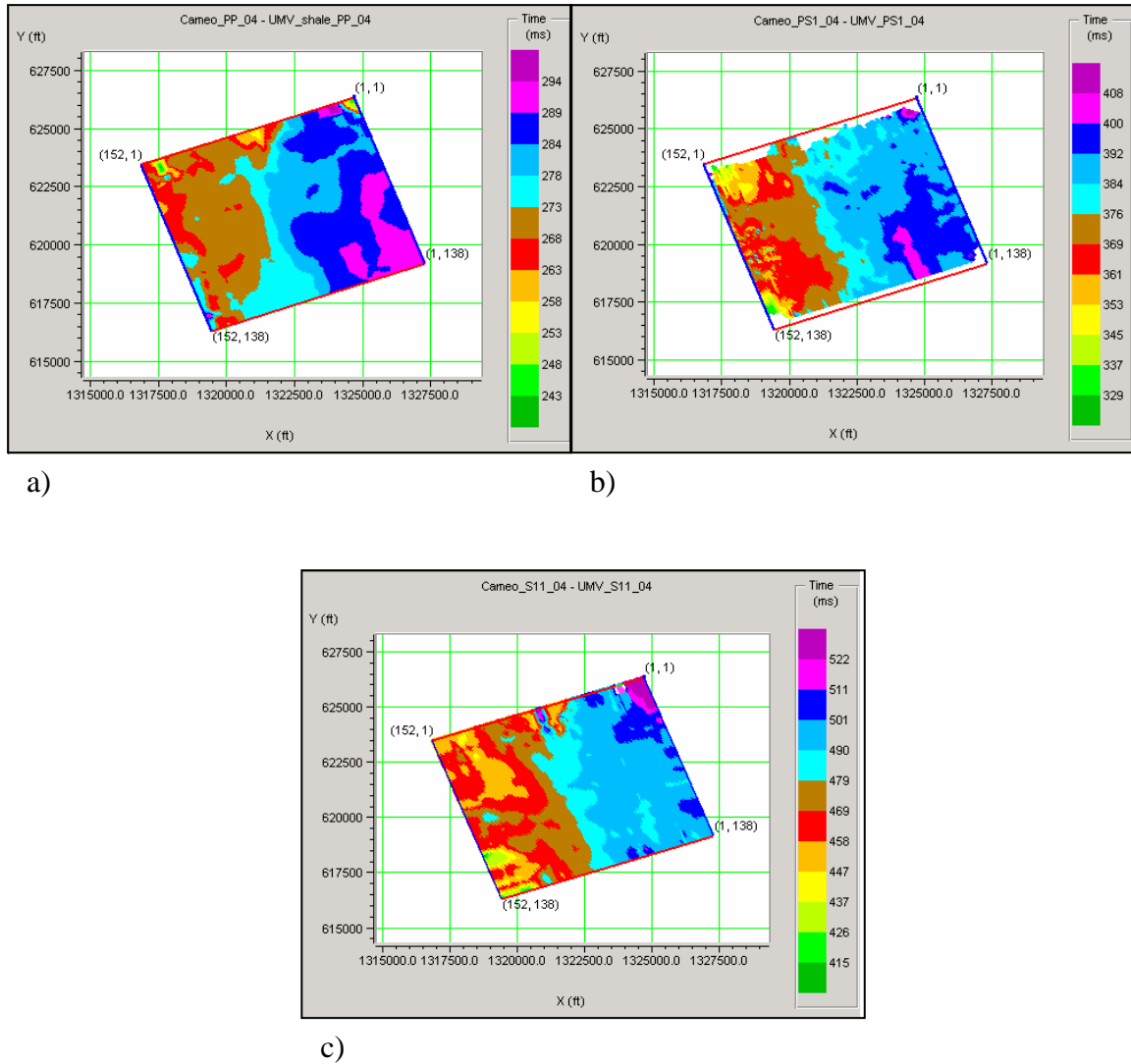


Figure 1.16 Isochron between the top and the bottom of the reservoir. The difference was estimated on: a) compressional wave data; b) converted wave data; c) shear wave data.

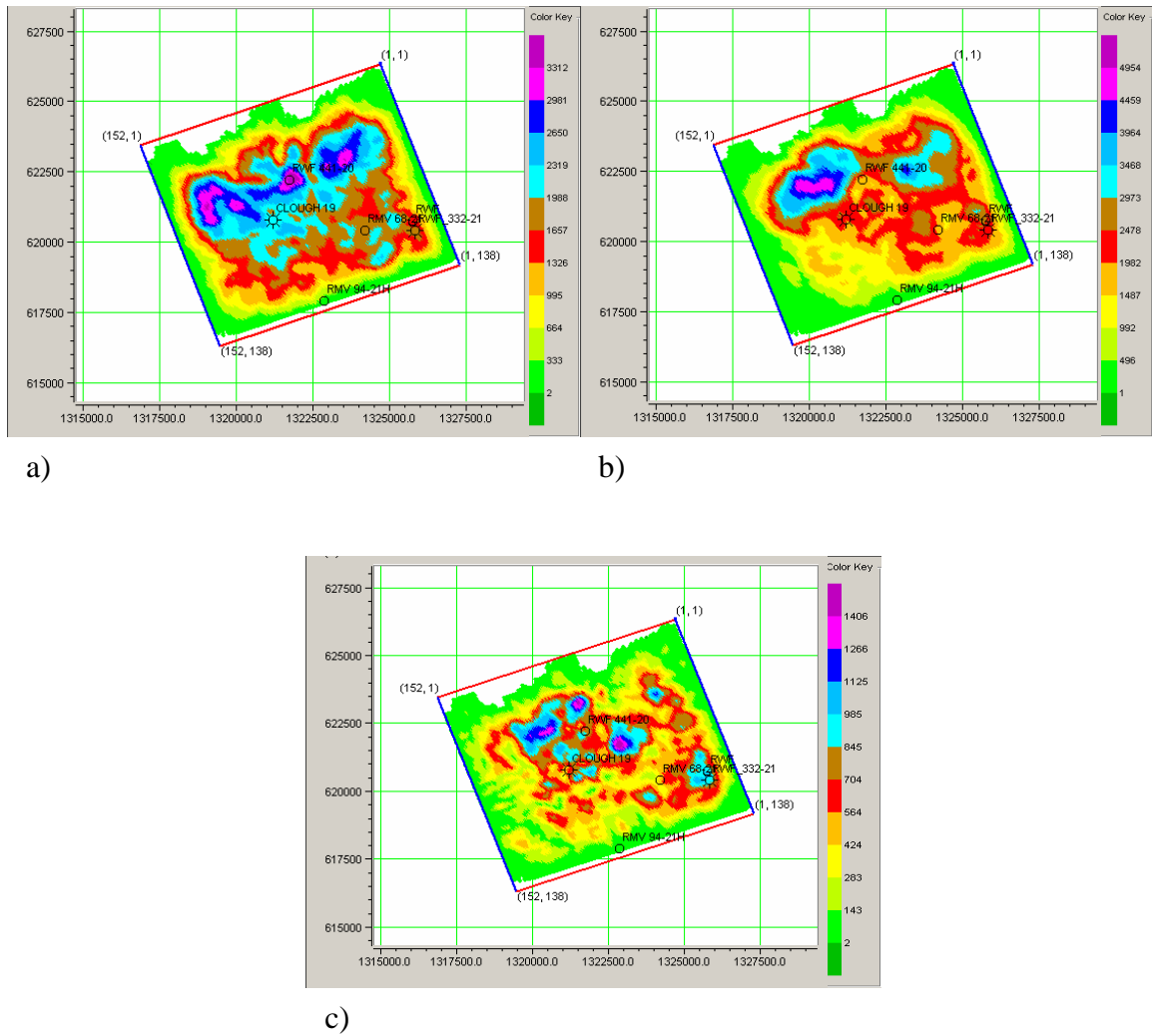


Figure 1.17 Signal RMS amplitude maps estimated from PP wave data within the window size of 10 ms. The data displayed: a) UMV horizon; b) Cameo horizon; c) Middle of the reservoir at 1000 ms in PP time.



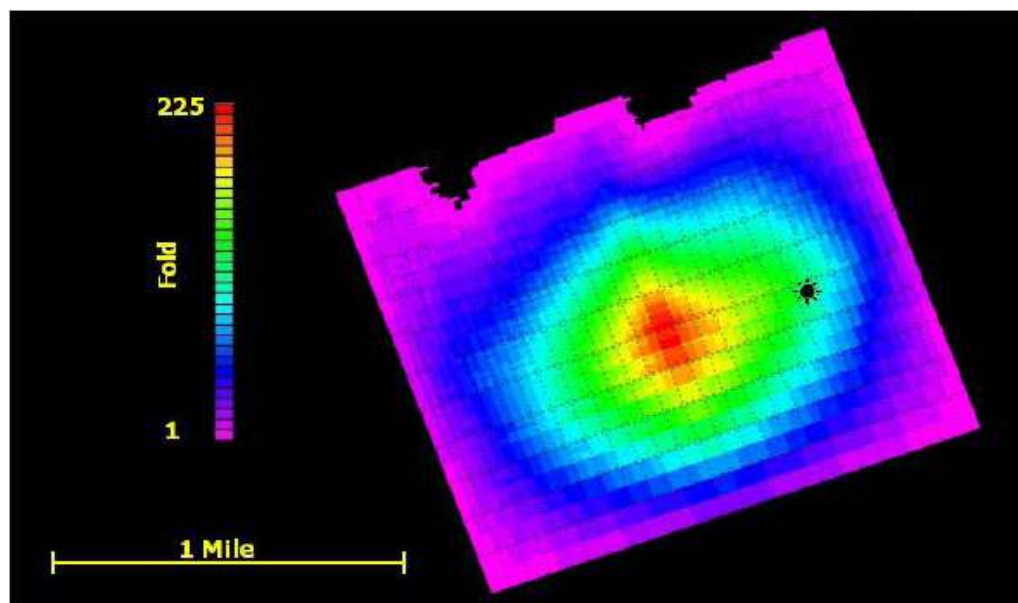


Figure 1.18 P-wave fold for all offset, RCP 2003 survey (Jansen, 2005).

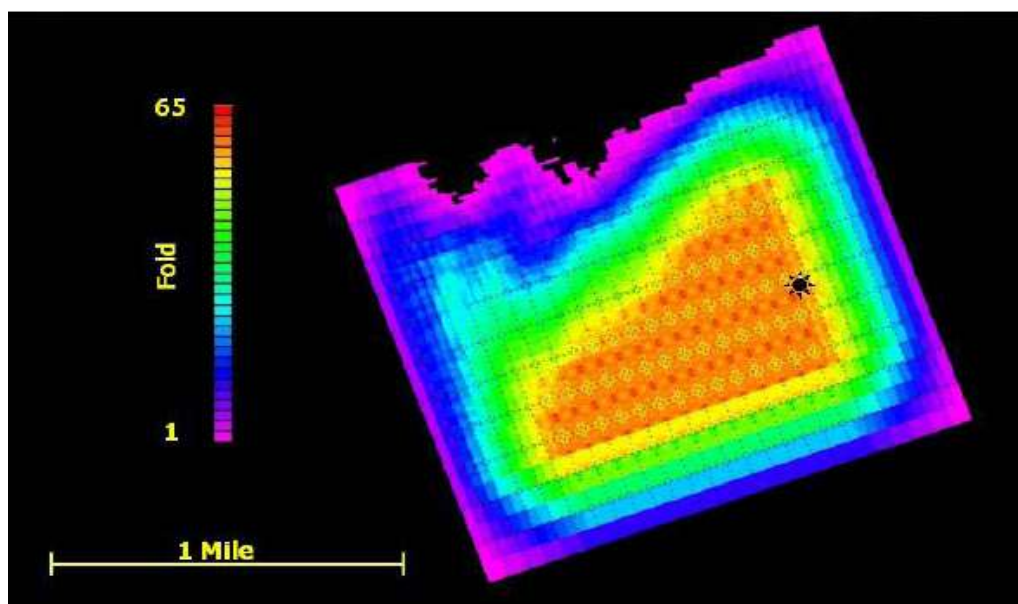


Figure 1.19 Usable S-wave fold with 4,000 ft maximum offset, RCP 2003 survey (Jansen 2005).

## **CHAPTER 2**

### **METHODOLOGY FOR TRAVELTIME-BASED $V_p/V_s$ ESTIMATION**

#### **2.1 Chapter Introduction**

I demonstrate a workflow for interval  $V_p/V_s$  estimation from traveltime of seismic data. This chapter covers synthetics modeling, well and seismic data correlation in time domain, wavelet extraction and depth-to-time curve generation. The interval  $V_p/V_s$  estimates from two way travel time conclude this chapter.

#### **2.2 Workflow For Interval $V_p/V_s$ Estimation**

Described in this section are the procedures taken to obtain an interval  $V_p/V_s$ . Multicomponent seismic data, including compressional, fast shear S11 and fast converted shear PS1 are used in the workflow for interval  $V_p/V_s$  estimation (Figure 2.1). The starting point is the well tie process involving three steps: modeling of synthetic seismograms, wavelet extraction and correlation. Synthetic traces are the function of reflectivity, calculated from velocity and density logs, and a wavelet. Through iterative steps, I improve the shape of the wavelet, until satisfying results (large correlation coefficient between synthetic and actual seismic traces, constant-phase waveform of the wavelet) are obtained. Since log and seismic data have different vertical scale (logs are registered in depth, while seismic is in time), the log tie to seismic is also a procedure of depth-to time curve generation. If this curve is estimated for each of the wave modes, the vertical rescaling becomes available. More exact time domain conversion can be performed after identifying reflection interfaces. In the next step of the workflow I complete the structural interpretation of the main horizons on each time section. To correspond all three seismic volumes in the same time domain, the depth equivalent

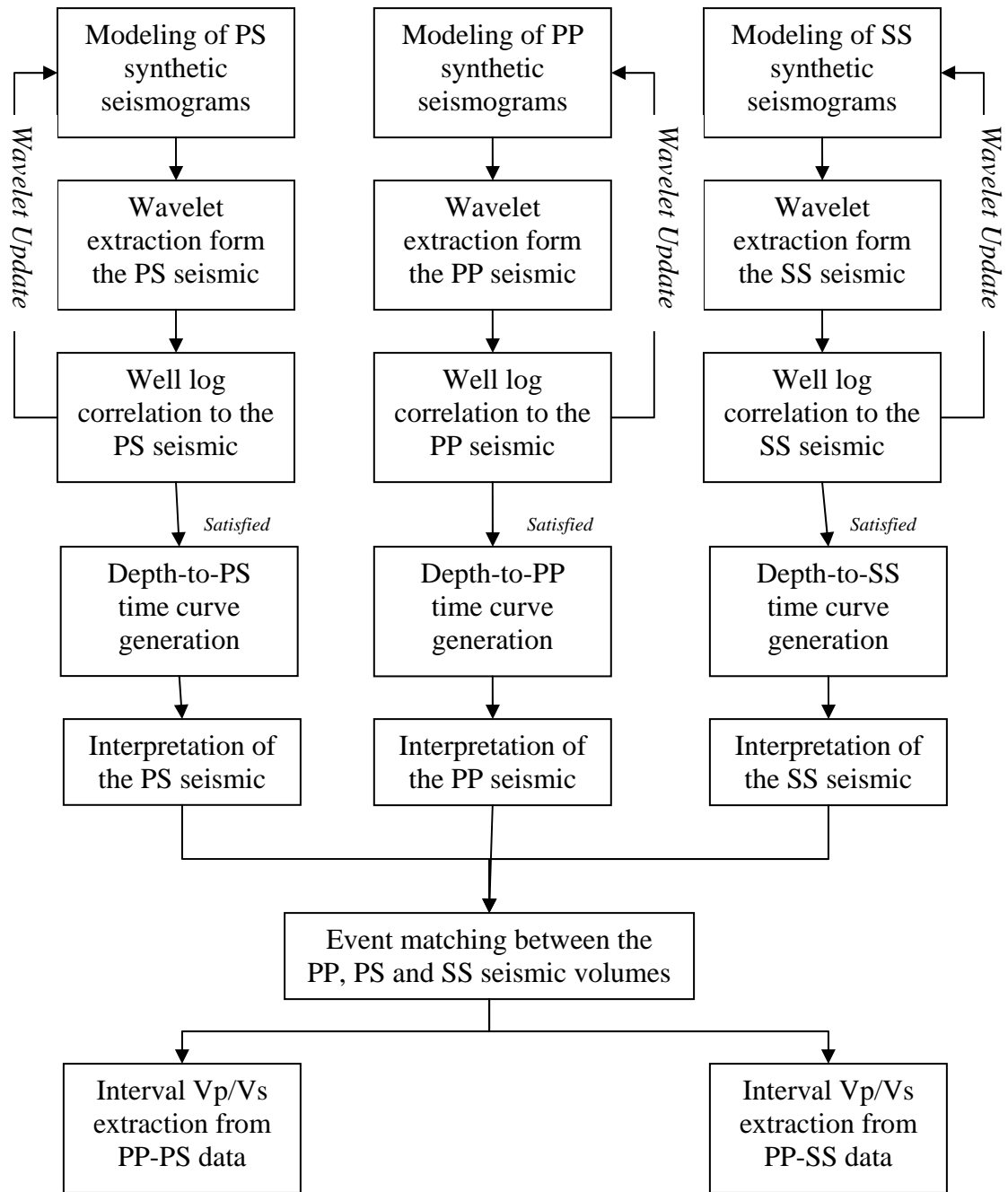


Figure 2.1 General workflow chart for interval Vp/Vs estimation.

seismic reflectors (the reflectors that correspond to the same depositional events) are needed to be matched and calibrated. This enables vertical time rescaling of the events and interval  $V_p/V_s$  estimation from both data sets in combination PP-SS and PP-PS.

Generalizing the described workflow, I estimate two important parameters – seismic wavelet and depth equivalent horizons.

### **2.3 Well Correlation To Multicomponent Seismic Data**

The presented workflow involves modeling of PP, PS and SS data and generation of synthetic seismograms from sonic and density logs. An essential part of this procedure is to identify main horizons and to find the wavelet, which refers to a relatively short, digitized transient waveform. The seismic wavelet is the link between seismic data (traces) on which interpretations are based and the geology (reflection coefficients) that is being interpreted (Henry 1997). The seismic wavelet can change both laterally and spatially in the subsurface for a number of reasons: near surface effects, frequency-dependent absorption etc. I make the assumption that the wavelets I derive for each of the wave modes are time and space invariant within the interval of interest because of the relatively small area of focus.

The procedure of extracting the wavelet and generating synthetic seismograms is based on the convolutional model, where reflectivity is convolved with some bandlimited wavelet and some noise is added. It can be written as:

$$T = W * R + N , \quad (2.1)$$

where:

T – seismic trace,

W – source wavelet,

R – reflection coefficient,

N – random noise.

It is assumed that the noise is random and uncorrelated with the signal. Obviously, to extract the wavelet, a wavelet must be known. The initial wavelet is statistically generated by the program (Hampson & Russell). This initial guess is a zero-phase wavelet with the amplitude spectrum derived from the seismic data. After synthetic traces are generated, they are compared with the actual seismic traces. Correlation of two traces updates the synthetics. Since reflectivity, calculated from the well logs stays constant, the only parameter that changes is the wavelet. Then, the new wavelet is applied and synthetics are recalculated. Thus, the wavelet extraction is an iterative process.

With the extracted ideal wavelet, a zero-phase synthetic seismogram can be derived and compared with the actual seismic data. This procedure is important for identifying seismic reflectors by correlating them to the well data.

### **2.3.1 Well Tie Of PP Seismic Data**

The main bounding horizon events (top UMV shale and Cameo coal) can easily be distinguished on conventional P-wave time section by stronger amplitudes (see Chapter 1 Figure 1.11). Figure 2.2 illustrates log data from well RWF 332-21 (see well location in Chapter 1 Figure 1.10) and the seismic data near the wellbore. With the well tie software (Hampson & Russell) capability of vertical stretching and squeezing logs, I update depth-to-time curve and perform an overall correlation with the seismic data. The tops of UMV and Cameo are correlated with the interpreted earlier horizons UMV\_PP\_04 and Cameo\_PP\_04 (see Chapter 1), representing the same stratigraphic units. The blue trace within the Figure 2.2a is a synthetic trace calculated using the sonic and density logs and an extracted wavelet. After selecting and matching corresponding events on the synthetic and composite traces (red trace), which are the average of well neighbored seismic traces, two more horizons are picked MSVRD\_PP\_04 and Coal\_D\_PP\_04, representing the top of Williams Fork Formation and top of Iles Formation. The shown on Figure 2.2b the extracted P-P constant phase wavelet has the

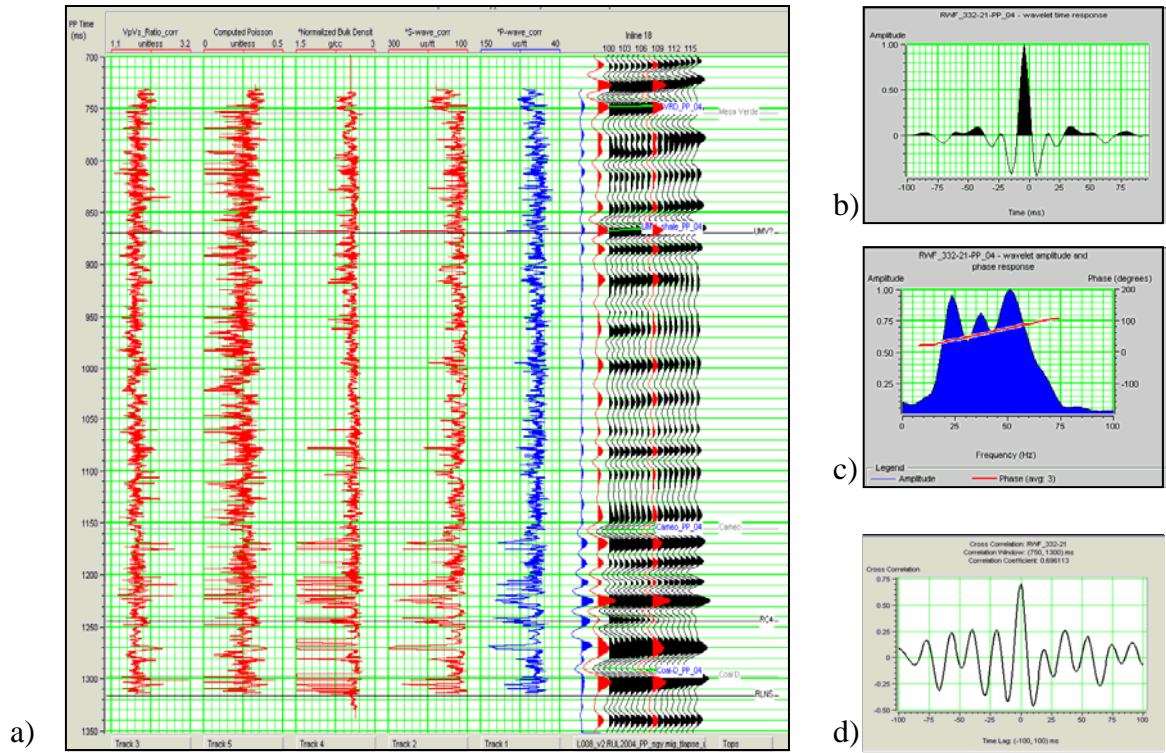


Figure 2.2 Well tie to the PP seismic data. a) The portion of the time section is correlated with the P-wave well log by matching the events on composite trace (red curve) and synthetic trace (blue curve); b) The extracted wavelet with a constant phase in the time domain; c) Frequency domain of the wavelet; d) Cross correlation plot demonstrating a zero-phase symmetric waveform at zero time with correlation coefficient of about 0.70.

following parameters:

wavelet length = 200 ms,

taper Length = 25 ms,

sample Rate = 2 ms.

The bandwidth of the wavelet is from 10 to 75 Hz (Figure 2.2c). A cross correlation plot on Figure 2.2d demonstrates a symmetric shape with a peak at about zero time. The correlation coefficient is 0.70 for the main reservoir interval.

### **2.3.2 Well Tie Of SS Seismic data**

I apply the same procedure of well log correlation to pure shear wave data (Figure 2.3) resulting in generation of an extracted wavelet with a bandwidth from 5 to 25 Hz. The results of cross correlation plot show the correlation coefficient for S-wave data of 0.73 for the main reservoir interval.

### **2.3.3 Well Tie Of PS Seismic Data**

Pure mode PP and SS data can be correlated with either P-wave or S-wave components of a dipole sonic log applying the zero-phase synthetic. In the case of a PS-wave to obtain a synthetic response of converted wave data, a range of offsets, similar to those used during the data processing, must be stacked. According to the geophysicists from Veritas (personal discussion), who were involved in the processing of the Rulison data, the maximum offset used is 10905 feet (3324 m). With this information the algorithm implemented in ProMC package of Hampson and Russell software creates PS offset synthetic seismogram with the range of offsets from 1636 to 9900 ft. After some iteration, I obtain a 0.75 correlation coefficient for the main reservoir interval between log and seismic data (Figure 2.4).

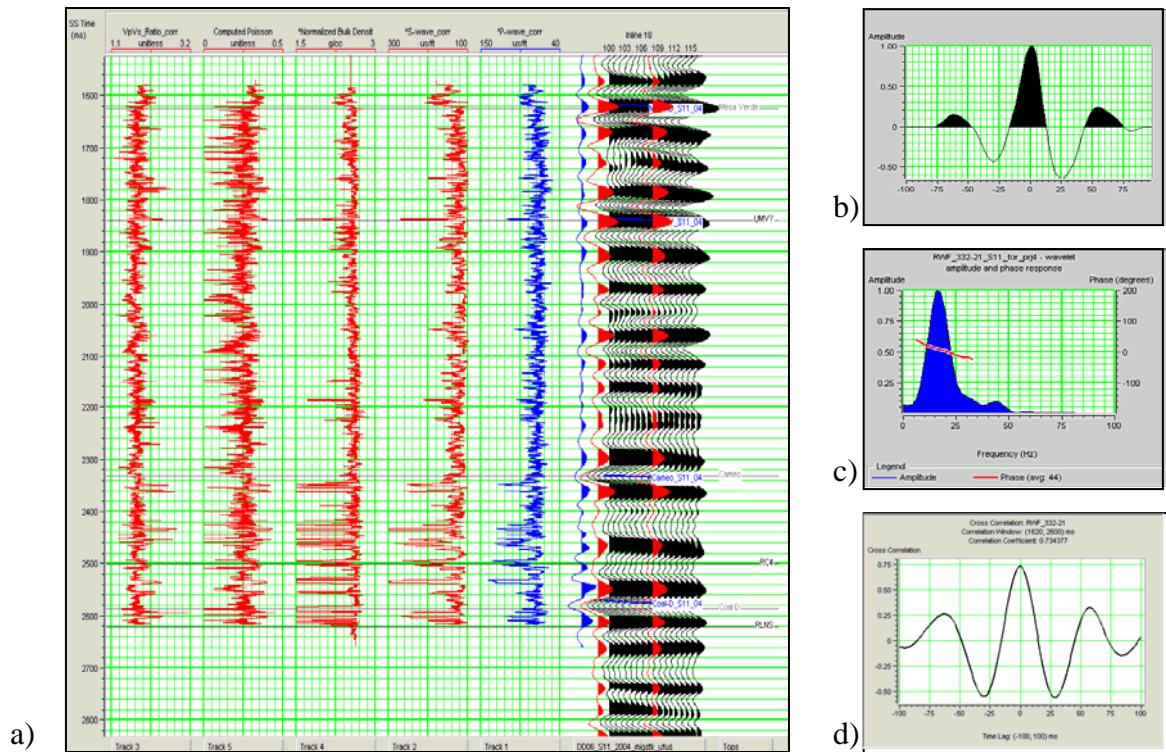


Figure 2.3 Well tie to the SS seismic data. a) The portion of the time section is correlated with the S-wave well log by matching the events on composite trace (red curve) and synthetic trace (blue curve); b) The extracted wavelet with a constant phase in the time domain; c) Frequency domain of the wavelet; d) Cross correlation plot demonstrating a zero-phase symmetric waveform at zero time with correlation coefficient of about 0.73.



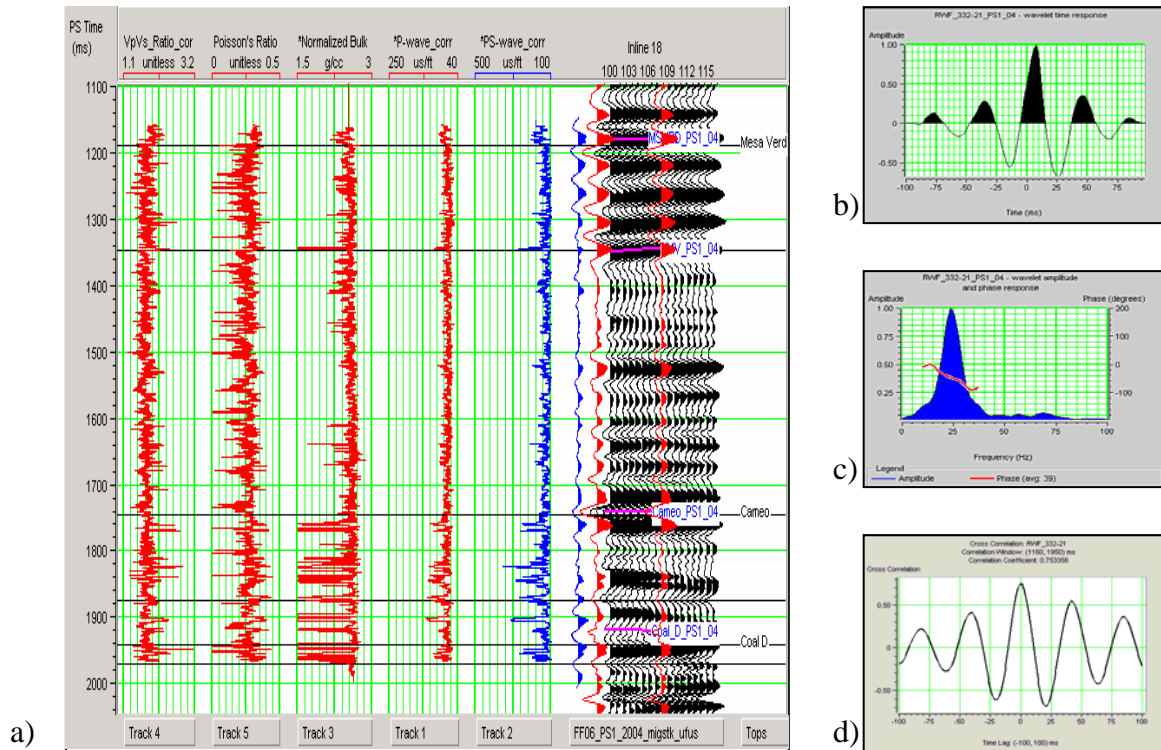


Figure 2.4 Well tie to the PS seismic data. a) The portion of the time section is correlated with the S-wave well log by matching the events on composite trace (red curve) and synthetic trace of stacked offset range (blue curve); b) The extracted wavelet with a constant phase in the time domain; c) Frequency domain of the wavelet; d) Cross correlation plot demonstrating a zero-phase symmetric waveform at zero time with correlation coefficient of 0.75.

## **2.4 Interval Vp/Vs Estimation**

By tying the well logs to the seismic, I create a depth-to-time curve, which specifies the transformation factor between time and depth scales for all three seismic wave types, PP, SS and PS. This also enables me to perform time domain conversion, which is based on the P- and S-wave velocity logs from well RWF 332-21 tied to seismic in different time modes.

When the consistent reflectors conforming to UMW and Cameo events are picked on multicomponent seismic surveys, it is possible to estimate interval Vp/Vs from the traveltimes of the corresponding horizons. Basically,

$$\left[ \frac{V_P}{V_S} \right]_{PP,PS} = \frac{2\Delta t_{PS} - \Delta t_{PP}}{\Delta t_{PP}}, \quad (2.2)$$

$$\left[ \frac{V_P}{V_S} \right]_{PP,SS} = \frac{\Delta t_{SS}}{\Delta t_{PP}}, \quad (2.3)$$

where:

$\left[ \frac{V_P}{V_S} \right]_{PP,PS}$  - velocity ratio estimated from PP- and PS-wave data,

$\left[ \frac{V_P}{V_S} \right]_{PP,SS}$  - velocity ratio estimated from PP- and SS-wave data,

$\Delta t_{PS}$  – two-way travel time difference between two events in PS time,

$\Delta t_{PP}$  – two-way travel time difference between two events in PP time,

$\Delta t_{SS}$  – two-way travel time difference between two events in SS time.

Thus, interval Vp/Vs can be estimated if either converted wave (eq. 2.2) or pure shear wave data (2.3) are available. Nine-component seismic data used allow me to obtain Vp/Vs results from two data sets – PP-S11 and PP-PS1. The investigation of the

interval Vp/Vs maps is presented in Chapter 5.

The depth equivalent horizons are defined as the horizons that if in depth overlay each other. The seismic data are in time scale. Figure 2.5 represents the seismic volumes in the same PP time domain after well log correlation has been done and interval Vp/Vs has been estimated. Ideally, when the right domain conversion is applied, the depth equivalent horizons must match each other. This is demonstrated in Figure 2.5.

The correct interval Vp/Vs estimation depends on correctly picked horizons on all seismic volumes included in the calculation of traveltime difference. If the interpretation has correctly identified depth-equivalent reflectors, the calculated Vp/Vs values will represent interval Vp/Vs over a vertical seismic portion independently of any a priori velocity information. There is always a likelihood that time horizons may be picked incorrectly. To avoid some misinterpretations and miscalculations of Vp/Vs, it is meaningful to pick strong continuous reflectors on the whole survey and to use dipole logs for assistance.

The reservoir interval is about 2,000 ft in thickness. An interval Vp/Vs estimated between UMV-shale and Cameo-coal is over 2,000 ft. The workflow explained earlier in this chapter is designated to estimate Vp/Vs that would provide more detailed information within the reservoir interval.

## **2.5 Summary**

The workflow of the current research is described. The log and multicomponent seismic data correlation is critical to the process of Vp/Vs determination.

Interval Vp/Vs is calculated from the traveltime registration at corresponding time horizons from multicomponent seismic data. Two combinations of data sets are used for this purpose – PP-S11 and PP-PS1. The obtained data are further investigated for general Vp/Vs distribution and correlation with additional information in Chapter 5.

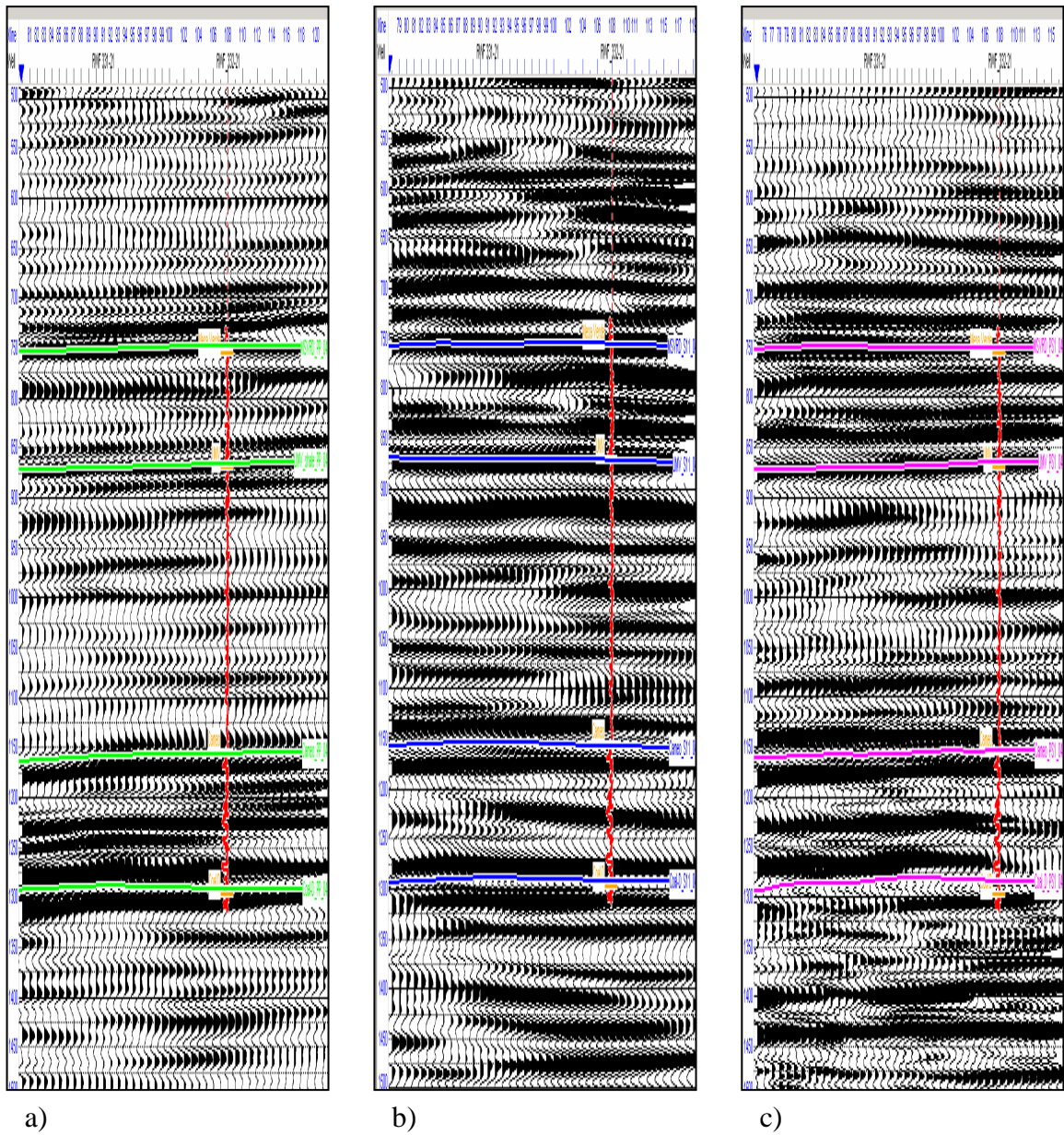


Figure 2.5 Seismic time sections in PP time domain : a) Compressional wave data; b) Shear wave data; c) Converted wave data. With the right  $V_p/V_s$  all the picked horizons must be lined up.

## **CHAPTER 3**

### **METHODOLOGY FOR SEISMIC IMPEDANCE INVERSION OF MULTICOMPONENT SEISMIC DATA**

#### **3.1 Chapter Introduction**

Unlike the procedure of interval  $V_p/V_s$  estimation introduced in the previous chapter, which is based on traveltimes measurements, here I use a different approach based on seismic amplitude inversion for impedance. The chapter covers main principles of the developed workflow and applied inversion algorithm. The outputs from inversion are the P-impedance volume and two S-impedance volumes estimated from SS and PS data. The quality control of the results proves the accuracy of the impedance volumes.

#### **3.2 Frequency Bandwidth Of The Seismic Data**

Before considering the basic steps of the inversion algorithm, I need to specify the frequency bandwidth of the multicomponent seismic data. This step is not indicated in the workflow and might be skipped if applied on different data sets. However, for the purpose of investigation I introduce the following procedure. The presented study shows that P-wave data have the broadest range of frequencies among multicomponent data used. To make the bandwidth of all three, PP, S11 and PS1 seismic data comparable, I apply a bandpass filter 0,0,50,60 to the compressional wave data to cut the high frequency content (Figure 3.1). Transformed to different time domains, filtered P-wave data display similar frequency bandwidth to those of the originally registered PS and SS time reflections. The comparisons on Figure 3.2 demonstrate the frequency spectra of the PS and SS signals and comparable frequency range of filtered P-wave data in different time domains (PS and SS). Here and in all subsequent computations I use the high

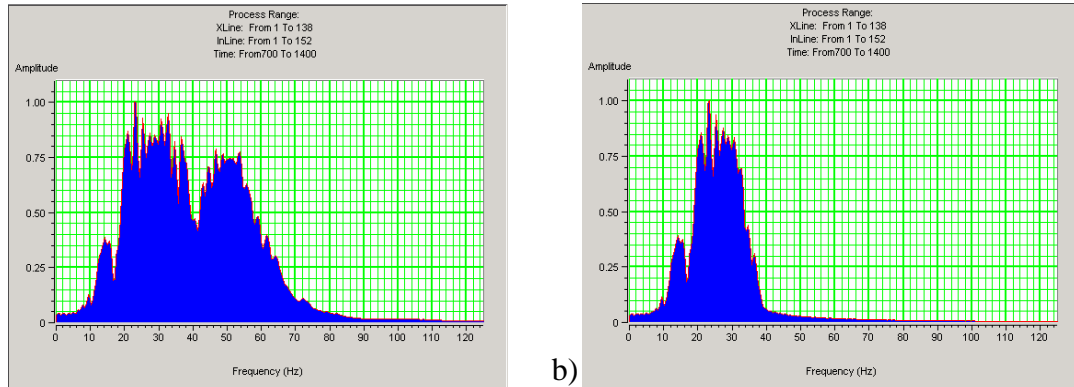


Figure 3.1 Frequency domain of compressional wave data in PP time: a) original unfiltered; b) after the high frequency was cut.

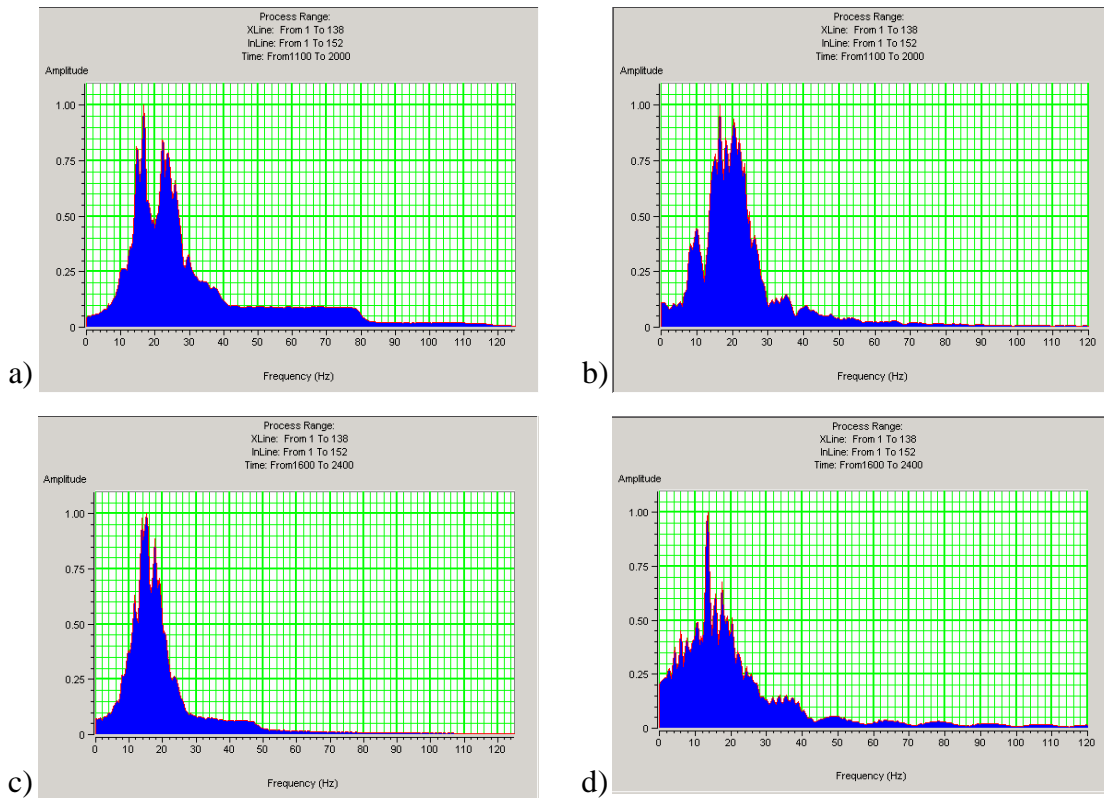


Figure 3.2 Frequency domain of multicomponent seismic data: a) converted wave data in PS time; b) filtered compressional wave data in PS time; c) shear wave data in SS time; d) filtered compressional wave data in SS time.

frequency filtered P-wave data. This brings all the data to the point when the bandwidth does not differ much from one data set to the other and, therefore, the output  $V_p/V_s$  is not influenced by the high frequency content of either one of the input seismic.

### **3.3 Workflow For Impedance Derived $V_p/V_s$ Estimation**

Figure 3.3 captures the main process steps and outputs from these processes for the velocity ratio derivation from seismic amplitudes. I accomplish the impedance inversion through model based inversion algorithm for each input data in the original time domain utilizing the extracted wavelet. The software package, Hampson and Russell, including STRATA and ProMC is used for this purpose. The outputs are P-impedance volume from PP-wave data and two S-impedance volumes from SS- and PS-wave data. This creates two data sets for  $V_p/V_s$  estimation, PP-SS and PP-PS. The time rescaling of the inversion results to the equal time domain followed by the ratio of P- and S-impedance volumes exhibit a high resolution  $V_p/V_s$  attribute volume. The final step involves depth conversion of the estimated  $V_p/V_s$  volumes.

Assumptions involved in the workflow include:

- The extracted wavelet for each wave mode is assumed to be constant in time and space over the reservoir interval;
- The vertical time rescaling of multicomponent seismic data correctly positions picked horizons and intermediate events in different time domains.
- The rotation during the data processing recovered fast shear wave information from both pure S11 and converted PS1 seismic reflection data to handle a fixed single orientation of fast shear in the subsurface.

The current work meets all the mentioned above assumptions. The small area of the investigation justifies the first assumption. The time domain transformation is performed within a large vertical section, but as demonstrated later, the correctly picked time horizons contribute to the appropriate positioning of the registered on multicomponent seismic data events in different time domains. The constant angle

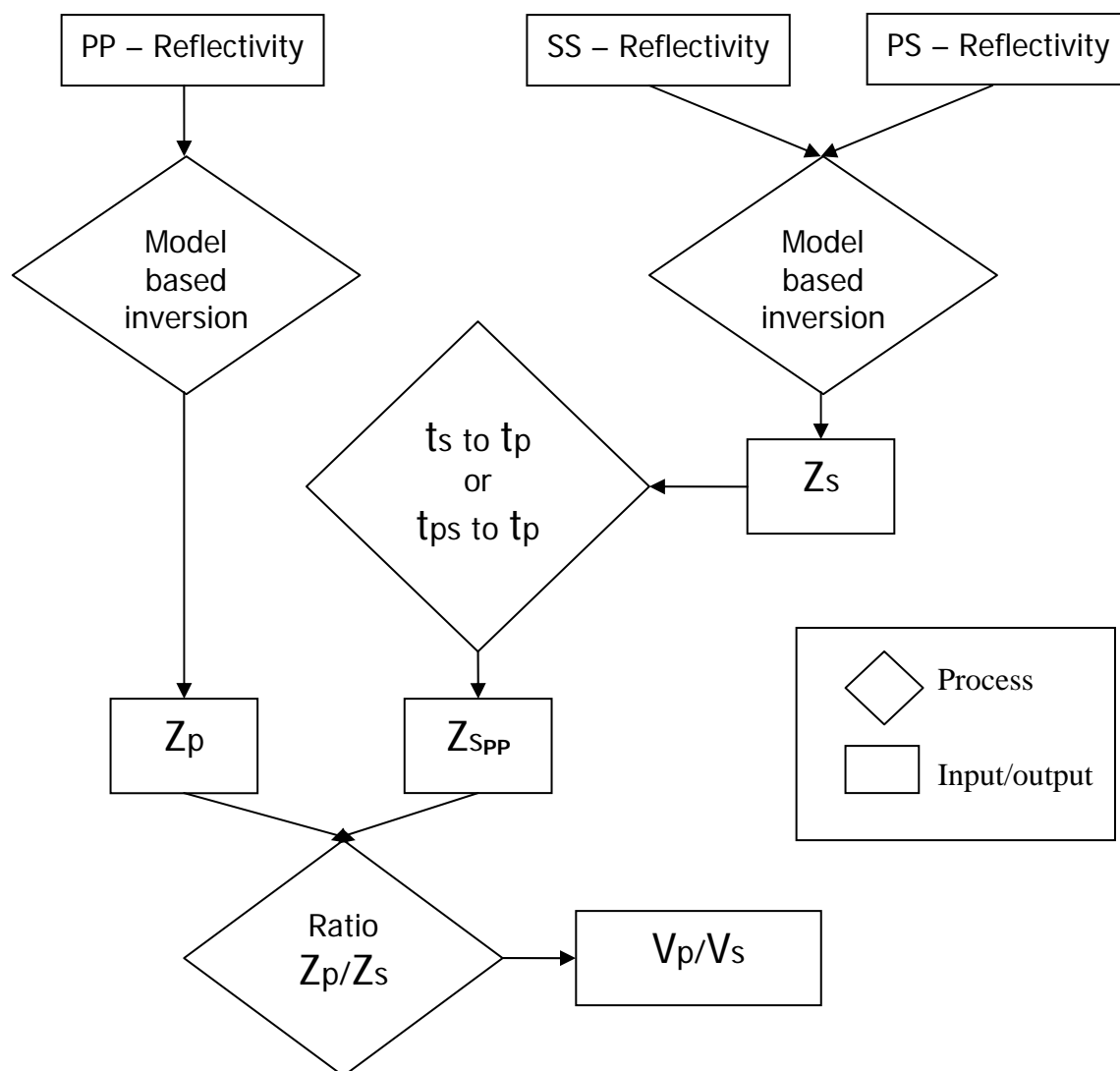


Figure 3.3 Workflow chart for impedance derived  $V_p/V_s$  estimation.



chosen for Alford rotation is N45W. The results from converted wave and VSP data agree with this. Shown in Figure 3.4 is a regional stress map comparing the Rulison result to publicly available data, usually obtained from borehole breakouts. A similar direction of stress is observed at Rulison as determined from the fast shear direction computed through the Alford rotation algorithm.

More detailed information for each of the workflow steps is provided in the later chapters. This chapter covers interval Vp/Vs extraction from PP-S11 and PP-PS1 seismic data.

### **3.4 Model-Based Inversion Technique**

The inversion I use is model-based, the algorithm in software program STRATA, designed by Hampson & Russell. The algorithm is built to iteratively update an impedance model to match synthetically produced traces with original seismic ones.

Impedance is a medium property and reflection coefficient is an interface property. Both these parameters can be calculated from borehole registered data. Seismic provides bandlimited estimations of impedance. Naturally, low frequency information can be obtained from other sources, such as well logs, and added to seismic estimations (Russell 1988). The basic principle of the applied inversion is to create an impedance model from well log data. The model is defined as a series of layers with variable velocity, density, and thickness. Synthetic seismograms based upon this initial model are computed and compared with the actual seismic data. Under the constraints of manually adjusted parameters (average block size, number of iterations, prewhitening, scaler adjustment factor etc.), the model is iteratively updated to obtain the best match with the observed seismic in a least square sense. Figure 3.5 illustrates the basic elements of the model-based inversion.

I test different approaches to model-based inversion to identify the inversion parameters that produces the best results for impedance estimations from the seismic data used. The tests and analysis of the inversion results confirm that final results are more

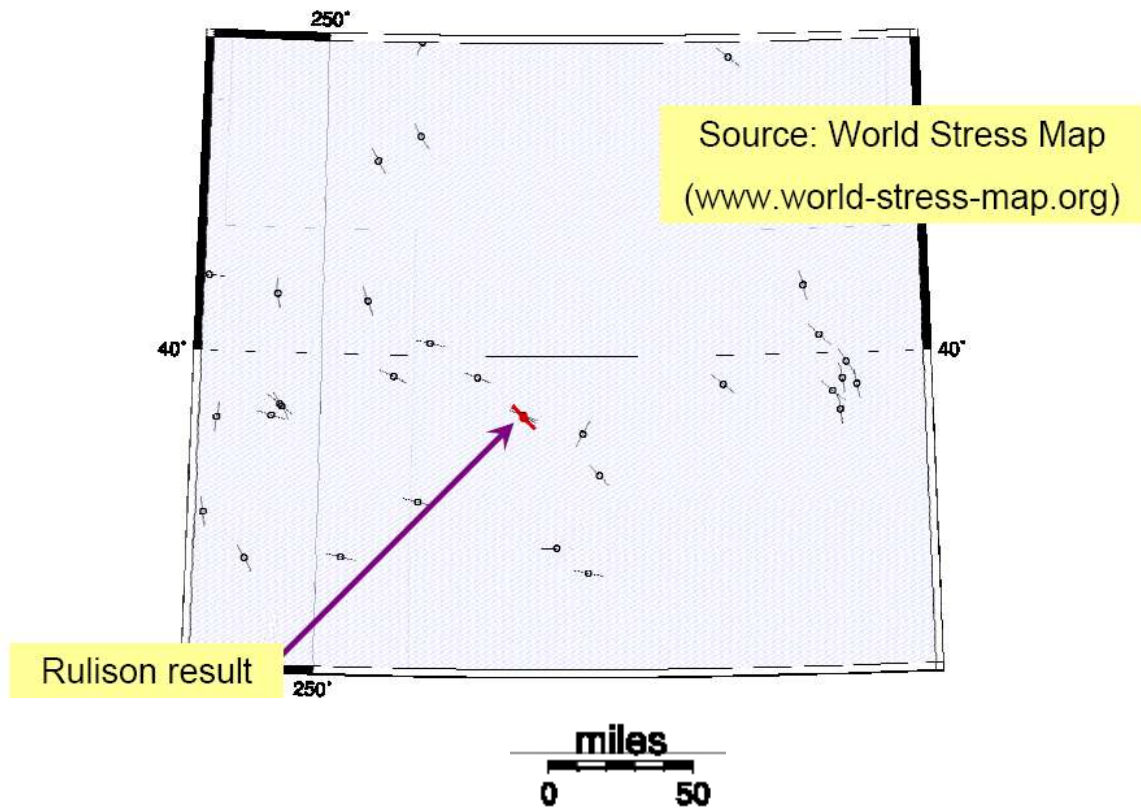


Figure 3.4 Regional stress map ([www.world-stress-map.org](http://www.world-stress-map.org)). Rulison result of N45W rotation agrees with the stress map obtained from borehole breakouts.

robust if the inversion algorithm is applied to the whole interval from the seismic datum to the bottom limit of the target interval. The existence of the log information just within the interval of interest validates the results.

The inversion technique is an iterative modeling scheme, which can be thought of as a geology-based deconvolution since the full reflectivity is extracted (Russell 1988).

Any inversion algorithm, ideally, would produce the same impedance results within the seismic bandwidth as any other inversion techniques. As in any other inversion schemes, the problem of non-uniqueness outside of the seismic bandwidth is present here. A good match can be achieved between modeled and real data but it does

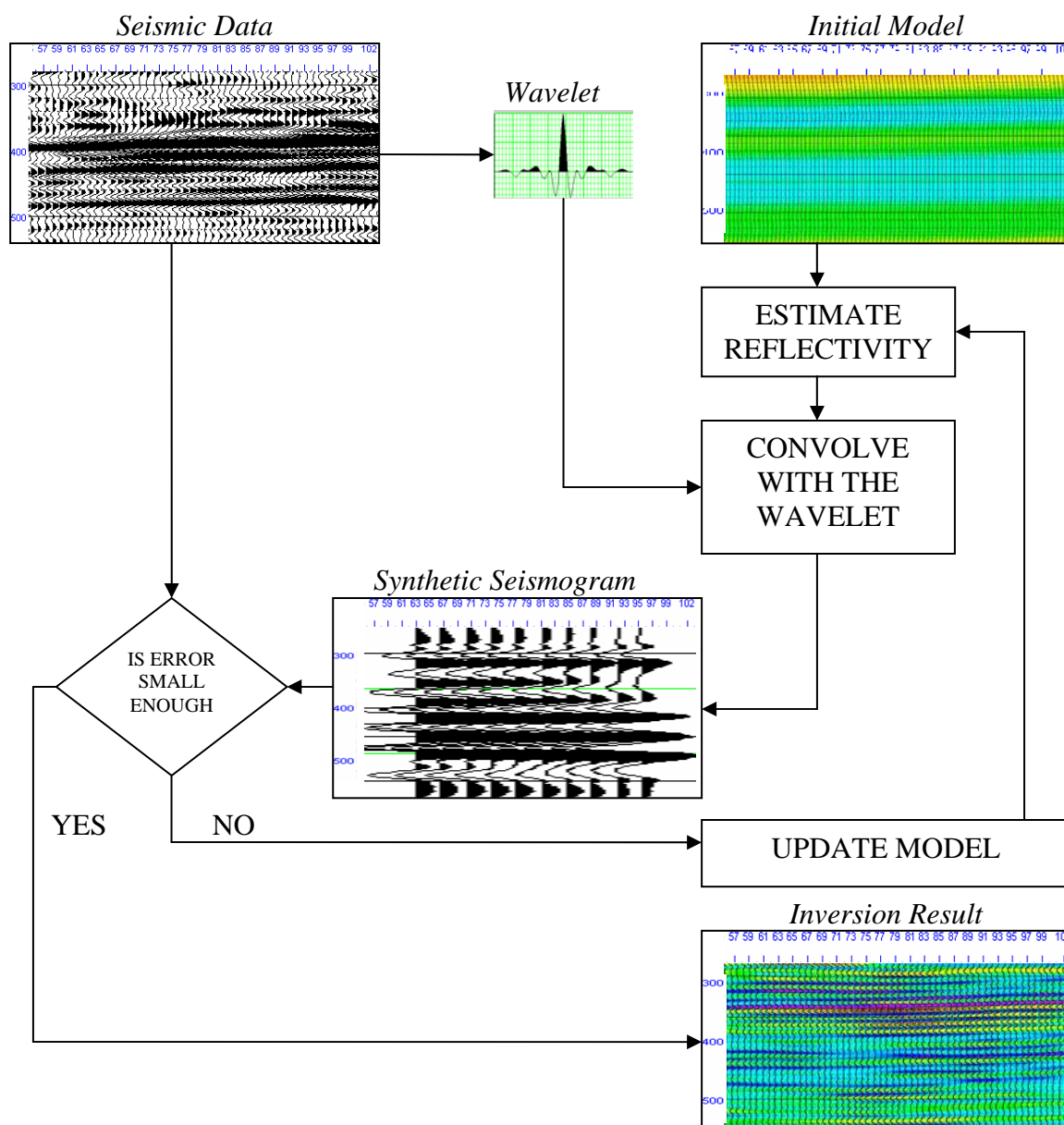


Figure 3.5 Model based inversion flowchart (modified from Russell 1988).

not guarantee the correct impedance volume. Therefore, the inversion process of adding low frequency content to the impedance results is constrained by input data from dipole sonic logs.

Single mode compressional P- wave data are the input for P-impedance estimations. Pure shear S-wave and converted PS-wave data are input for S-impedance volumes computation. I perform a thorough analysis of the resultant impedance traces at the well location and their visual and numerical correlation with well log data. This procedure helps to evaluate the algorithm parameters that would provide the most comprehensive and correct estimation of both P- and S-wave impedances.

### **3.5 Compressional And Shear Wave Data Inversion**

The small area of investigation and horizontal subsurface structure ratifies utilization of a single well. I generate the initial earth model by extrapolating the data from well, RWF 332-21 where compressional and shear wave velocity information was registered in the interval of interest from a dipole sonic log. The extrapolation is constrained by the seismic horizons. The P-wave acoustic impedance model is shown in Figure 3.6. The model is color coded for representation of temporal impedance changes. The values are constant laterally. Figure 3.7 shows the model for S-impedance created from fast S- wave borehole registered velocity. The impedance log, shown as a black curve on the Figures 3.6 and 3.7, is calculated by multiplying velocities from the dipole sonic log and density log.

After the background models are created, I analyze the seismic data in order to adjust parameters for the inversion process. The results of inversion analysis are also valuable for quality control of inverted data, therefore, this can be considered as a QC analysis of the inversion results. Since seismic data are band-limited, log data containing broader bandwidth must be filtered down to the seismic frequency content to validate the correlation. This procedure does not affect the results of inversion because the operator passes the initial model just to estimate the misfit between seismic and synthetics.

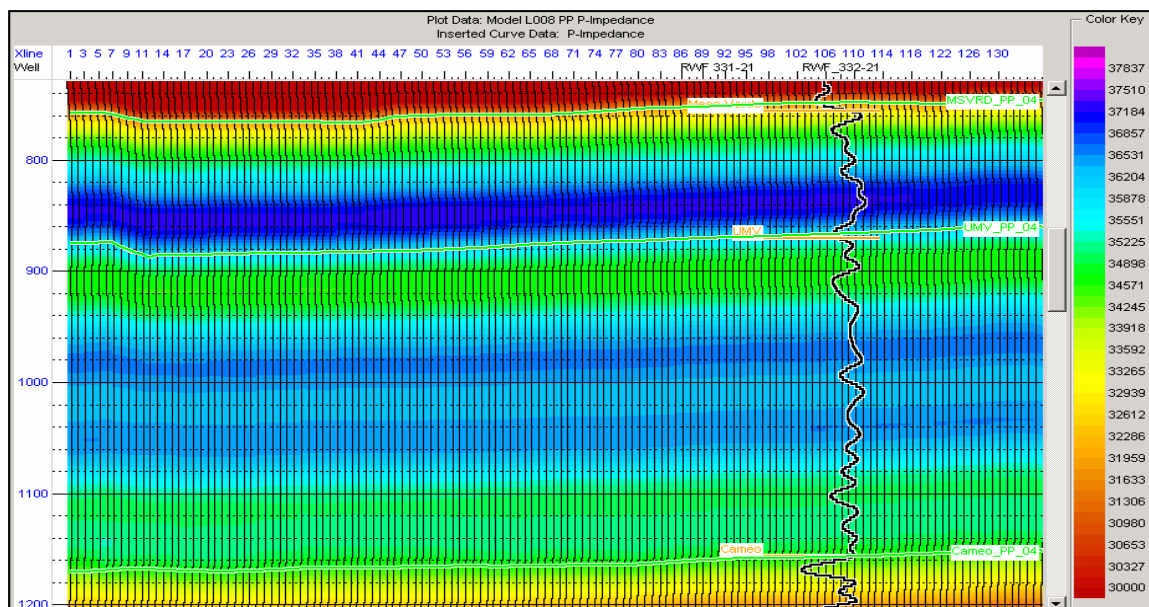


Figure 3.6 P-wave acoustic impedance model within the interval from Mesaverde to Cameo-coal. The black curve is P-impedance estimated from velocity and density logs and filtered to the seismic frequency bandwidth.

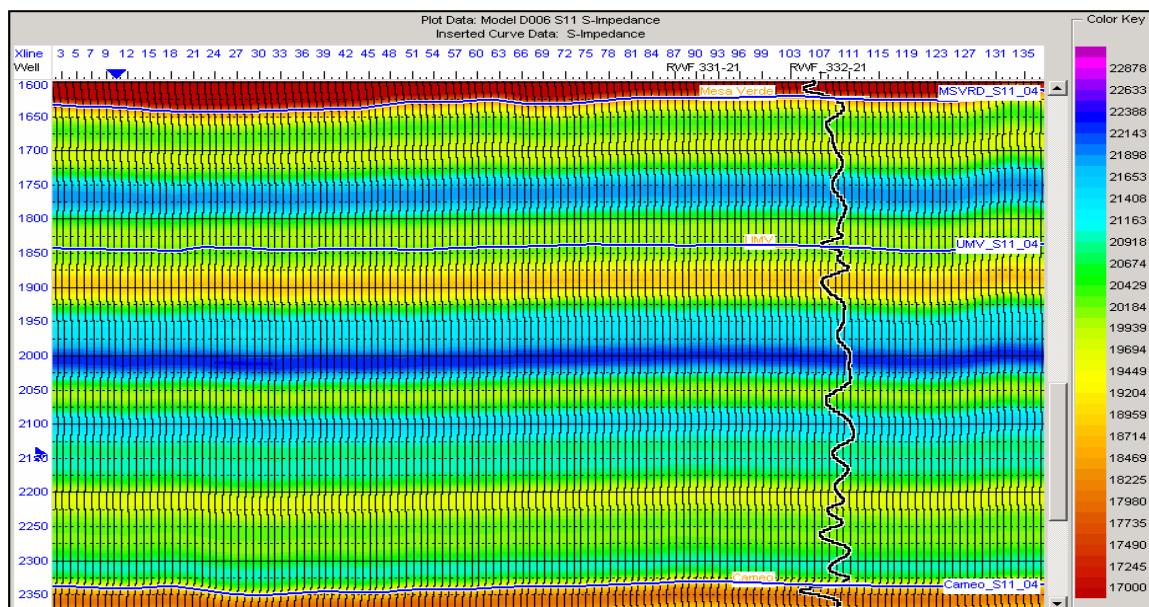


Figure 3.7 S-wave impedance model within the interval from Mesaverde to Cameo-coal. The black curve is S-impedance estimated from velocity and density logs and filtered to the seismic frequency bandwidth.

The QC analysis of impedance results from inversion can be seen in Figure 3.8. The program perturbs the black curve in Figure 3.8 representing the impedance model trace at the well location until a good match between seismic and synthetic traces is achieved. The analysis compares the result of inversion represented by the red curve and log data shown with the blue curve. Thus, after the parameters optimization for P- and S-wave data in the original time domain, I estimate the correlation coefficient for compressional and shear wave data to be about 0.80 and 0.70 respectively. Several zones can be identified where the inversion function produces considerable errors (indicated by arrows in Figure 3.8). This mismatch may be due to the caving that occurs in the coal zones in the upper and lower part of the reservoir and its influence on the sonic log. The other important observation can be made below 1150 ms at figure 3.8a and below 2330 ms at figure 3.8b. This is the coal zone, which produces much lower acoustic impedance than in the section above. Therefore, if the interest arises for the coal interval, it has to be considered and inverted separately from the sand reservoir interval (with inversion parameters adjusted for this specific zone).

Two impedance volumes presented on figures 3.9 and 3.10 are the outcomes from amplitude inversion of stacked and migrated compressional and shear wave seismic data respectively. The inserted curves are log derived P- and S-impedances. The general correspondence of seismic and log signals can be observed on both sections.

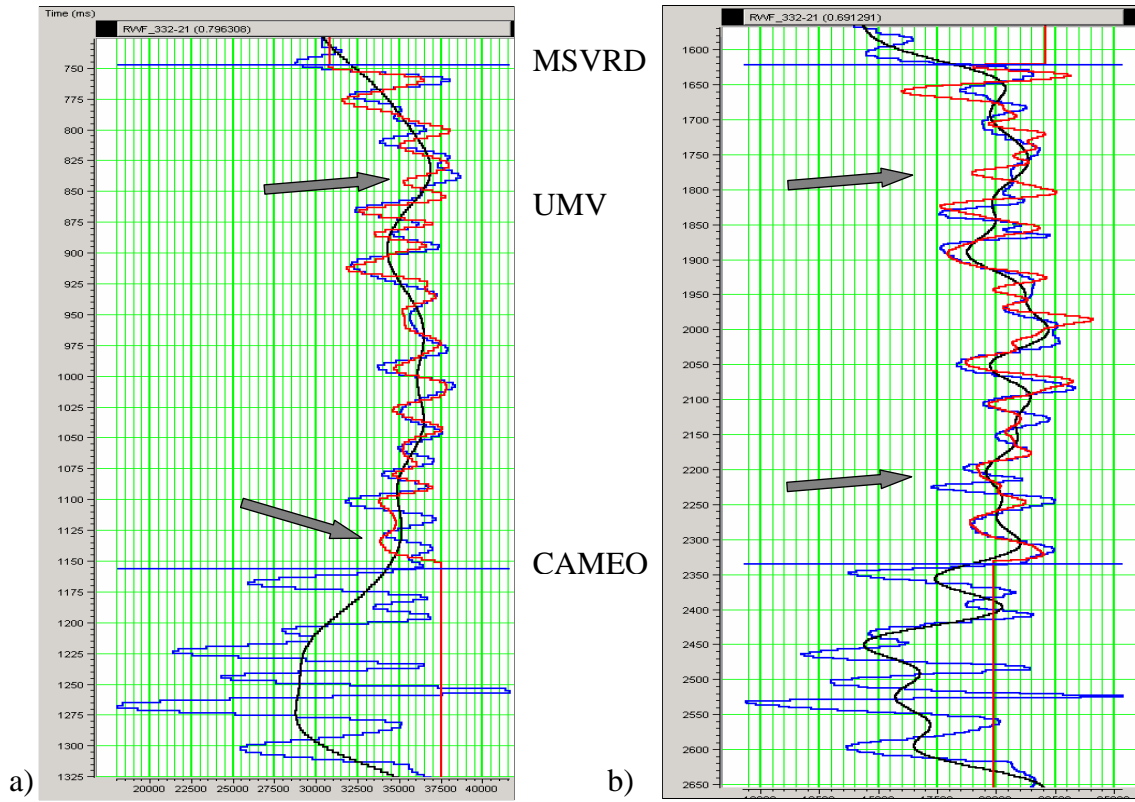


Figure 3.8 Inversion QC analysis of: a) P-wave data in PP time b) S-wave data in SS time. The inverted interval is between MSVRD and CAMEO marks. Blue curve represents impedance estimated from well log. Black curve is the earth model created by extrapolating the well logs. Red curve is the result of inversion. The match between real and estimated acoustic impedance is 0.8 for P-wave data and 0.7 for S-wave data. Arrows indicate the zones of distinguished errors in the inversion results.



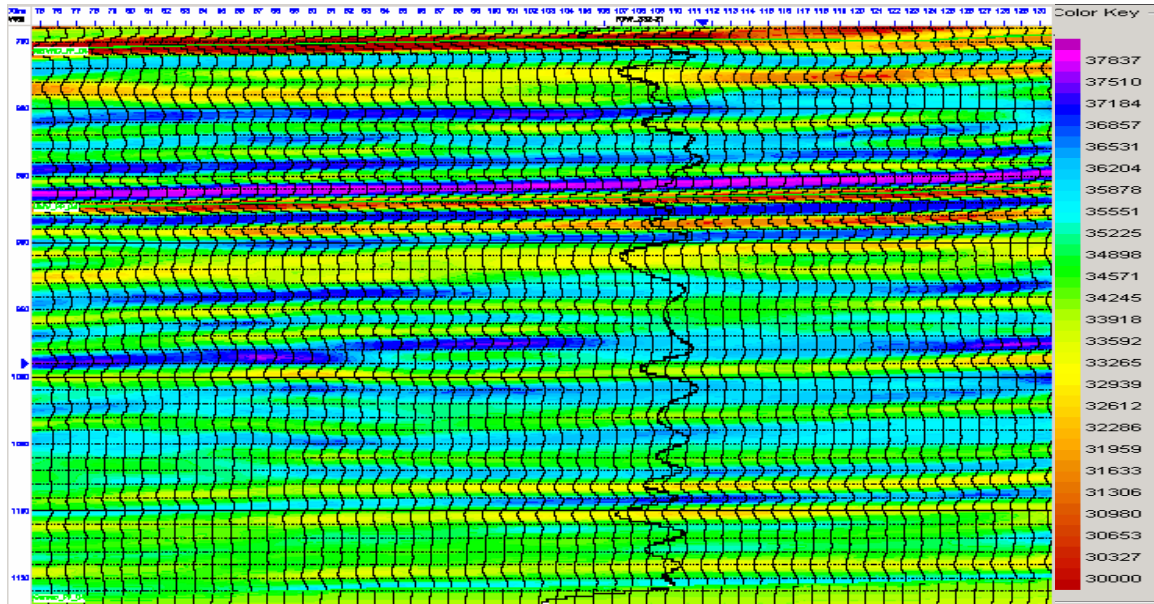


Figure 3.9 P-wave impedance result after applying model based inversion algorithm to the seismic data. Inserted curve is high frequency cut P-impedance calculated from the well logs.

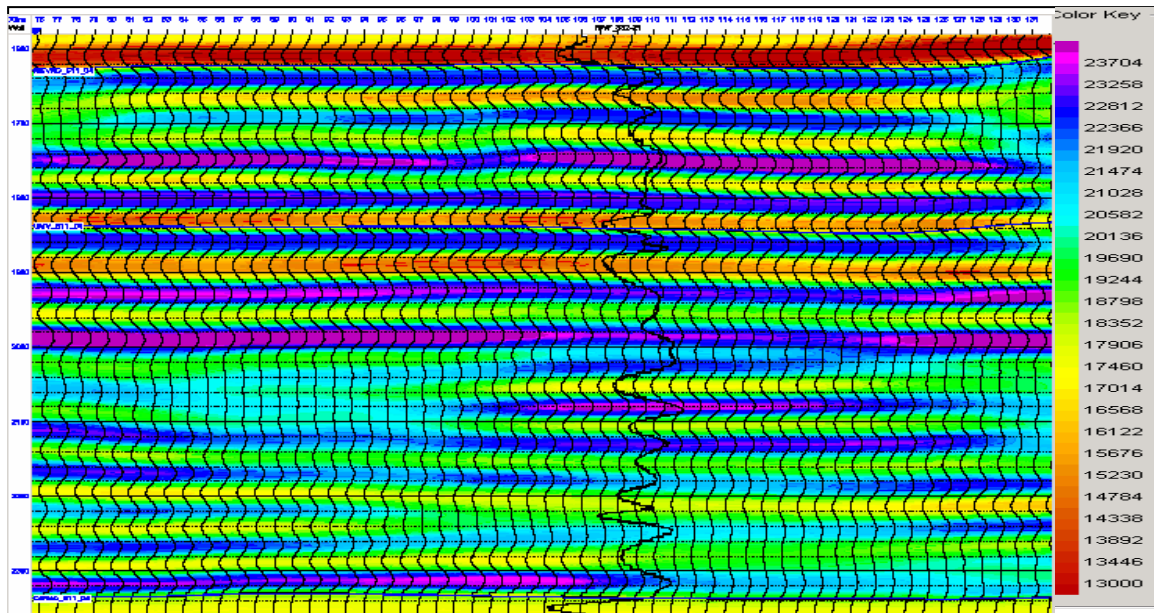


Figure 3.10 S-wave impedance result after applying model based inversion algorithm to the seismic data. Inserted curve is high frequency cut S-impedance calculated from the well logs.



### **3.6 Converted Wave Data Inversion Trough Pseudo S-Impedance Estimation**

To simplify the task of S-impedance estimation from poststack PS data, I assume that the medium is isotropic. This assumption is reasonable because the anisotropy parameters estimated by Franco (2006) within the reservoir at Rulison field indicate the presence of a weakly anisotropic environment.

Stacked PS amplitudes are not directly related to P- or S-impedance. In this section, I introduce the quantity proportional to PS reflectivity, pseudo shear  $\hat{S}$ -impedance. To retrieve this information from the stacked PS amplitudes, I apply model based inversion, following the procedures demonstrated and explained earlier in the chapter. The algorithm requires an input low frequency impedance model, which is usually generated from velocity and density logs. However, PS velocity needed for model creation cannot be registered by a sonic tool. Valenciano and Michelena (2000) express the reason for not using poststack PS data to estimate changes in medium properties, stating that “we have not been able to find a model for PS stacked data that has the simplicity of the convolutional model we assume to model PP stacked data”. The initial model has no contribution to the inversion results within the seismic bandwidth. Nevertheless, adding low frequency to the resultant impedance, the model also applies some constraints for the inversion algorithm. To be able to minimize these constraints and verify results a model must be applicable in the time domain of the input seismic and reflect vertical impedance variations that can be updated by matching the seismic amplitudes.

The idea of poststack converted wave data inversion based on convolutional a model for S-impedance volume was proposed by Valenciano and Michelena (2000). Instead of estimating PS velocity, they suggest to recalculate density values so that the product of estimated pseudo density  $\hat{\rho}$  and shear wave velocity is pseudo  $\hat{S}$ -impedance. To determine the pseudo density  $\hat{\rho}$ , the following equation can be utilized:

$$\hat{\rho} = \rho \left( \frac{1}{4} \frac{V_P}{V_S} + \frac{1}{2} \right), \quad (3.3)$$

where

$\hat{\rho}$  - pseudo density,

$\rho$  - original density,

$V_P$  – P-wave velocity,

$V_S$  – S-wave velocity.

Complete derivation of equation 3.3 is presented in Appendix A.

The purpose of this application in the presented work is to create an impedance model. Using as an input, registered in the well, density log and dipole sonic log velocities, I calculate pseudo density through equation 3.3. Figure 3.11 demonstrates the difference between real (red curve) and newly obtained pseudo (blue curve) density logs. The pseudo density log reveals similar magnitude but lowered absolute numbers than the real log. This also can be observed on the crossplot, where the regression line has a gradient of 1.0, and histogram of the density values (Figure 3.12). Analyzing these results, it is possible to estimate the corrections needed for the product of inversion -  $\hat{S}$  - impedance to turn the values to the actual S-impedance.

To build the model, the log data, S-wave velocity and pseudo density  $\hat{\rho}$ , must be multiplied and extrapolated. A section of the estimated impedance model is shown in Figure 3.13. The inversion algorithm produces a pseudo  $\hat{S}$ -impedance volume. The output results are inverted PS seismic amplitudes and added from the impedance model low frequency component.

Tying the inversion results back to the well, I estimate the correlation coefficient within the interval of interest to be about 0.73 (Figure 3.15). Figure 3.15 compares in

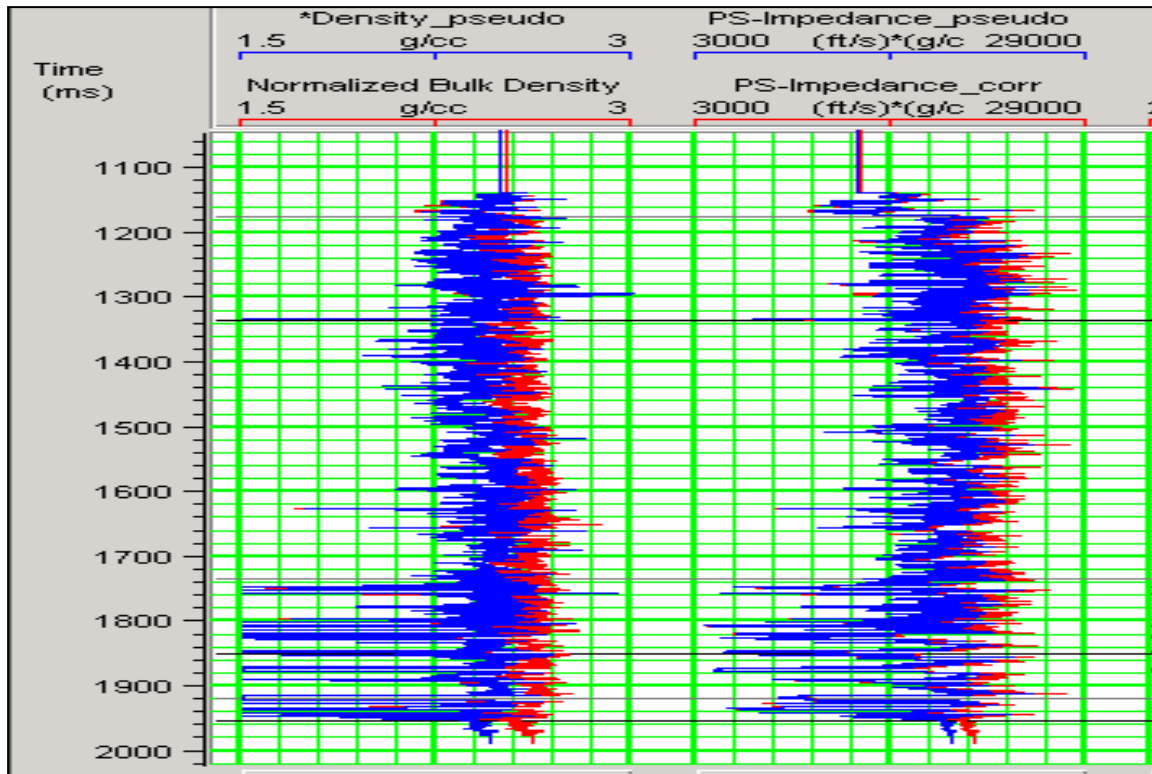


Figure 3.11 Calculated pseudo density log. The blue curve representing pseudo density has lower values than those of the red curve, tool registered and normalized bulk density. The pseudo impedance results, as a product of pseudo density and S-wave velocity have lower values than normal impedance as well.

PS time domain the S-impedance section (inversion estimation from pure shear wave data) and pseudo  $\hat{S}$ -impedance section (inversion estimation from converted wave data). The time rescaling of SS data is possible after a depth-to time curve has been estimated both for SS and PS time domains. The image on the right illustrates lower amplitudes, which could be expected from low values of the estimated pseudo density.

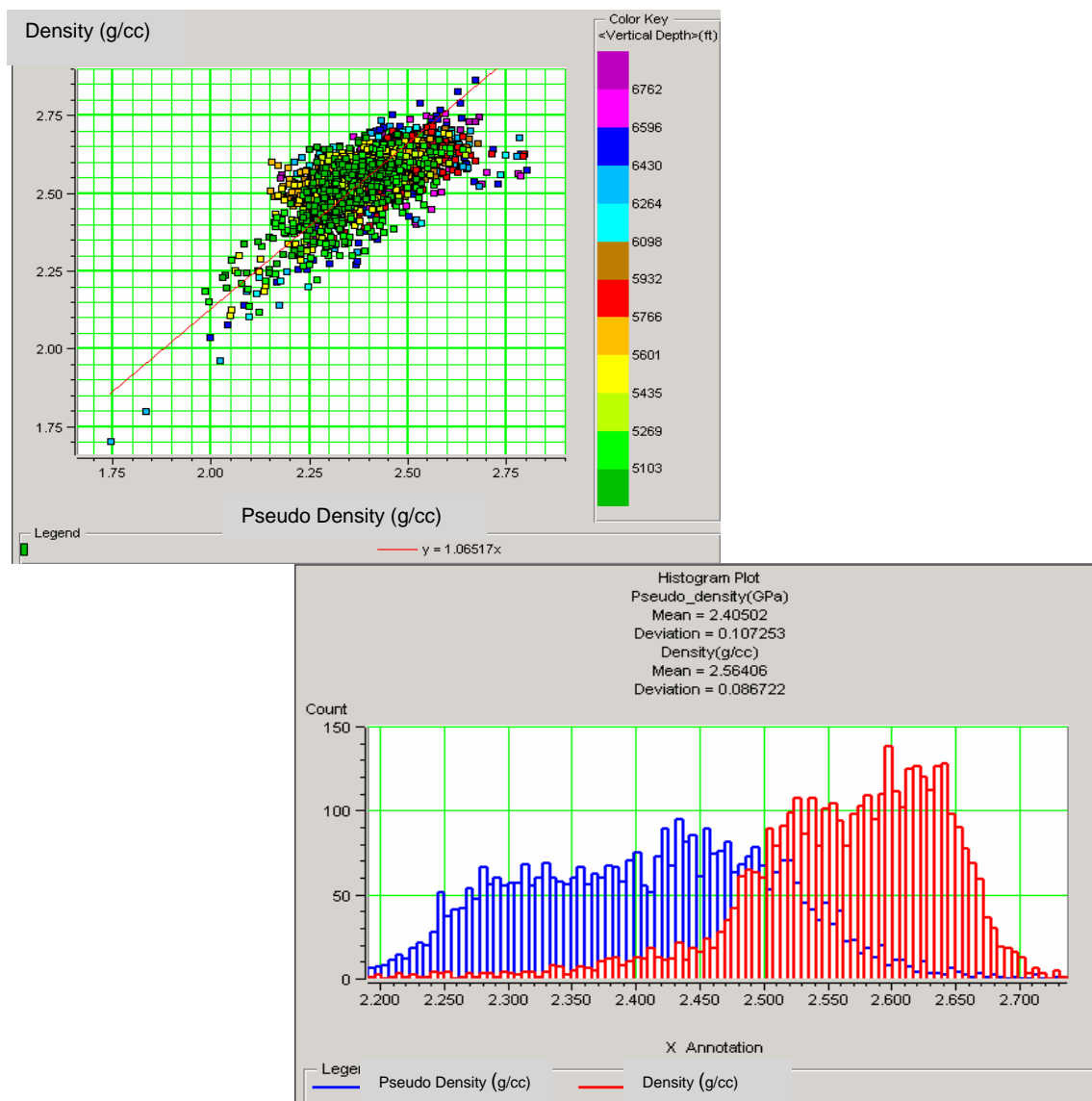


Figure 3.12 The crossplot and histogram of pseudo and normal density logs.

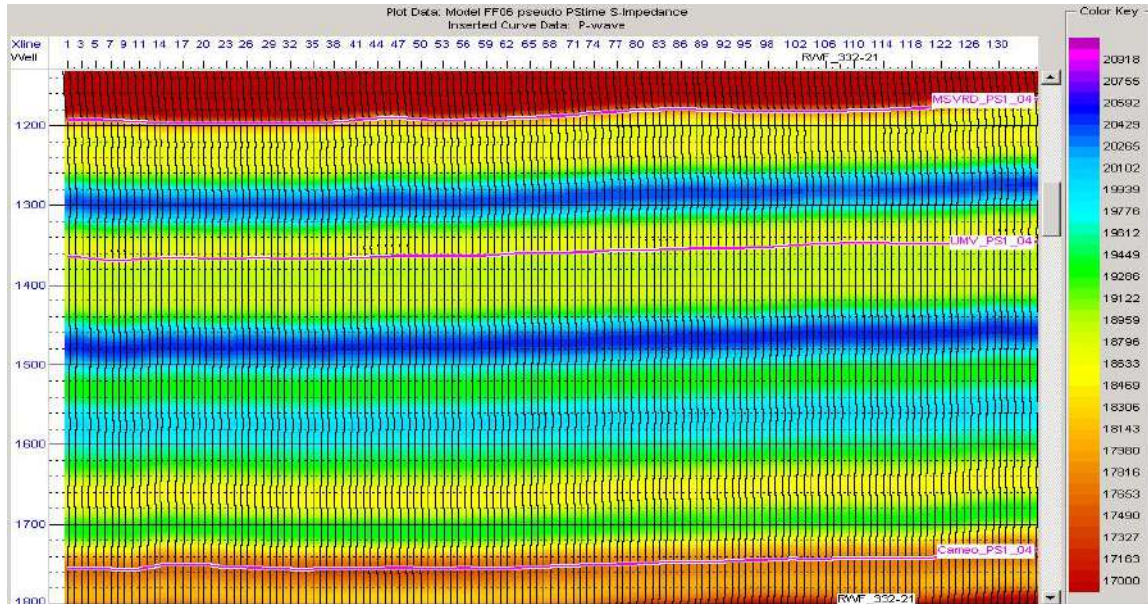


Figure 3.13 Pseudo  $\hat{S}$ -impedance model estimated from pseudo density  $\hat{\rho}$  and S-wave velocity log data.

### **3.6.1 Corrections For Pseudo S-Impedance From Differential Modeling**

The impedance results estimated from log data provide the method for pseudo  $\hat{S}$ -impedance volume calibration. The product of density and shear wave velocity logs reveal S-impedance, while multiplication of pseudo density and shear wave velocity logs results in  $\hat{S}$ -impedance (see Figure 3.11). Differential modeling here is determined as an extrapolation of the time variant difference between these two impedance values. Filtered to the seismic frequency range modeled difference I add to pseudo  $\hat{S}$ -impedance volume generated from the PS-wave data inversion. The output is a corrected pseudo  $\hat{S}$ -impedance, which demonstrates a good correspondence with the S-impedance derived from SS-wave data (Figure 3.16).

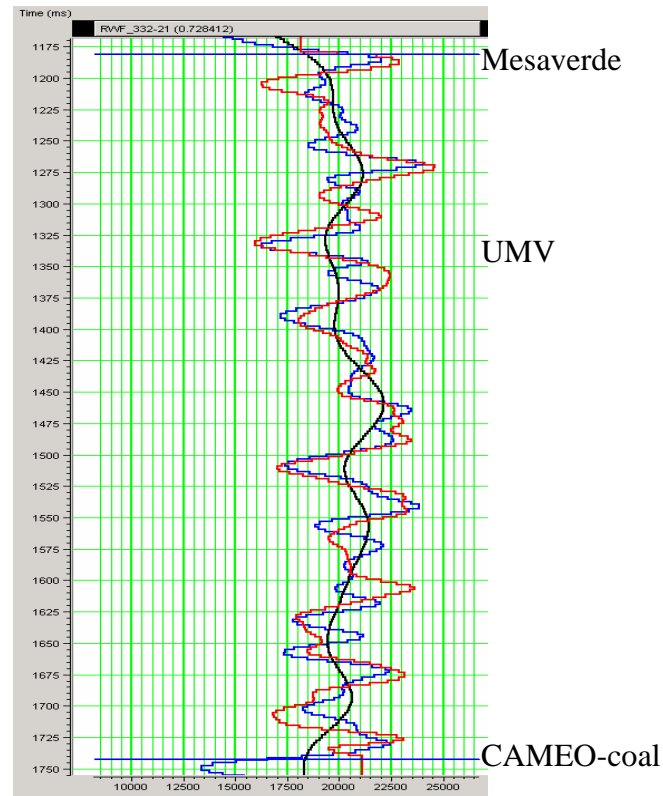


Figure 3.14 Inversion analysis of PS data, where pseudo S-impedance is modeled through the pseudo density estimation. Correlation coefficient, estimated within Mesaverde – Cameo interval is about 0.73.

I conduct some quantitative analysis two resultant shear impedance volumes. The S-impedance amplitudes from SS- and PS-wave data within the interval of interest are plotted against each other in Figure 3.17. The derived equation for the least square regression line is  $Y=1.42X-9328$ . Figures 3.18a and 3.18b display the histogram plots for S-impedance estimations from SS- and PS-wave data respectively. Normal distribution curve has similar shape for both data sets amplitudes. Mean and deviation calculations show close numbers Figure 3.18c is both histograms plotted within the same coordinate system. This explicitly demonstrates the similarity between S-impedance results.

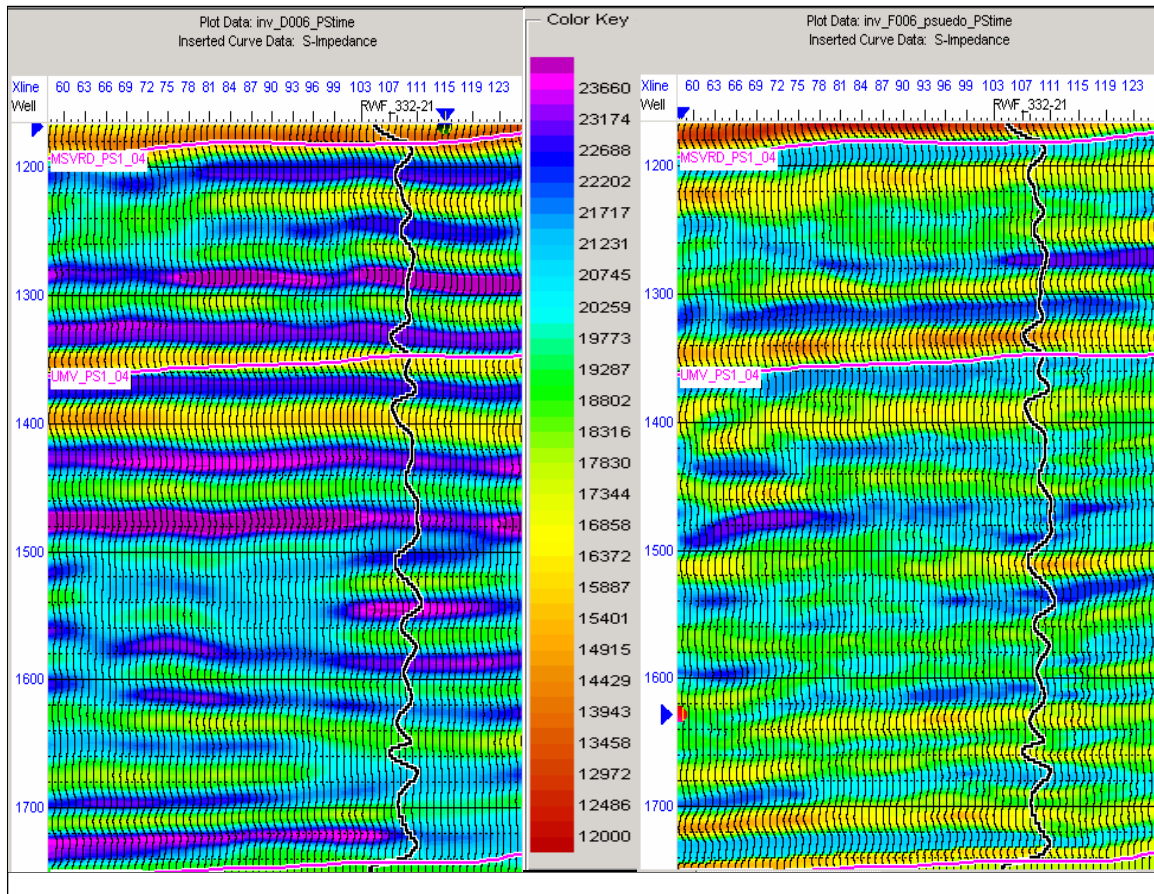


Figure 3.15 Comparison of S-impedance (left) generated from SS amplitudes and pseudo S-impedance (right) generated from PS amplitudes. The amplitudes are lower on the right image, which could be expected from lower pseudo density values.

The further test for modeled S-impedance is a plot of original shear impedance log and a composite trace from the corrected result. This QC result is displayed in Figure 3.19, where the left image shows the inversion result, shifted from the initial position, before, and right image after the corrections have been applied. The curve on the right image is within the appropriate framework.



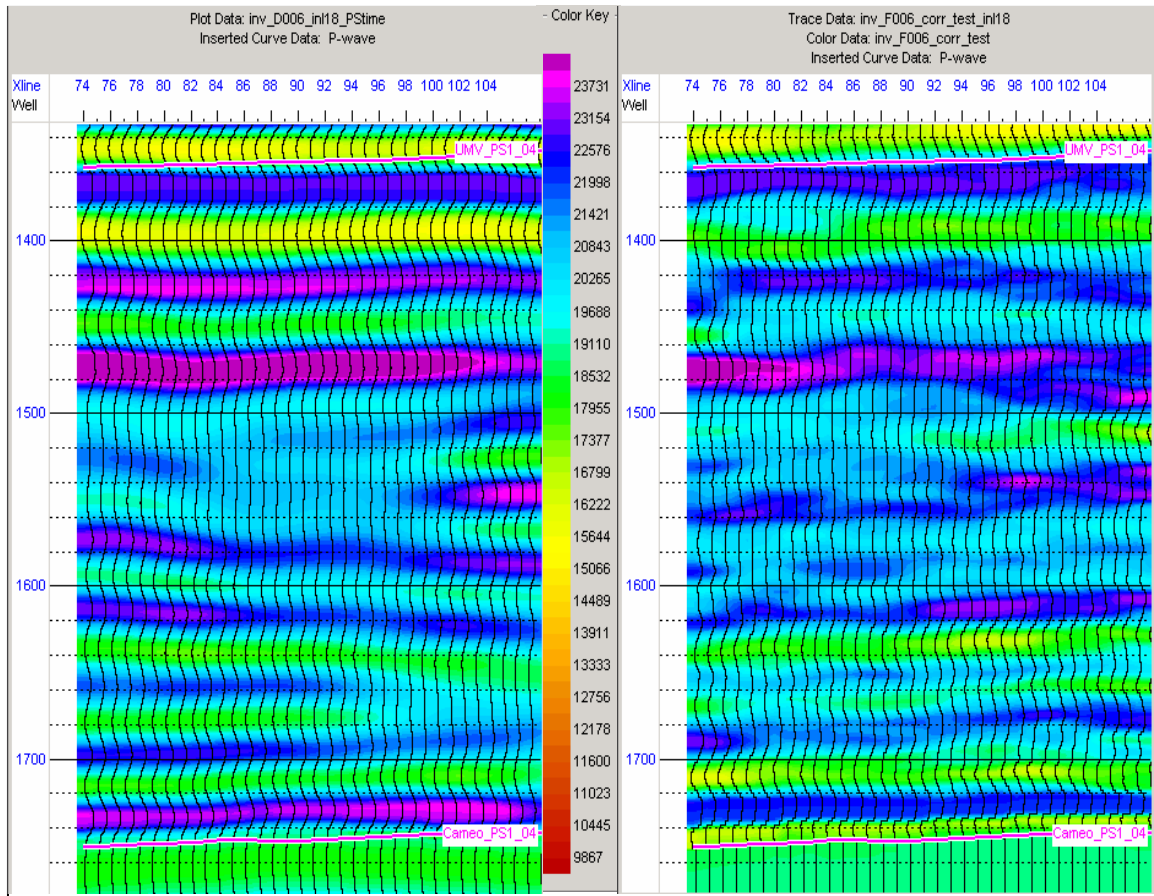


Figure 3.16 Comparison of attributive S-impedance (left) and corrected pseudo S-impedance (right) after differential modeling corrections are applied.



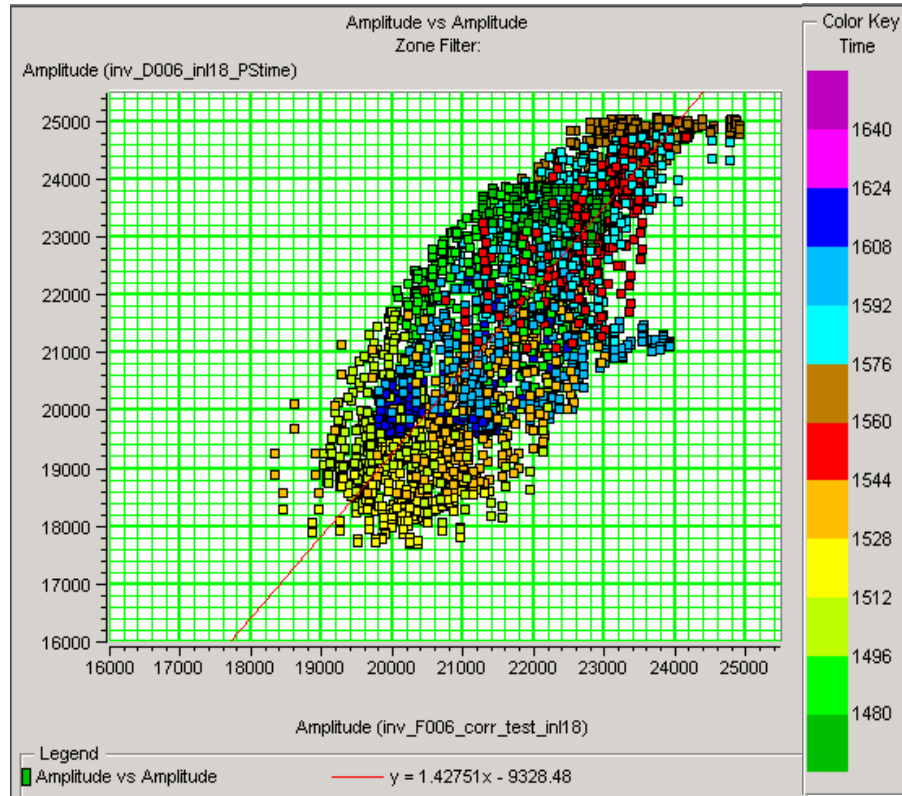
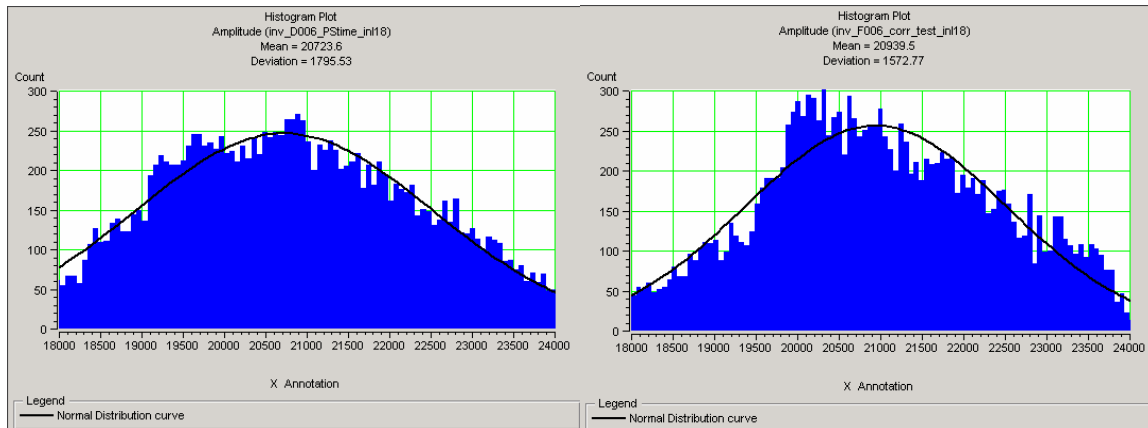


Figure 3.17 The crossplot of impedance values after the differential modeling corrections have been applied. The X axis is represented by S-impedance amplitudes from PS-wave data, the Y axis is represented by S-impedance amplitudes from SS-wave data. The slope of the regression line is  $Y=1.42X-9328$ .

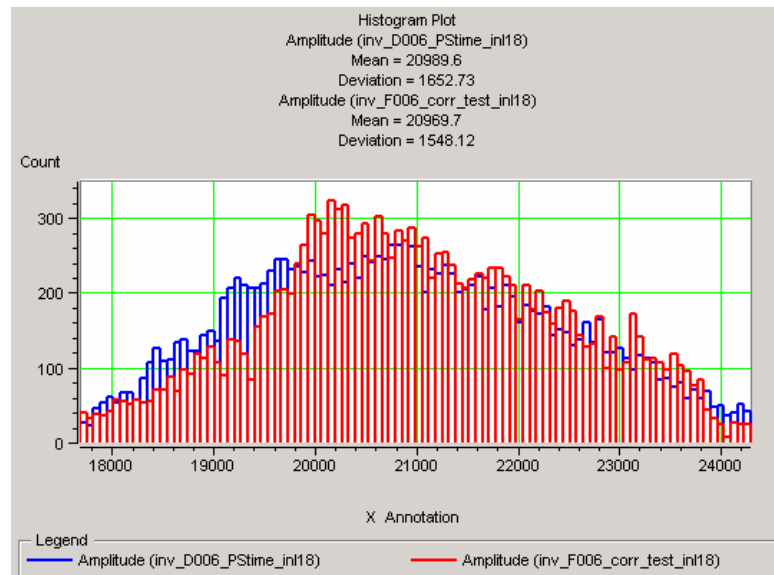
### **3.7 Summary**

Model based is an inversion algorithm I apply to the seismic data to convert seismic amplitudes into the impedance values. The procedure has broad application for pure mode seismic data but generally has not been applied to mode converted wave P-S data. To compute shear impedance volume from PS data, I introduce the quantity – pseudo density  $\hat{\rho}$ . The product of the log derived pseudo density and shear velocity is pseudo  $\hat{S}$ -impedance, the parameter proportional to the converted PS-wave reflectivity



a)

b)



c)

Figure 3.18 The histograms of S-impedance amplitudes. a) S-impedance generated from SS-wave data. The mean value is 20724 and deviation number is 1796. b) S-impedance generated from PS-wave data. The mean value 209405 and deviation number 1673 are very close to the ones above. c) Both SS-wave (blue curve) and PS-wave (red curve) generated impedance data.

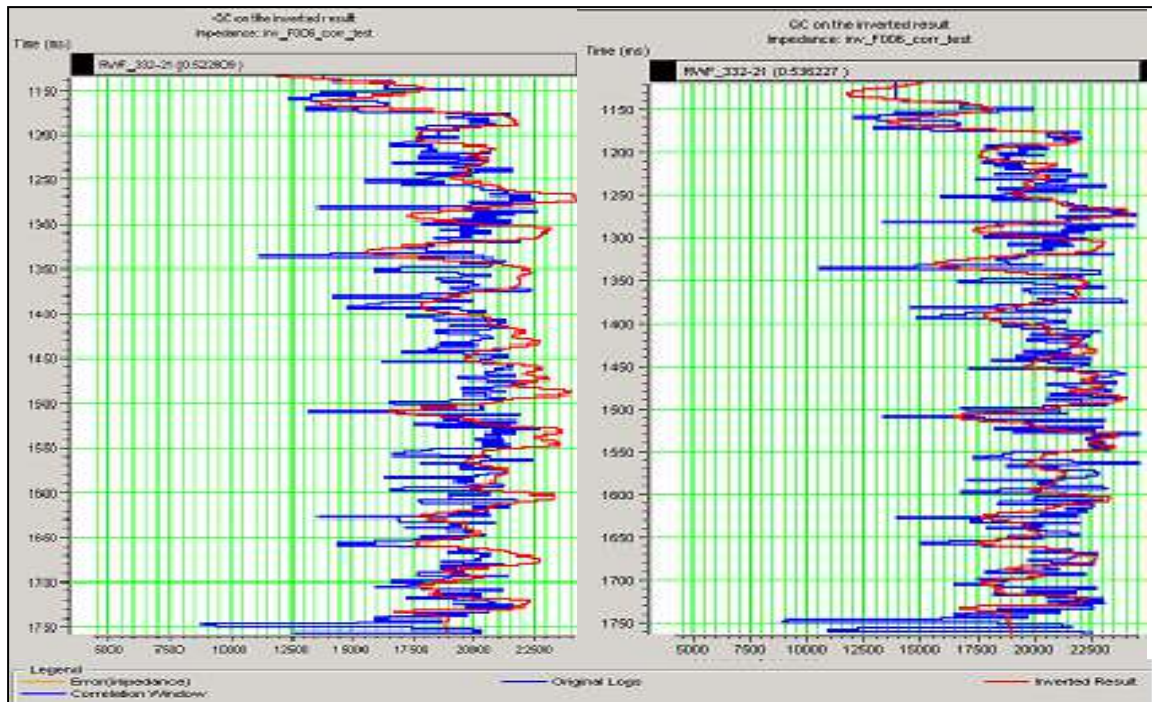


Figure 3.19 QC of the corrected pseudo impedance volume. Left screen shows the correlation between original shear impedance log (blue curve) and synthetically generated impedance volume (red curve). The right screen displays the noticeable improvement in correlation that is obtained after the applied corrections.

data. Extrapolation of the computed pseudo  $\hat{S}$ -impedance creates an impedance model, which serves as an input for the model-based inversion algorithm. With this approach, I invert PS-wave seismic amplitudes for the  $\hat{S}$ -impedance values. The estimated corrections then, calibrate the pseudo values for the actual S-impedance results.

## **CHAPTER 4**

### **METHODOLOGY FOR Vp/Vs ESTIMATION FROM IMPEDANCE INVERTED DATA**

#### **4.1 Chapter Introduction**

I show in this chapter the method to estimate Vp/Vs, which is defined as high resolution Vp/Vs. The input data include P-impedance and two S-impedance volumes generated in the previous chapter. I obtain and analyze for robustness two high resolution Vp/Vs volumes. The computation is followed by the correlation tests of the resultant velocity ratio volumes and well log data.

#### **4.2 High Resolution Vp/Vs Volume**

This chapter concentrates on the work that is done on multicomponent seismic data at Rulison field in an attempt to generate a “high” resolution Vp/Vs volume. High resolution Vp/Vs is an appropriate term if the properties are sensitive to temporal and spatial changes. According to Rojas (2005) we should delineate low Vp/Vs zones as potential gas charged intervals and target them for future drilling in the area of study. The nature of the reservoir demands high resolution Vp/Vs measurements in order to properly target them.

##### **4.2.1 Seismic Inversion As A Tool For High Resolution Vp/Vs Estimation**

P-impedance and S-impedance are presented by equations (4.1) and (4.2) respectively.

$$Z_P = \rho V_P, \quad (4.1)$$

$$Z_s = \rho V_s, \quad (4.2)$$

where:

$Z_p$  – P-wave impedance,

$Z_s$  – S-wave impedance,

$V_p$  – P-wave velocity,

$V_s$  – S-wave velocity,

$\rho$  – density.

The ratio of impedance volumes at particular depths intervals will result in the ratio of velocities and the influence of density will be eliminated:

$$V_p/V_s = Z_p/Z_s. \quad (4.3)$$

To verify the results they must be compared with well logs and must be calibrated to increase the reliability and interpretability. The impedance volumes generated and tested for quality control from compressional PP, pure shear S11 and converted shear PS1 seismic data create two data sets for  $V_p/V_s$  estimation – PP-S11 and PP-PS1. Presented herein are the results of two  $V_p/V_s$  volumes calculation, their description and correlation with log derived  $V_p/V_s$ .

### **4.3 $V_p/V_s$ Volume Calculation**

The math, involved in this process, requires both P- and S-impedance volumes to have equal vertical scale. It can be either depth or any of the three time domains, PP, SS or PS. I process the amplitude inversion of the seismic traces in their original time domains. To convert the resultant impedance volumes to depth, at least two velocity volumes are required, P-wave and S-wave velocity, which can be calculated along with the impedance inversion estimation from the Gardner's equation (for more details see depth conversion in Chapter 5). However, the reason for not using depth as a common

scale is inaccuracy of these velocity volumes and, consequently, mispositioning of the time seismic events in the depth domain. Hence, I estimate high resolution Vp/Vs in the time domain. To switch between different time domains, the only information needed is depth-to-time curve, generated from the multicomponent seismic well tie.

I conclude that time domain transformation before the inversion does not produce as robust results as if the transformation is performed on impedance inverted volumes. This can be explained by the fact that resampling of the seismic traces requires the extraction of a new wavelet. Since the rescaling of the time axes does not contain any information and preserves the actual amplitudes, the inversion algorithm, based on the trace convolutional model, encounters the problem of an inaccurate wavelet.

High resolution Vp/Vs is the velocity ratio that can be defined at every time sample. At the point when the seismic amplitudes are recalculated for the impedance, the simple ratio of the obtained volumes (described by equation 4.3) will reveal more detailed results of Vp/Vs. Figure 4.1 compares a part of seismic section colored with Vp/Vs values interpolated from the well log data (Figure 4.1a) and Vp/Vs estimated from the ratio of P-impedance volume and S-impedance volume estimated from pure shear wave data and converted to PP time volume (Figure 4.1b). The right figure reveals a more detailed Vp/Vs image and better correspondence with the original, before inversion seismic wiggle traces, confirming the contribution of the actual time reflection data to the estimation of Vp/Vs.

The quality and resolution of the newly obtained Vp/Vs is limited to the quality and resolution of the input seismic data. The vertical resolution is proportional to the seismic wavelength, which can be estimated by the ratio of velocity and frequency. The amplitude spectrum computed in the middle of the reservoir reveals the dominant frequency at about 35 Hz for P-wave and about 20 Hz for S-wave. The velocities within this interval I approximate from the P- and S-impedance results (to generate the velocity volumes, I use the relationship between velocity and density estimated through the Gardner's equation), 13,610 ft/s and 8900 ft/s respectively. Thus, the wavelength of



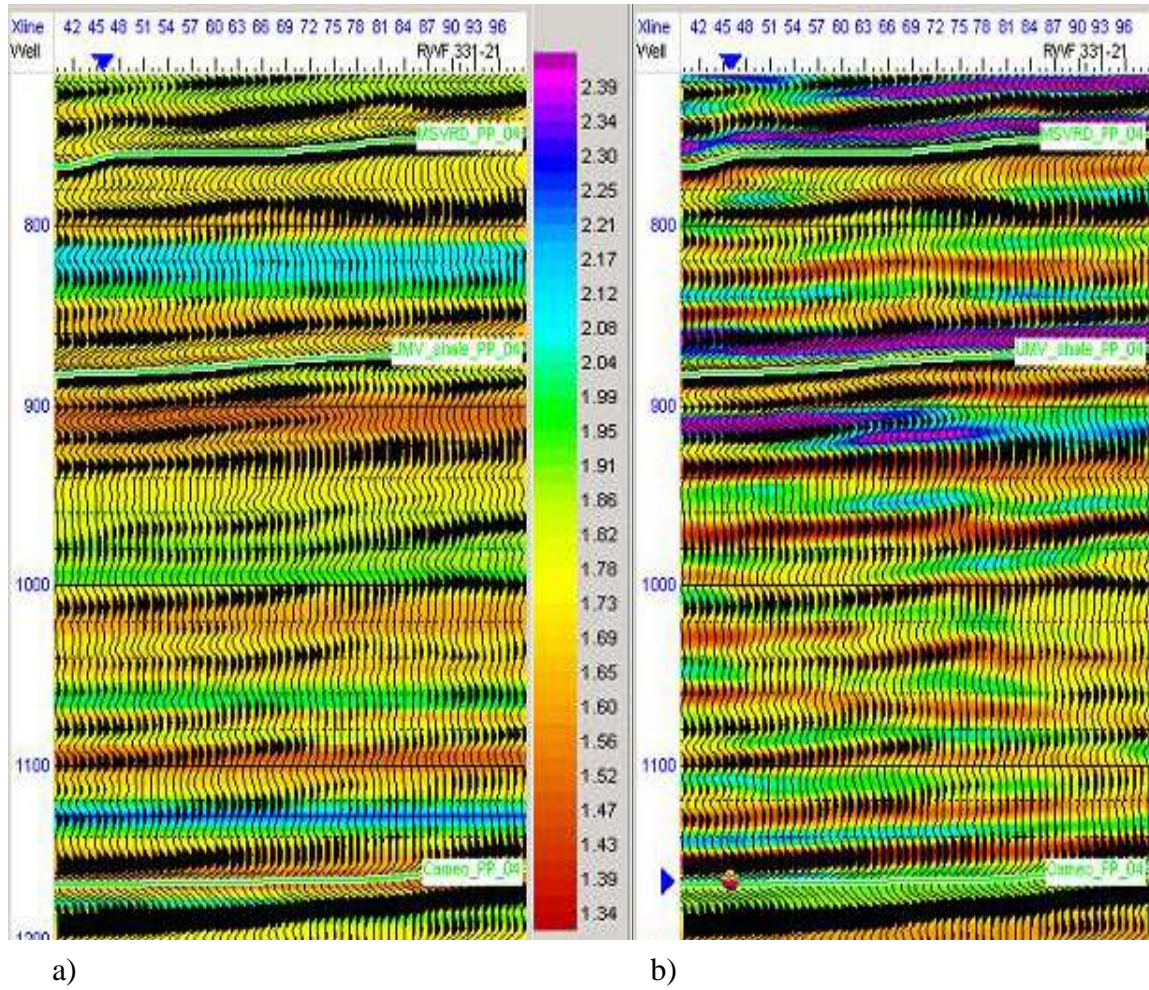


Figure 4.1 Seismic wiggle traces color coded with: a) Spatially interpolated log  $V_p/V_s$  data; b) high resolution  $V_p/V_s$  estimated from PP and S11 wave seismic data.

compressional wave data estimated in PP time is 390 ft, while the wavelength of fast shear wave data estimated in SS time is 445 ft. The common estimate of vertical resolution is a quarter of the dominant wavelength. Therefore, the vertical resolution of the impedance inverted and calculated Vp/Vs volume is approximately as low as one fourth of the seismic wavelength or 100 ft.

Spatial resolution is very often associated with the Fresnel zone, the area that returns half of the energy from the reflector. I perform no procedure to increase lateral resolution of the resultant Vp/Vs. Therefore, the radius of the Fresnel zone can be calculated in terms of dominant frequency

$$r = \frac{v}{2} \sqrt{\frac{t}{f}}, \quad (4.4)$$

where:

$r$  - Fresnel zone width,

$v$  - velocity at various depth,

$t$  - vertical time,

$f$  - dominant frequency.

Assuming the same parameters as for vertical resolution estimation, the numbers I calculate for spatial resolution or first Fresnel zone radii are about 575 ft for P-wave data and 600 ft for S-wave data, which are close to the wavelengths estimations. It can be explained by the fact that migration of seismic data tends to collapse diffractions and decrease the size of the Fresnel zone. Hence the fully migrated input seismic data have an improved lateral resolution, which is commensurable to the wavelength. Frequency is inversely proportional to wavelength, so an increase in dominant frequency will result in resolution enhancement. The dominant frequency of a stacked section from a given area is governed by the physical properties of the subsurface, processing quality and recording



parameters (Yilmaz 2001). The last two can enhance the high-frequency level of the signal and produce high-quality seismic data.

Vp/Vs estimations reveal similar results. Shown in Figure 4.2 is a comparison between Vp/Vs results estimated from PP-S11 and PP-PS1. The sections are shown in PP time. The zones of abnormally low Vp/Vs (below 1.5) are colored in red. Upon closer examination of seismic Vp/Vs represented by black curves and log Vp/Vs, red curve, I infer that the shapes of two resultant velocity ratio curves (not the actual amplitudes) match each other with the exception of some zones (Figure 4.3). Notice that the lower portion of the reservoir contains some misfit between two signals in Figure 4.3a, as it is predicted by inversion analysis (see Figure 3.6 in Chapter 3). In Figure 4.3b the Vp/Vs traces from PP-PS1 combination match the log Vp/Vs even in the lower part of the reservoir, close to Cameo level.

I estimate the correlation coefficient between seismic and log signals within two intervals, between UMV and Cameo, and in the middle of the reservoir section. Figure 4.4 images PP-S11 derived Vp/Vs trace at well RWF 332-21 location (red curve) and log derived Vp/Vs (blue curve). The correlation coefficient estimated for the UMV - Cameo interval is about 0.50. The misfits in the upper (close to UMV) and lower (close to Cameo) portions of the reservoir, as observed in Figure 4.3a, reduce the correlation between two signals. In the middle portion of the reservoir, the correlation coefficient is about 0.77. Therefore, more reliable results can be expected within this interval.

Figure 4.5 reveals the correlation coefficient for Vp/Vs derived from PP-PS1 data set. The interval covering vertical section between UMV and Cameo is well correlated with log derived Vp/Vs. The coefficient is about 0.70. The correlation coefficient for the middle portion is about the same, 0.67.

The major Vp/Vs computational errors are controlled by the inversion technique and the depth-to-time curve applied. The first contributes to the impedance values estimation, the second adjusts vertically rescaled traces in different time domain.

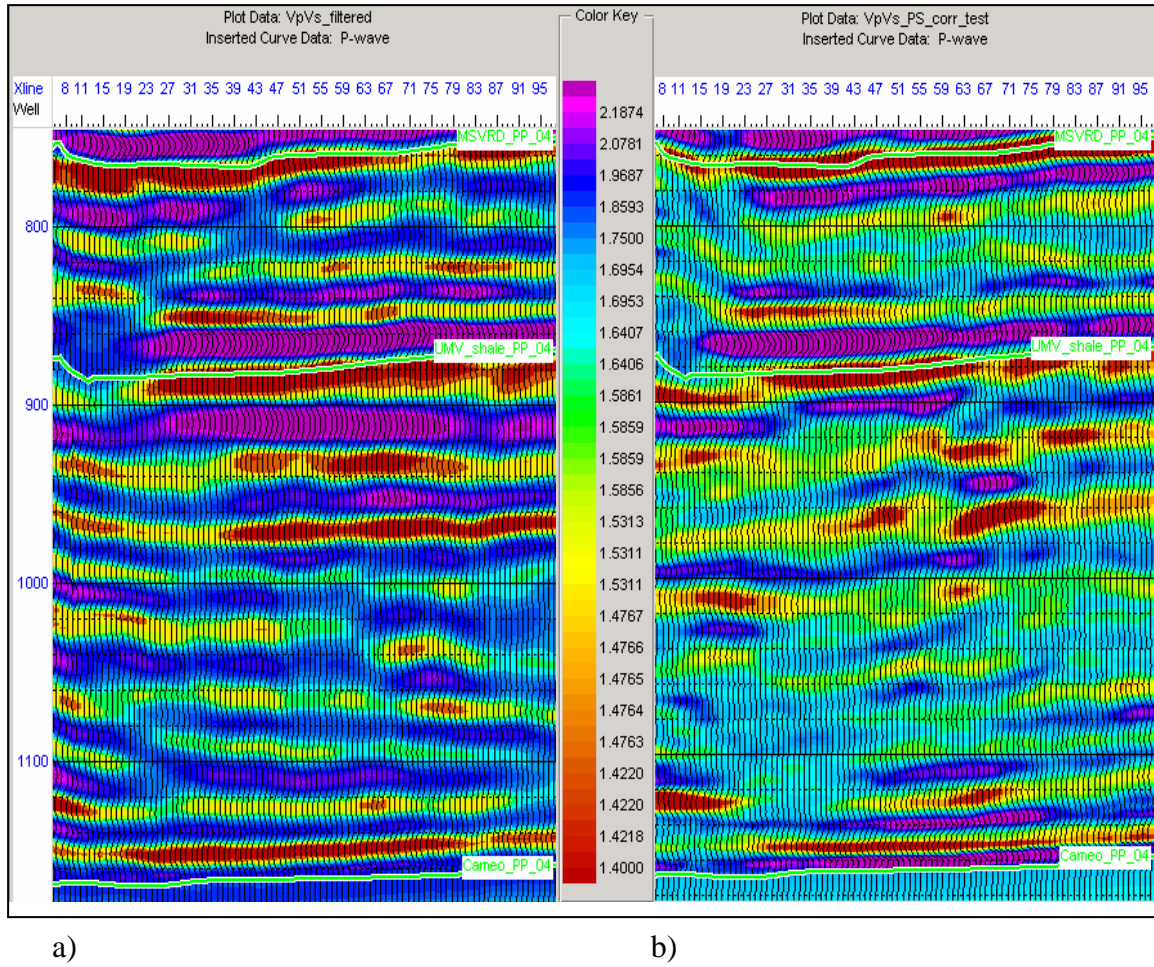


Figure 4.2 Vp/Vs inline 18. Sections are estimated from: a) PP-S11 data set, b) PP-PS1 data set. The shown interval is in between top of Mesaverde and top of Cameo.

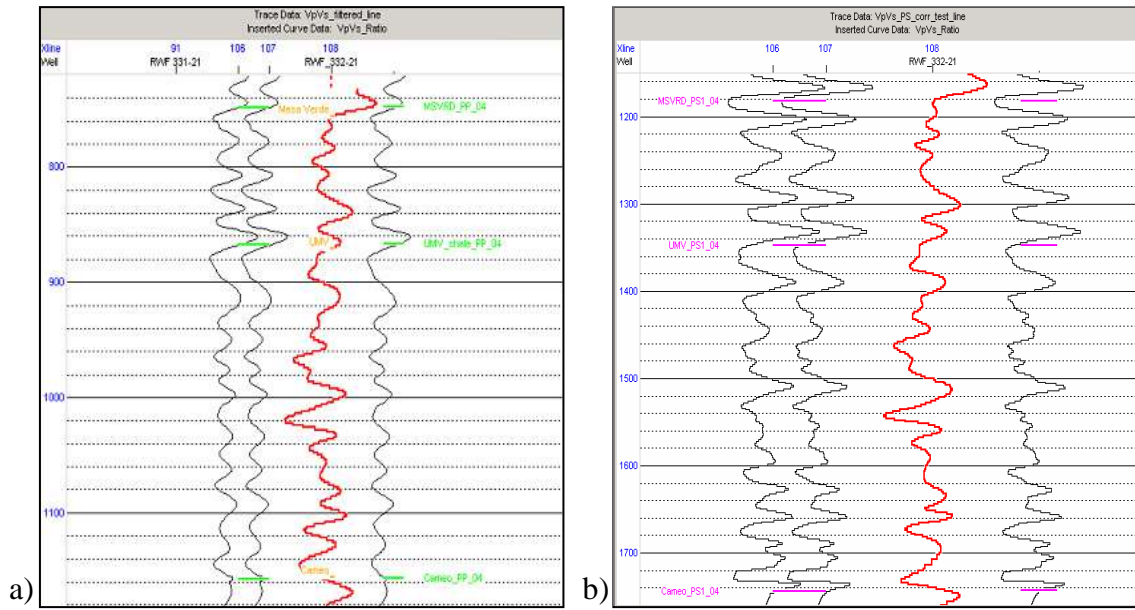


Figure 4.3 Comparison of Vp/Vs traces (black curves) and Vp/Vs log (red curve). The data shown are obtained from: a) PP-S11 data set in PP time; b) PP-PS1 data set in PS time.

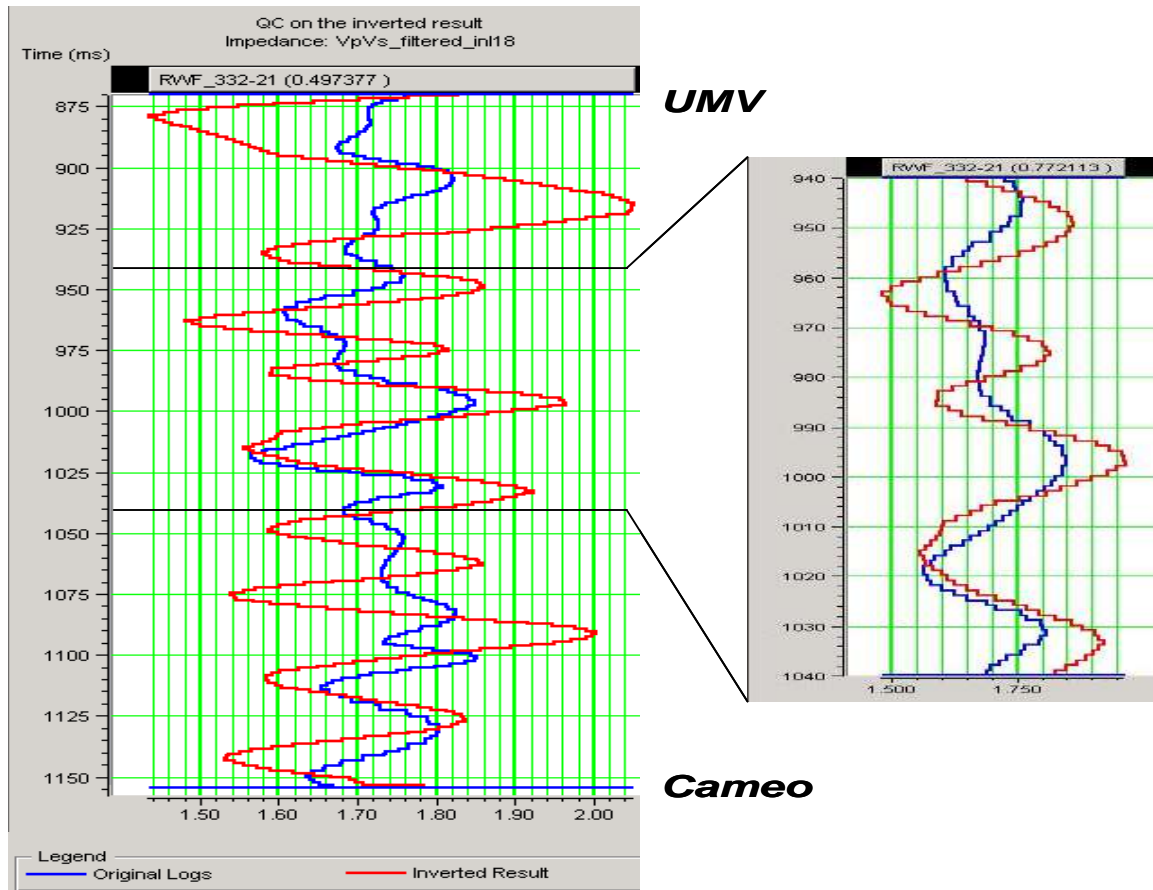


Figure 4.4 Correlation of Vp/Vs estimated from PP-S11 data set (red curve) at well RWF 332-21 location and log derived Vp/Vs. Estimated correlation coefficient for UMV-Cameo interval is about 0.5, for the middle reservoir 0.77.

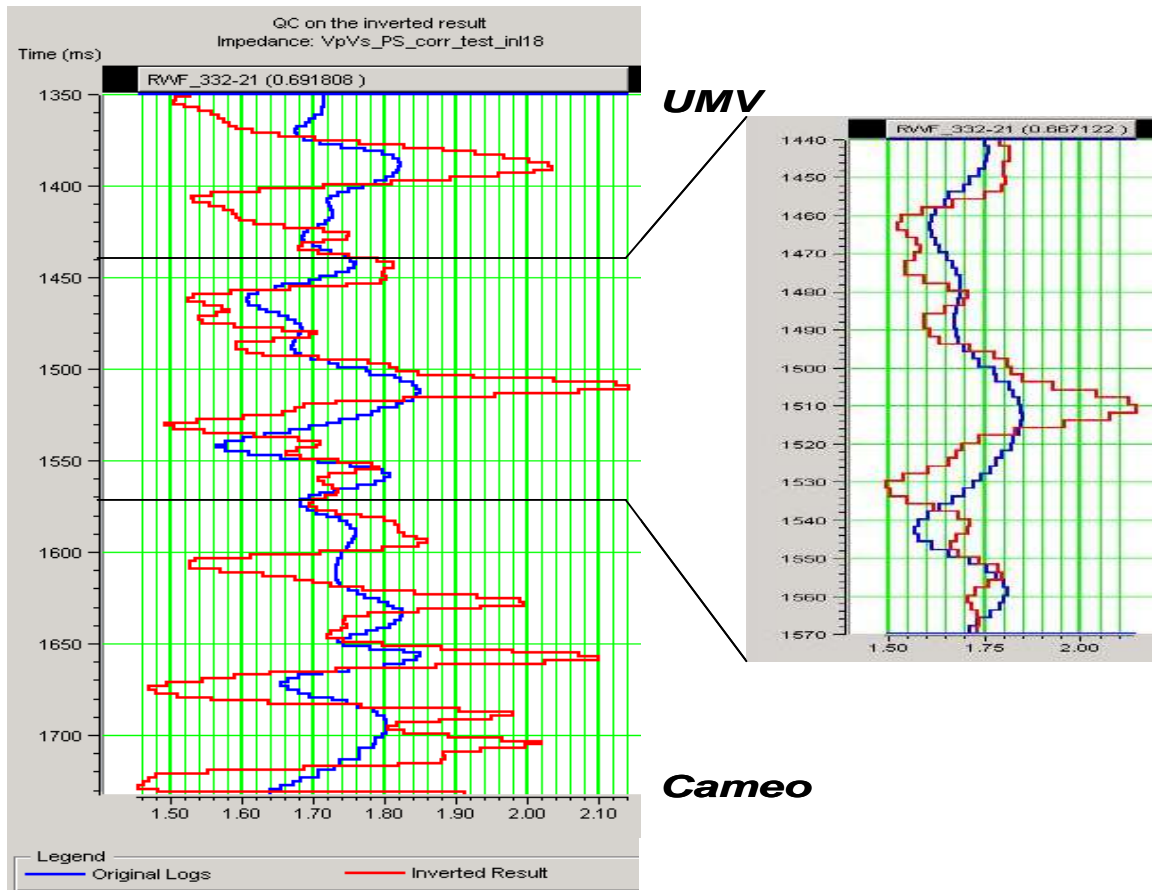


Figure 4.5 Correlation of Vp/Vs estimated from PP-PS1 data set (red curve) at well RWF 33-21 location and log derived Vp/Vs. Estimated correlation coefficient for UMV-Cameo interval is about 0.69, for the middle reservoir 0.67.

#### **4.4 Quality Test At A Distant Well**

Prior to this point, I have been analyzing all the errors at one well location, which is involved in the process of  $V_p/V_s$  calculation. To demonstrate the robustness of the results, seismic derived velocity ratio must be compared to some independent data, which are not involved in the process of  $V_p/V_s$  extraction. Such data appeared to be velocity information obtained from well RWF 441-20, which is about 4500 ft (1.5 km) away from the well RWF 332-21 (see Figure 1.11 in chapter 1). The dipole sonic log was run in this well in 2006 providing some additional material to support this study. Figure 4.6 demonstrates the near well  $V_p/V_s$  traces extracted from compressional and converted wave data shown in black and log derived  $V_p/V_s$  shown in red. A poor correlation can be observed in under UMV portion of the reservoir. The well log data do not exhibit much variation. As it is described in chapter 1, the upper part of the reservoir contains some water mixed with gas in the porous media. This may affect sonic shear wave velocity and disturb the image of velocity ratio. The deeper portion of the reservoir, from the level approximately corresponding to the top of gas to the top of Cameo, reveals much better correlation between two data sets.

I evaluate the correlation coefficient for UMV – Cameo interval and for the middle portion of the reservoir (Figure 4.7). In the first case the coefficient is 0.40, showing poor overall correlation. In the second, the coefficient reaches 0.62. Hence, the  $V_p/V_s$  velocity ratio validates more pronounced results in tight sandstones filled with gas (middle reservoir) rather than mixture of water and gas (upper portion of the reservoir). This conclusion is useful for the discrimination of pore fluids content in this particular and similar environment.

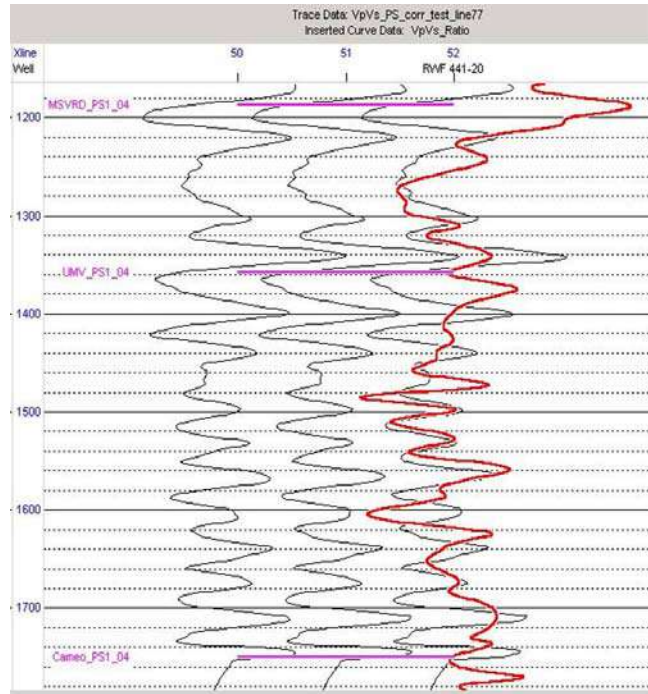


Figure 4.6 Comparison of Vp/Vs traces from PP-PS1 data set and Vp/Vs log from dipole sonic run in well RWF 441-20.

#### **4.5 High Resolution Vp/Vs Failure As A Time Rescaling Tool**

I want to concentrate some attention to the problem of time rescaling using high resolution Vp/Vs values. I include this discussion because the reader may consider amplitude derived velocity ratio equal to traveltime derived in terms of its applicability. I feel obligated to inform that the estimations of Vp/Vs values I present in this chapter are not suitable for time domain conversion of seismic data.

As explained in chapter 2, the method for traveltime recalculation into different time domain is based on depth-to-time curves extracted from well logs leading to horizons picking and interval Vp/Vs volume estimations. Thus, the calculated interval Vp/Vs has the property of a rescaling factor for the vertical time domain. Certainly, the

domain conversion can be performed only for a bulk volume of seismic data equal to a volume of applied interval  $V_p/V_s$ . Hence, the seismic volume is resampled to different domain.

Impedance derived  $V_p/V_s$  changes both laterally and vertically. This property brings more of the sample by sample recalculation of the time scale. False of one  $V_p/V_s$  value will cause summed traces horizontal distortion. This incorrect value will also propagate errors through the computation of new timing. If more than one  $V_p/V_s$  values are erroneous, which is more realistic, then the whole seismic image can become deformed after time domain conversion.

To prove my theory, I show the time domain rescaling of compressional wave data to SS time domain (Figure 4.8). Notice, that traces on the right image, where I apply impedance derived  $V_p/V_s$  for rescaling, are more distorted than those on the left image, where I use more convenient interval  $V_p/V_s$ . The mispositioning of the events is more obvious because the horizons on the right image do not overlay the seismic wiggle traces. In contrast, interval  $V_p/V_s$  on the left image places the originally interpreted P-wave traces in correct vertical SS time positions by stretching the bulk volume of the specified interval.

#### **4.6 Summary**

The ratio of P- and S- impedance volumes estimated from compressional PP, pure shear S11 and converted shear PS1 seismic data is used to create  $V_p/V_s$  volume, with the resolution controlled by the resolution of the input seismic data. Two separate data sets are PP-S11 and PP-PS1. Examination of the results of  $V_p/V_s$  for quality control shows a good correlation with well log data in the middle part of the reservoir.

The estimated high resolution  $V_p/V_s$  is not applicable for time domain conversion of seismic data.



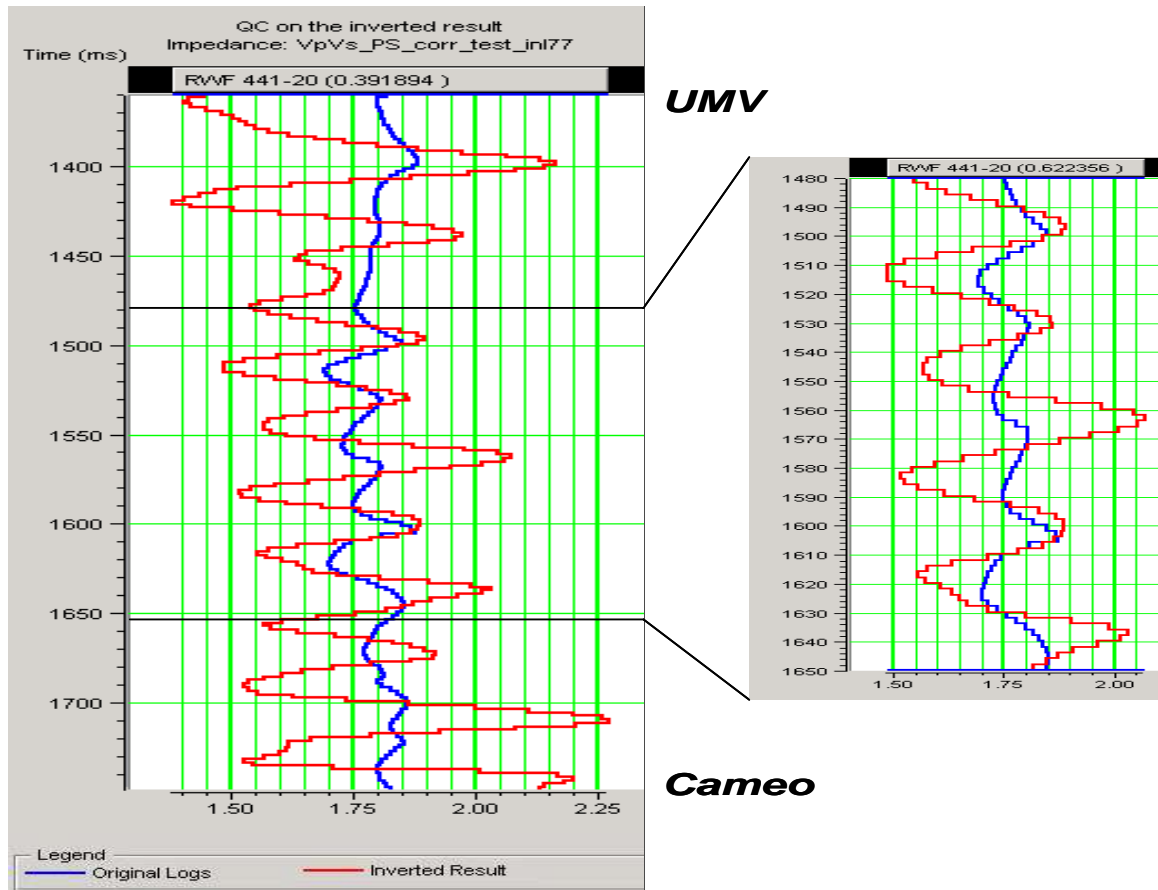


Figure 4.7 Correlation of Vp/Vs estimated from PP-PS1 data set (red curve) at well RWF 441-20 location and log derived Vp/Vs. Estimated correlation coefficient for UMV-Cameo interval is about 0.39, for the middle reservoir 0.62.

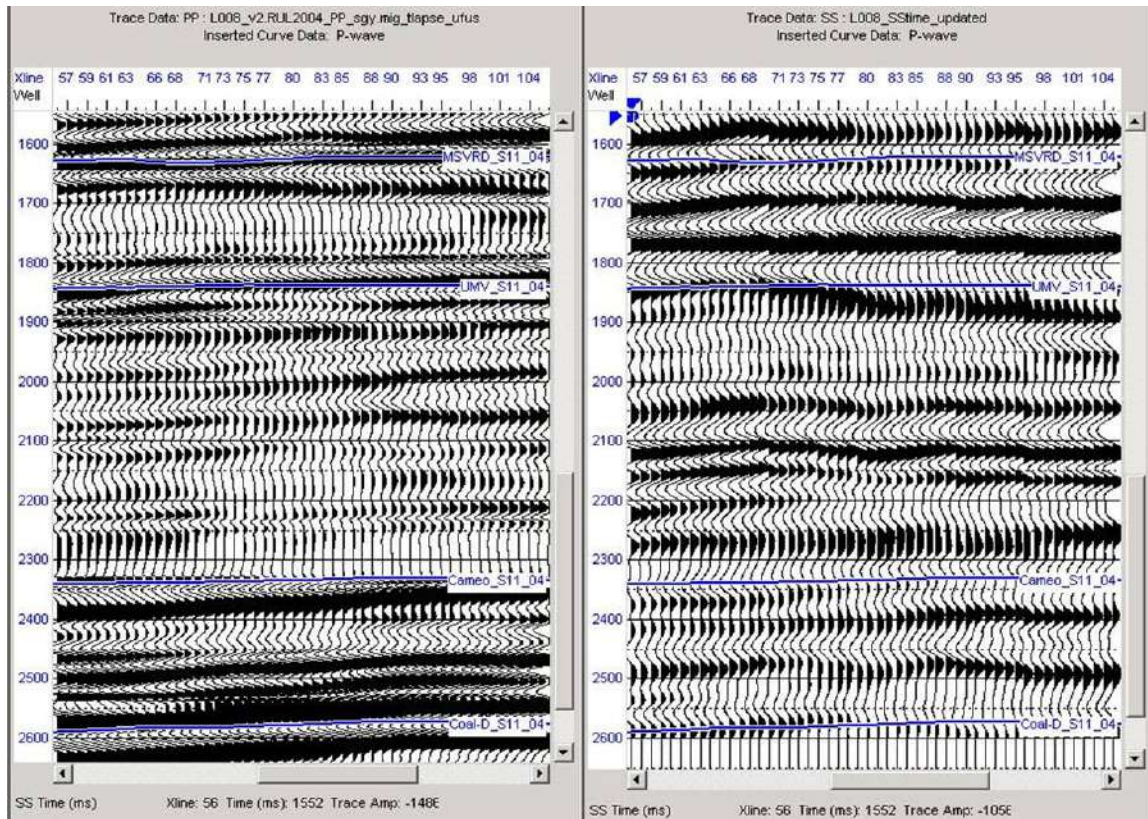


Figure 4.8 P-wave data transferred to SS time domain. The image on the left represents time section obtained after interval  $V_p/V_s$  application. The right image demonstrates the application of impedance derived  $V_p/V_s$  for rescaling of the original vertical axis. Erroneous disposition of the traces is obtained on the right image.

## **CHAPTER 5**

### **ANALYSIS AND INTERPRETATION OF Vp/Vs RESULTS**

#### **5.1 Chapter Introduction**

This chapter contains discussion and interpretation of the obtained Vp/Vs results. I investigate interval Vp/Vs by mapping the average values within the UMW - Cameo interval and comparing them with EUR and net sand thickness data. Three dimensional representation broadens the scope of the high resolution Vp/Vs. The stratigraphic interpretation of the high resolution Vp/Vs volumes and analysis of the Vp/Vs depth slices reveal zones of gas charged overpressured sandstone stacks.

#### **5.2 Interval Vp/Vs Interpretation**

Two maps of interval Vp/Vs results generated from PP-S11 and PP-PS1 data combinations are shown in Figure 5.1. The range of Vp/Vs values is from 1.46 to 2.05. Estimated percent difference between the two maps and a histogram of percent difference values are presented in Figure 5.2. Even though the range of values is large, most of the significant differences occur on the edge of the survey where the data are not reliable. The histogram confirms that most of the data are concentrated between  $\pm 5$  percent of difference. This can be expected because the fold decreases from the center of the survey to the edges (see Chapter 1 Figures 1.18 and 1.19). Thus, the data on the edges are less reliable and to compare, we need to look in outline on Figure 5.2.

The interval Vp/Vs, cannot be used for the complete lithology interpretation and characterization of the reservoir because of the thin heterogeneous nature of the reservoir units. Instead, the analysis of these results can help an interpreter to recognize the general trend of Vp/Vs.

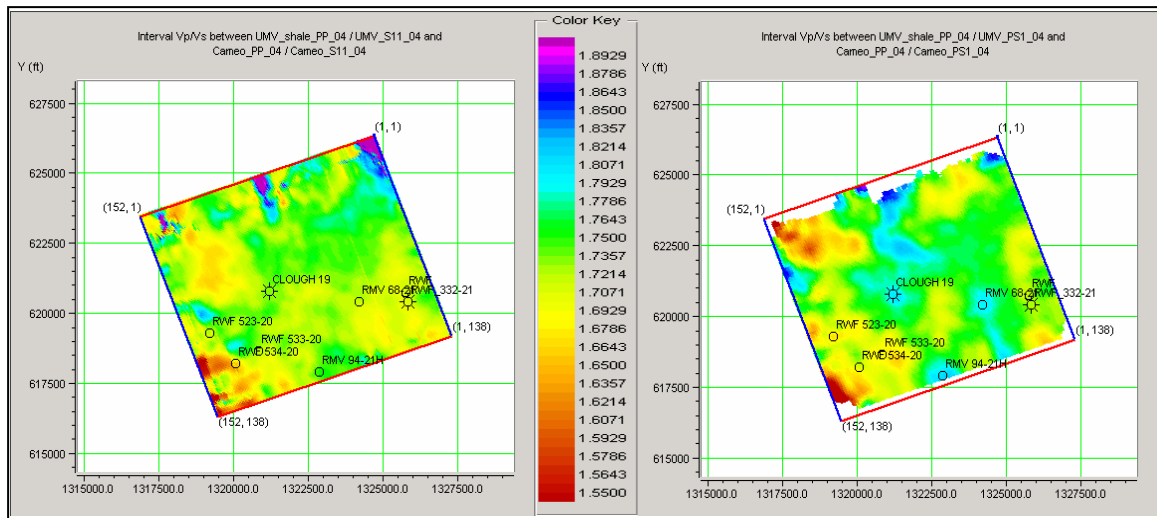


Figure 5.1 Interval Vp/Vs covering the zone between UMV-shale and Cameo-coal (reservoir interval). Left map represents the results from compressional and shear wave data. The map on the right is from compressional and converted wave data.

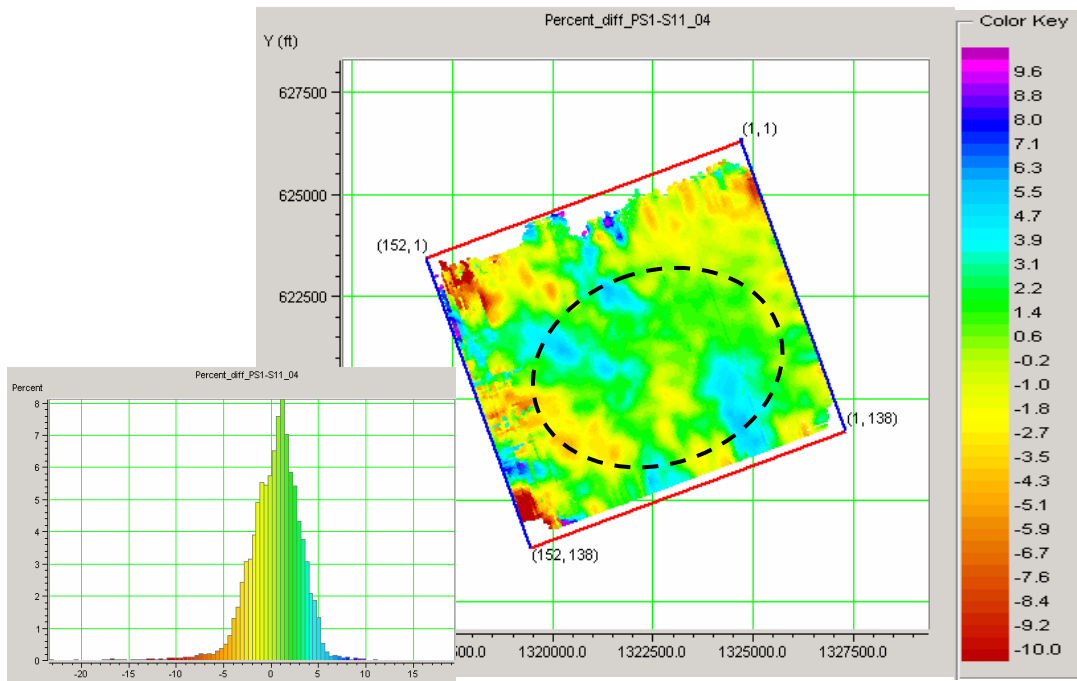


Figure 5.2 The percent difference map between Vp/Vs data slices generated from PP-SS and PP-PS data combination, and histogram of the data shown on color bar. The high fold area is outlined by the dashed ellipse.

The laterally distributed  $V_p/V_s$  values interpretation of travel time estimated velocity ratio is limited to the whole reservoir interval. This allows us to look at some average properties within this interval and correlate  $V_p/V_s$  with maps of estimated ultimate recovery (EUR) and net sand thickness estimated from gamma ray and density-porosity logs. This additional external information assists in conclusions about  $V_p/V_s$  trend and its correlation with EUR and net sand thickness and assessments from interval  $V_p/V_s$  values.

The two  $V_p/V_s$  maps are overlaid with EUR maps as shown in Figure 5.3. The EUR is represented by the bubbles with different colors. The area in the center of the survey showing higher values for  $V_p/V_s$  comprises several high EUR wells, up to 10 BCF. The actual correlation between low  $V_p/V_s$  and high EUR wells is not obvious.

Figure 5.4 represents the net sand thickness map from Williams Oil Company through the simultaneous interpretation of gamma ray, density and porosity logs (Figure 5.4a). The yellow color corresponds to the thicker net sand interval. The  $V_p/V_s$  map on the right image (Figure 5.4b) represents the average  $V_p/V_s$  values produced from compressional and shear wave data within the same interval of about 2,000 ft. According to the sand thickness map, higher net sand occurs in the western and southern portions of the survey. This correlates well with areas of low  $V_p/V_s$  on the right image. Even though the sand thickness decreases to the north, low  $V_p/V_s$  zones still are present. The EUR data also confirm higher productivity in these zones (Figure 5.3).

### **5.3 Impedance Derived $V_p/V_s$ Interpretation**

Now I shall consider the high resolution  $V_p/V_s$  derived from impedance results as a characterization tool. As one of the main goals of the research, I investigate possible applications of impedance derived velocity ratio for reservoir interpretation enhanced by other independent data.

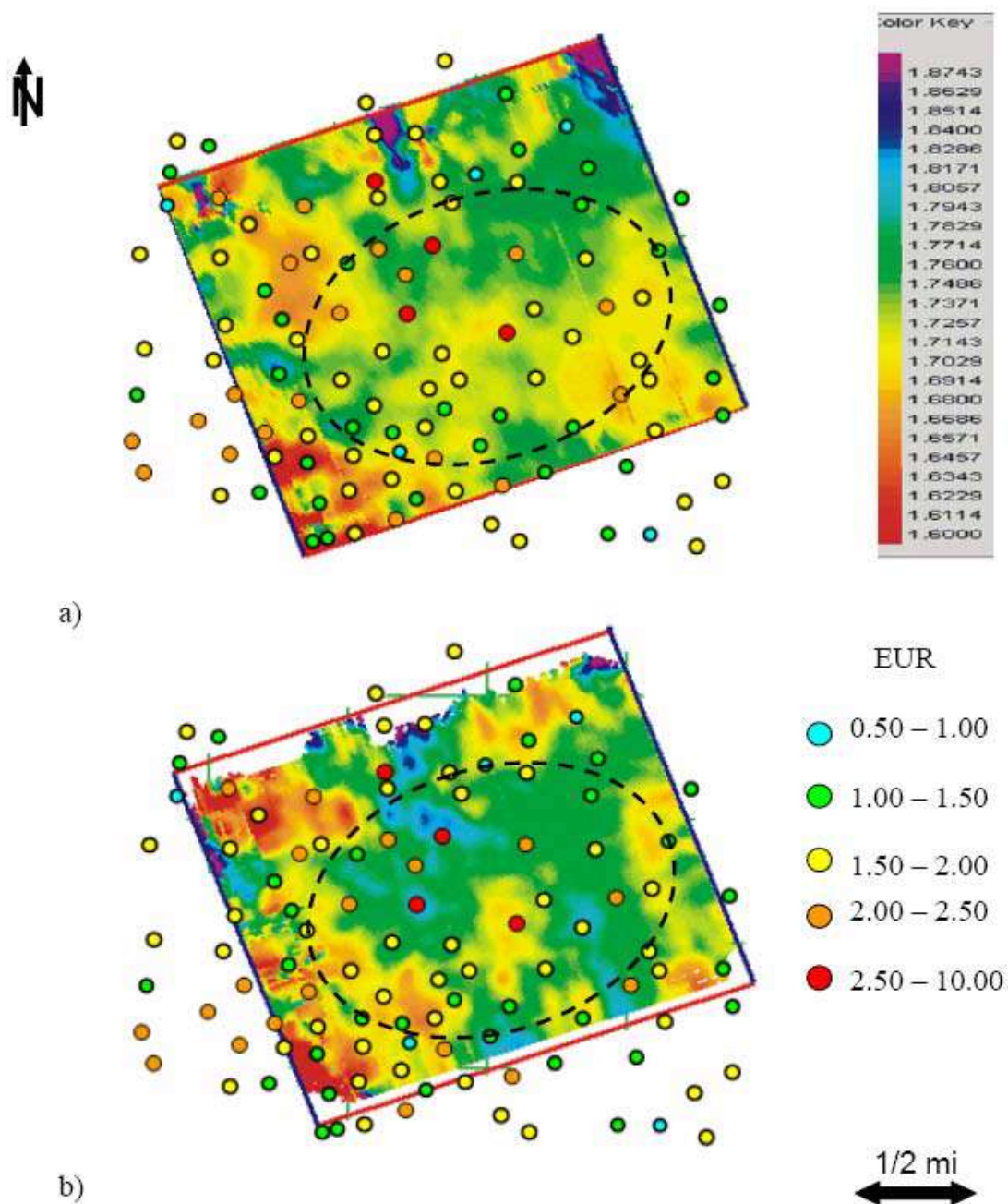


Figure 5.3 Interval  $V_p/V_s$  slices within the reservoir interval obtained from: a) PP-S11 data sets; b) PP-PS1 data sets. Overlaid bubbles represent estimated ultimate recovery provided by William Production. The color of the bubbles displays certain amount of gas in BCF. The high fold area is outlined by the dashed ellipse.



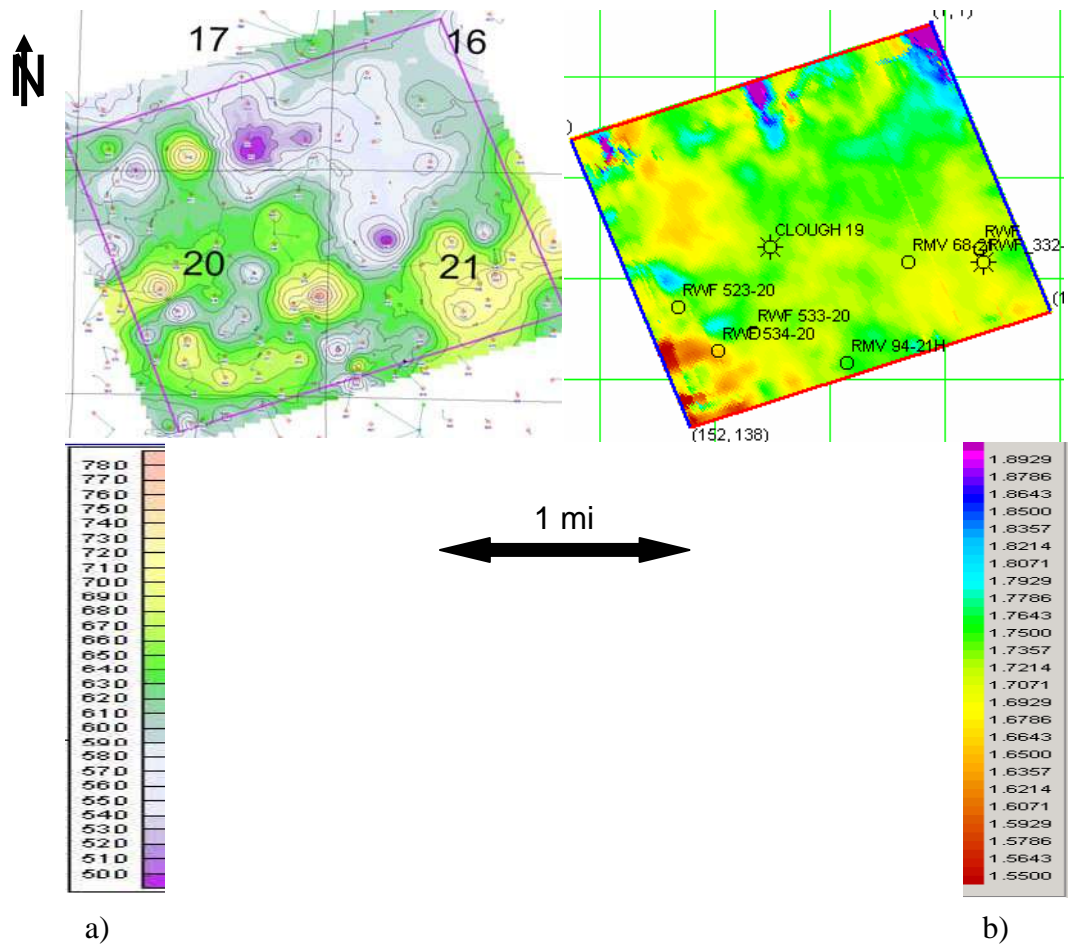


Figure 5.4 Net sand thickness map from Williams Production (a) versus Vp/Vs map generated from PP-S11 (b). The slices were generated within the reservoir UMW – Cameo interval. The areas of thick net sand sections are correlated with the areas of low Vp/Vs.

### **5.3.1 Three Dimensional Representation Of The Vp/Vs Results**

3-D visualization is a powerful tool for characterizing reservoirs. The availability of 3-D interactive programs may assist in interpretation of the Vp/Vs cube. This allows an interpreter to examine vertical sections in inline, crossline, or any arbitrary direction. In addition, horizontal sections - time or depth slices, can be viewed and studied within any interval.

The interpretation of the main horizons I fulfill in 2-D and display the results in 3-D perspective (Figure 5.5). Slightly dipping events can be determined very easily and some artifacts on the edges of the survey become more obvious. Figure 5.6 demonstrates the same horizons colored with Vp/Vs and an inline section extracted from the Vp/Vs cube.

I further investigate the distribution of Vp/Vs values within the reservoir visualizing the obtained volumes in 3-D. The combined plan and vertical sections reveal spatial and temporal changes of Vp/Vs associated with reservoir quality changes. Derived from seismic amplitudes the Vp/Vs cube is pictured in Figure 5.7. The color bar represents low values (1.7 and below) with reddish colors, while higher values are colored with darker grey and black colors. As it will be discussed below, more interest exists for low values of Vp/Vs because of their sensitivity to gas charged zones. I highlight the zones of Vp/Vs below 1.6 by shadowing high Vp/Vs values in Figure 5.8. This way of picturing the interval between top Mesaverde and top Cameo provides the sense of reservoir distribution in the subsurface. To display the overpressured zones, I dim the colors further in Figure 5.9, showing only the values below 1.5. The highlighted zones can be interpreted as bypass pay. According to the pictured features, the average area of the individual zones in the reservoir interval is about 30 acre (1,268,190 square feet) and vertically the zones range from 50 to 100 ft. It is important to consider this factor while planning a new drilling target. The histogram in Figure 5.10 discloses Vp/Vs values distribution within the reservoir interval percent wise. Most of the values are between 1.7 and 1.8. The reservoir contains about 45 % of Vp/Vs equalled 1.6. The



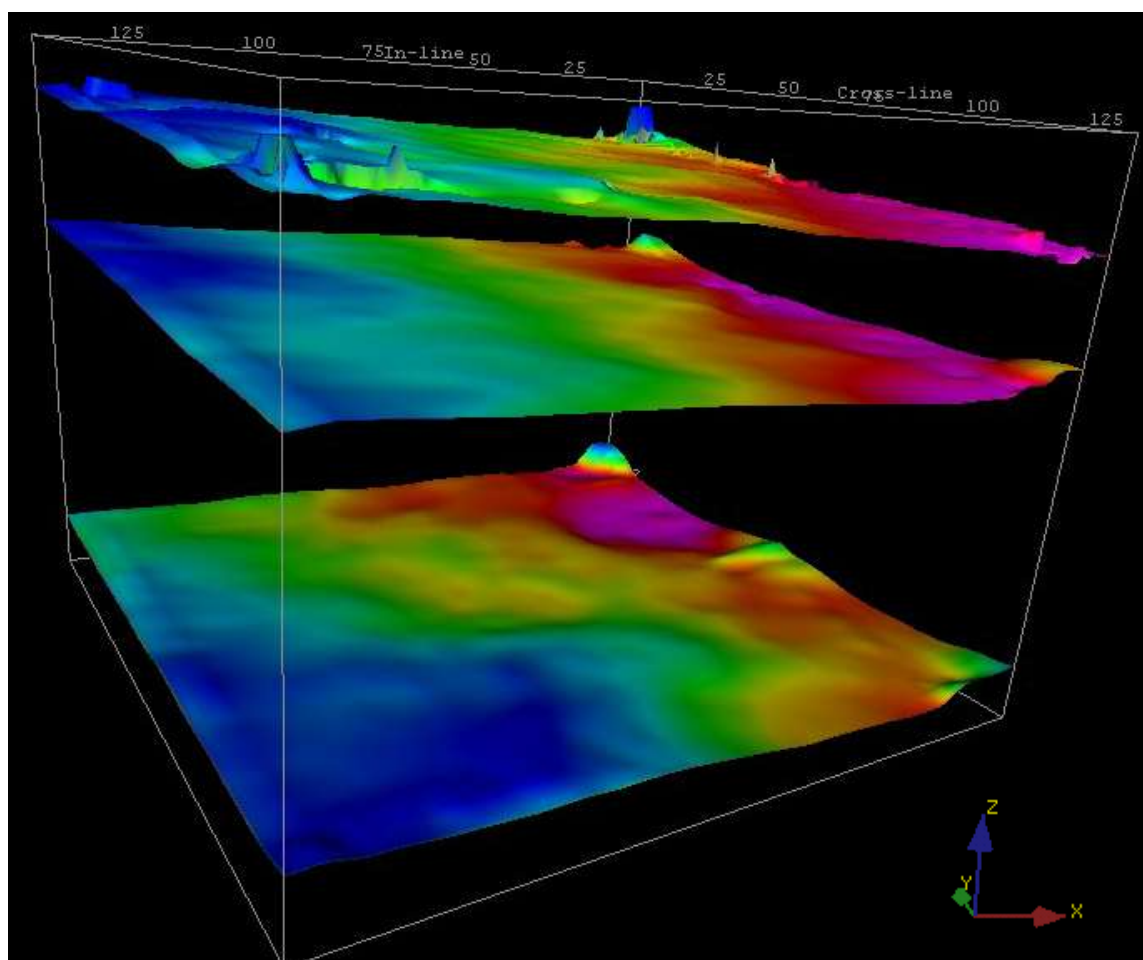


Figure 5.5 Seismic horizons dipping slightly in the Eastern direction. The corresponding events from top are: top of Mesaverde, top of UMV gas and top of Cameo coal.

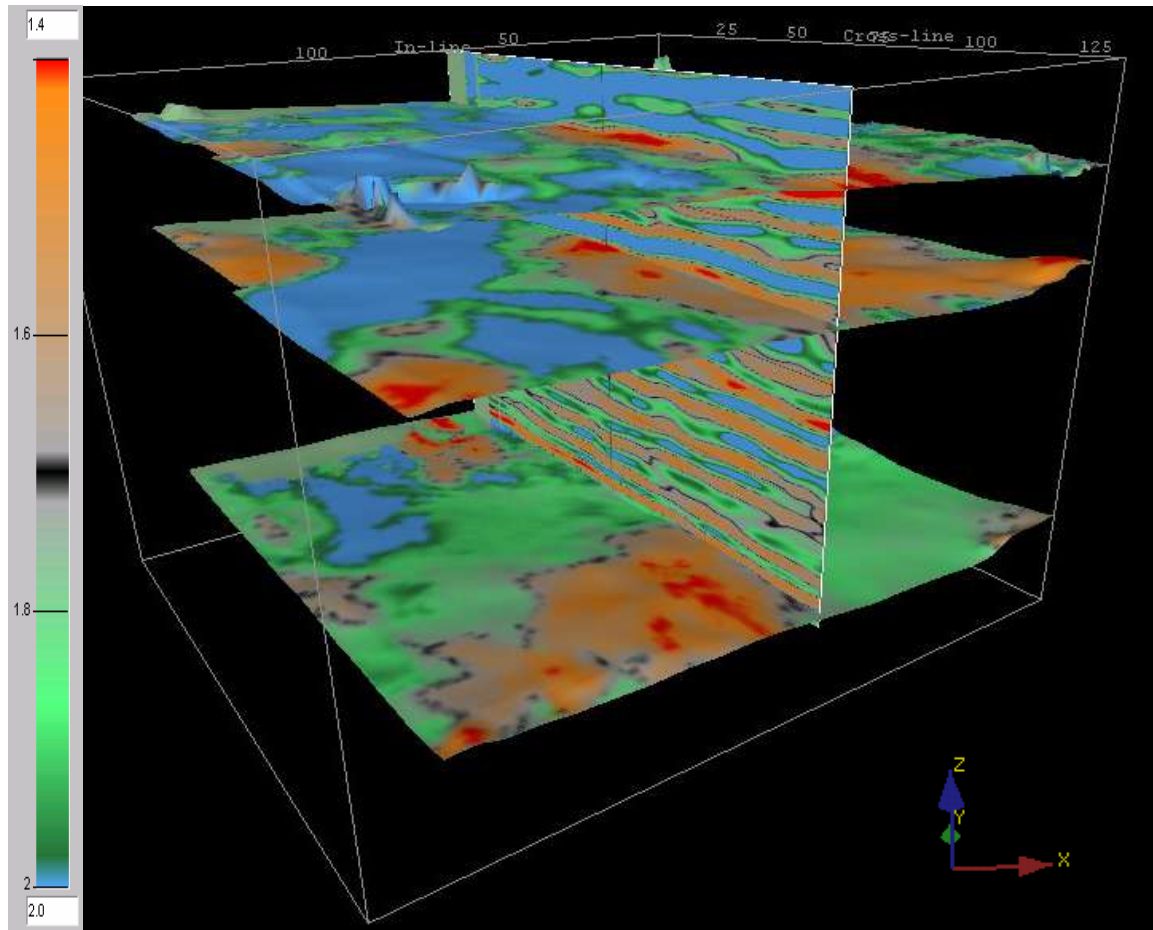


Figure 5.6 Seismic horizons colored with  $V_p/V_s$  values. The inserted vertical section from the estimated  $V_p/V_s$  volume assists in distribution analysis of velocity ratio.

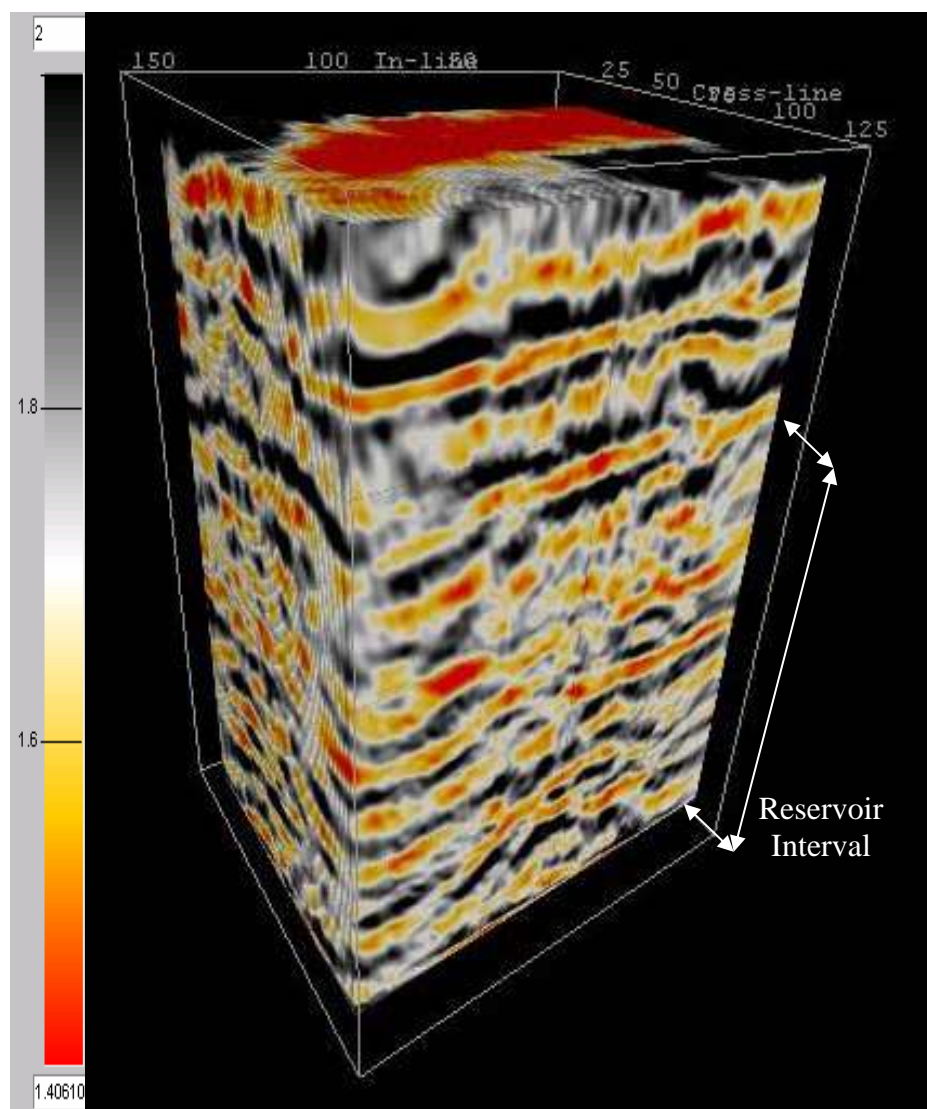


Figure 5.7 Impedance derived  $V_p/V_s$  volume estimated within Mesaverde – Cameo interval. The yellow-reddish colors represent low  $V_p/V_s$ .

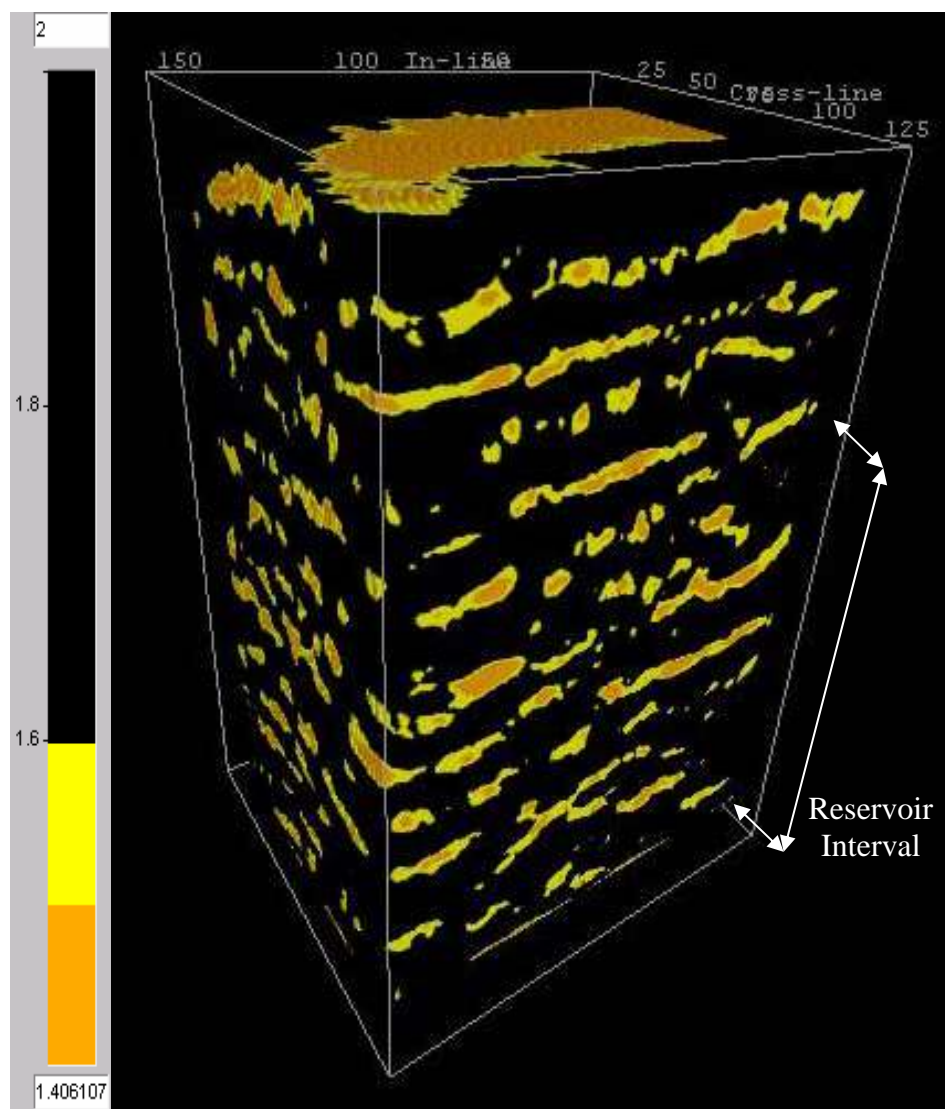


Figure 5.8 Impedance derived  $V_p/V_s$  volume estimated within Mesaverde – Cameo interval. The low values below 1.6 are highlighted representing potential gas charged sandstone zones.

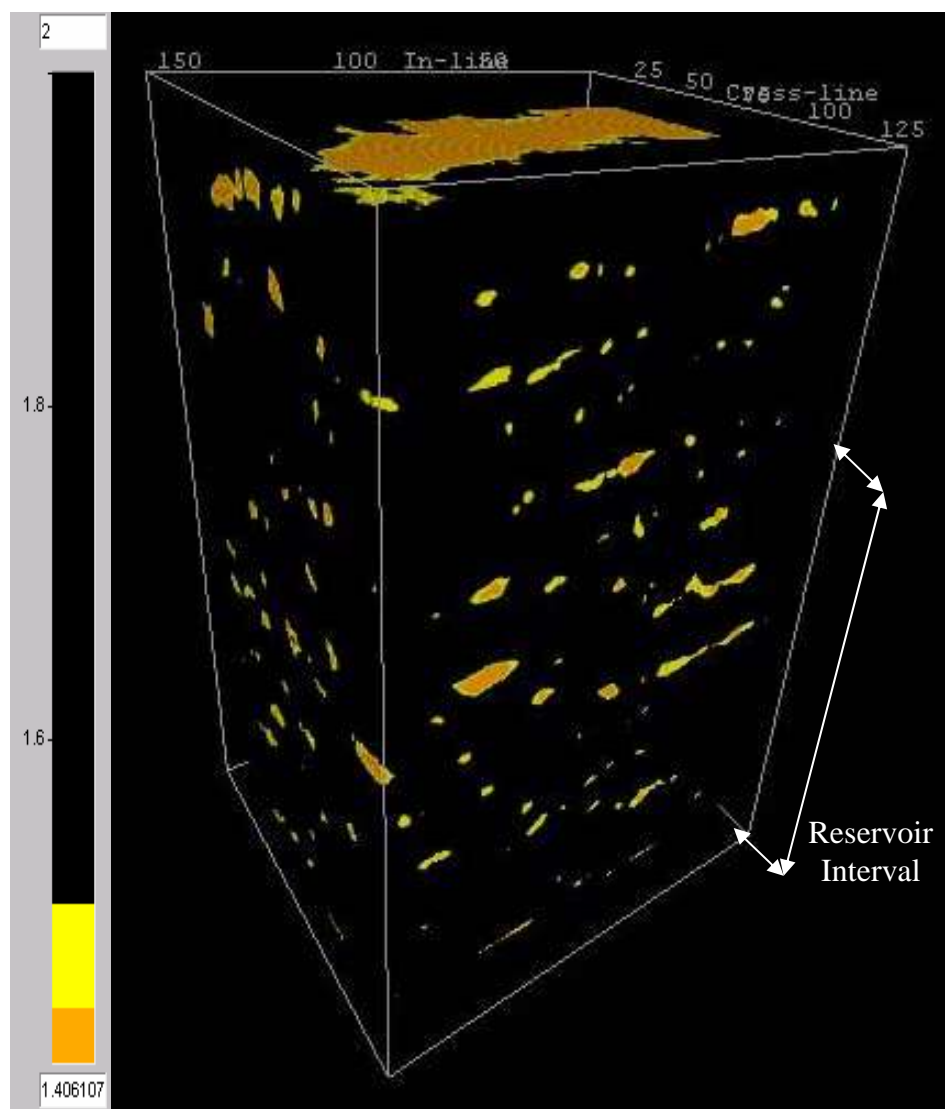


Figure 5.9 Impedance derived  $V_p/V_s$  volume estimated within Mesaverde – Cameo interval. The abnormally low values below 1.5 are highlighted representing potential overpressured gas charged zones.

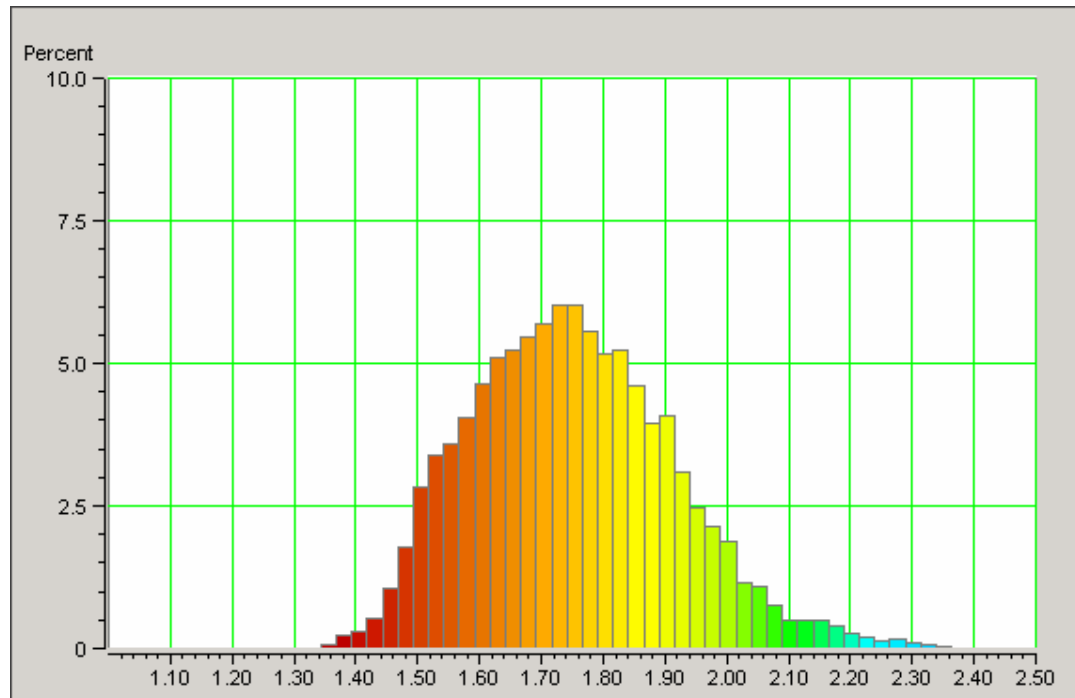


Figure 5.10 Histogram of  $V_p/V_s$  values distribution within the reservoir interval.

lower  $V_p/V_s$  values are distributed as follows: 30% of  $V_p/V_s = 1.5$  and 5% of  $V_p/V_s = 1.4$ .

### **5.3.2 Comparative Analysis Of $V_p/V_s$ With Time-Lapse Observations**

The seismic data were acquired in 2003 and 2004 and were processed to enhance the repeatability of two surveys specifically for the observation of time-lapse changes during a one year period of production. Time-lapse changes estimated from pure shear wave data within this period of time were studied by Rumon (2006). SS-wave time-lapse data enhance the understanding of reservoir connectivity, depleted intervals, and bypassed pay. Shear waves may provide the ability to avoid depleted intervals in new wells, and to identify bypassed pay interval penetrated by older wells (Rumon 2006).

Examining Vp/Vs within the areas of time-lapse anomalies, we can identify the velocity ratio sensitivity to the production and depletion of the reservoir. Depletion will cause a drop in pore pressure. Lowering pressure is detected by increasing Vp/Vs. Therefore, the zones of low Vp/Vs correspond to overpressured, bypassed zones.

The following demonstration is aimed to show the reciprocal relationship between two observations. A random inline in Figure 5.11 displays two sections representing Vp/Vs from PP-S11 (Figure 5.11a) and percent S-impedance difference (Figure 5.11b) estimated from 2003 and 2004 fast shear wave data sets. The color key is adjusted to represent only extreme values on both images, such as observed traces on Vp/Vs section are corresponding to very low and very high numbers (from 1.4 to 2.1), while the time-lapse section is displaying only the zones where the most changes took place (from -1% to +1%). Logically, the depletion interval will cause some time lapse anomalies, that can be observed within the small box and ellipse in Figure 5.11b. At the same time, Vp/Vs should show higher values in the depletion zones, since pressure drop increases Vp/Vs. The Vp/Vs values in Figure 5.11a within the same small box and ellipse are in the white range of the color bar, showing no extreme changes. On the other hand, the area of a large box in Figure 5.11a includes some Vp/Vs anomalies, where low values would correspond to gas charged sandstones. The same box on the right image (Figure 5.11b) does not exhibit any time-lapse anomalies suggesting the presence of a bypassed area.

More thorough analysis can be performed with 3-D viewing of the results. Figure 5.12 pictures inline and crossline of the time-lapse anomalies volume showing the percent impedance difference exceeding 3%. The Vp/Vs time slice represents the values less than 1.7. Zooming the area contoured by the dashed lines, it can be noticed that low Vp/Vs zones correspond to zero percent difference. This analysis may justify the proper usage of obtained Vp/Vs volumes for bypass zone identification and new production target identification.



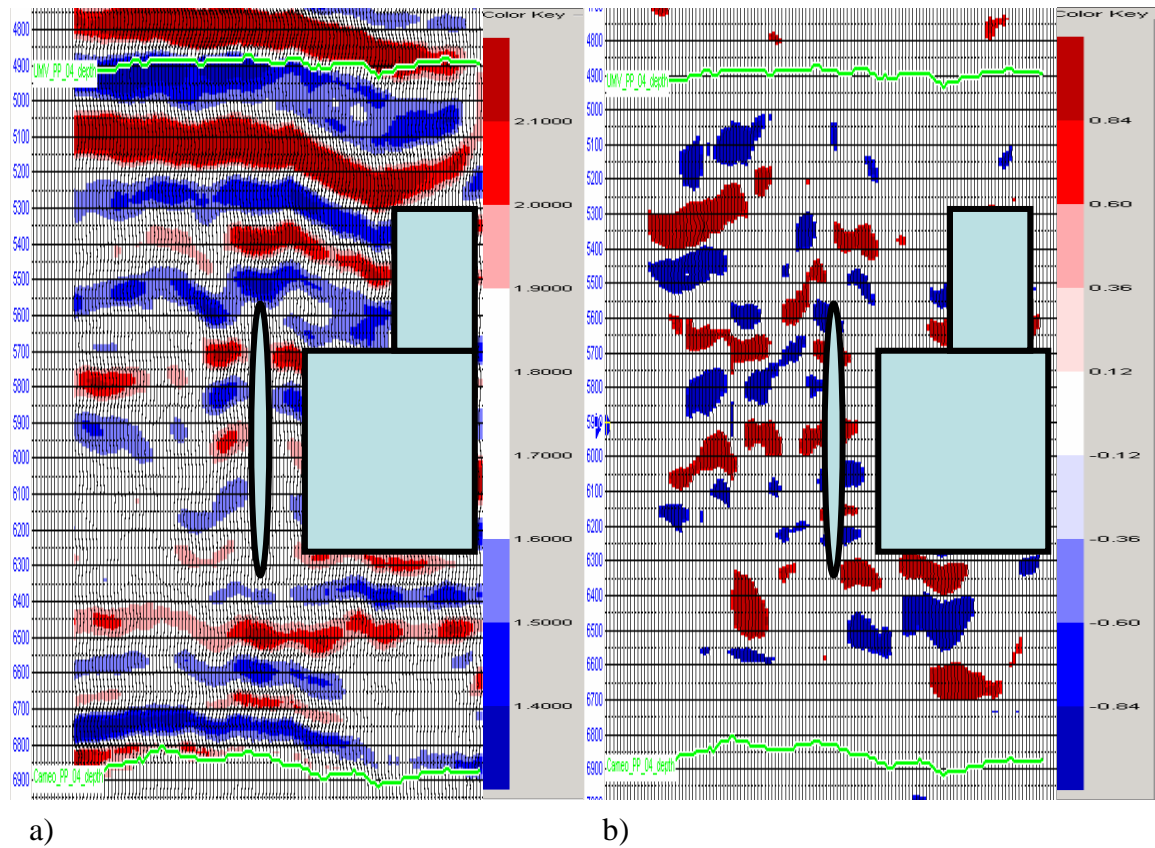


Figure 5.11 Inline 50 comparing: a) Vp/Vs cross section; b) Percent S-impedance difference between 2003 and 2004 surveys, estimated from S11 data. The sequence of low and high Vp/Vs values constrained by a black box corresponds to the area where no time-lapse changes are observed. The areas of normal Vp/Vs correspond more to significant 4D difference.



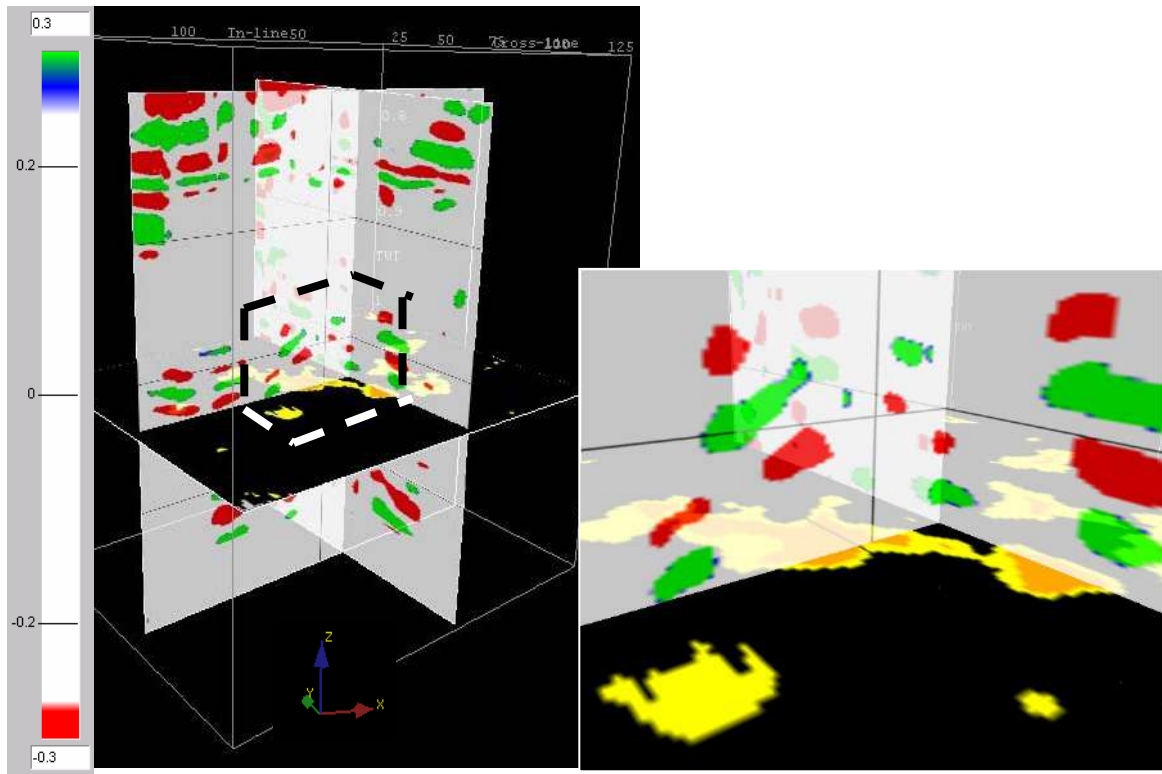


Figure 5.12 A random inline and crossline from the volume of percent impedance difference between 2003 and 2004, and low  $V_p/V_s$  time slice. The enclosing section is shown in the right. Time-lapse anomalies are not present in the areas of low  $V_p/V_s$ .

### **5.3.3 Depth Conversion**

The  $V_p/V_s$  volumes presented earlier are the result of step-by-step computation. Each step is carefully tested for the quality of the outcomes. Recognizing the errors at an early stage of the workflow may prevent some repetition and expansion of inaccuracies and propagation of the errors. Depth conversion serves as another test for the reliability of results. The process is described in this section.

Geologists and engineers are used to working in depth and to create a bridge between seismic survey and geology and engineering we need to transfer our data from

the time to the depth domain. Velocity information from different sources may be applied for this purpose; from seismic processing or log data. The inversion process itself provides a velocity field for depth conversion when tied to the wells.

The depth transformation is also an additional verification for the correctness of the impedance inverted results. To separate velocity and density from impedance inverted volumes, the Gardner's formula is commonly used:

$$\rho = cV_P^{0.25}, \quad (5.1)$$

where C – constant that depends on the rock type.

Applying this equation, the computing program of Hampson and Russell generates the PP and SS velocity volumes along with the acoustic and shear impedance estimation. According to Yilmaz (2001), the velocity derived from surface registered seismic data is the stacking velocity that produces the best trace summation. Shown in Figure 5.13 are the seismic traces colored with P-wave (Figure 5.13a) and S-wave (Figure 5.13b) velocity cubes. The changes occur in both vertical and horizontal directions, which implies higher resolution of estimated velocity volume in comparison with interval or extrapolated sonic log data.

Velocity volumes enable the sample by sample recalculation of vertical scale from time to depth. If the transformation positions the seismic events within the same depth interval as the well tops, then the applied velocity is usable and impedance estimation is done successfully. The absolute values, as determined from the color key in Figure 5.13, demonstrate the velocity for P-wave data are twice as fast as for S-wave.

To check the velocity volumes for their robustness, I convert the Vp/Vs cube estimated from PP-S11 data set to depth through the process of flattening the top of Mesaverde at some depth point (estimated from the well tops) and applying the velocity results to change the time domain to depth domain of the interval below. The picked

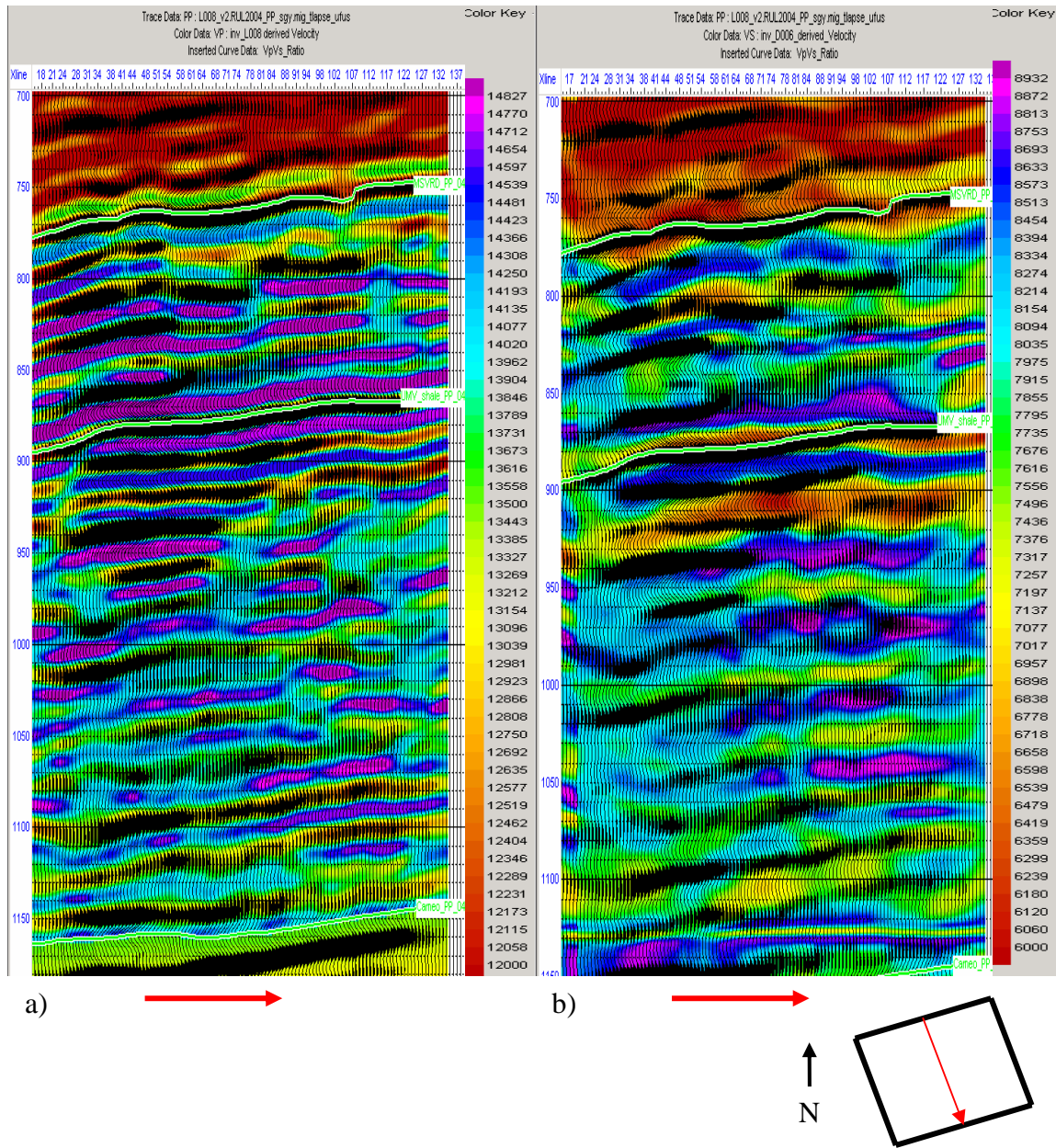


Figure 5.13 A random line of seismic wiggle traces in the middle of the survey colored with: a) P-wave velocity generated from impedance inversion of compressional wave data; b) S-wave velocity generated from impedance inversion of shear wave data. Both sections are shown in PP time.

horizons are converted by program from PP and SS time domains along with the seismic data for visual correlation with the well tops in depth domain. The result of P-wave and S-wave velocity application is demonstrated in Figures 5.14a and 5.14b. The depth difference between corresponding horizons is about 100 ft. The converted from time events are also in good agreement with the tops distinguished from the well log data. This result suggests the appropriate usage of both velocity cubes for depth conversion and confirms the robustness and accuracy of the inversion algorithm results.

#### **5.3.4 The Sensitivity Of Generated Vp/Vs Volumes To The Lithological Components Of The Reservoir**

In this section I progress with building a basic model for lithologic discrimination. Figure 5.15 displays the map view of 73 wells involved in the process of the lithological model development. This is the number of wells where a gamma ray tool was run, and the registered borehole data were normalized for casing. However, total gamma ray is not the most reliable tool for sand and shale delineation in this environment. An X-Ray Diffraction study, performed by a service company, K/T GeoServices in four core samples from the field, determined that quartz and plagioclase, are the most common minerals in the rocks. Table 5.1 characterizes phyllosilicates that were found in all samples. The phyllosilicates, or sheet silicates, are an important group of minerals that includes the micas, chlorite, serpentine, talc, and the clay minerals. The analysis showed that sand bodies contain a lot of illites and micas (Table 5.1), which add larger radioactive emissions, so that registered gamma ray shows an API higher than we expect from clean sandstones. The clay also reduces porosity so that density-porosity logs are not able to differentiate shale from sand. Nevertheless, using the cutoff at 80 and assuming everything below this number being the response to the sand, I can project some of the non-continuous sand rich zones.

Close spacing of the wells gives me the possibility to use the inverse distance power function to interpolate the gamma ray log data between nearby wells. This way I



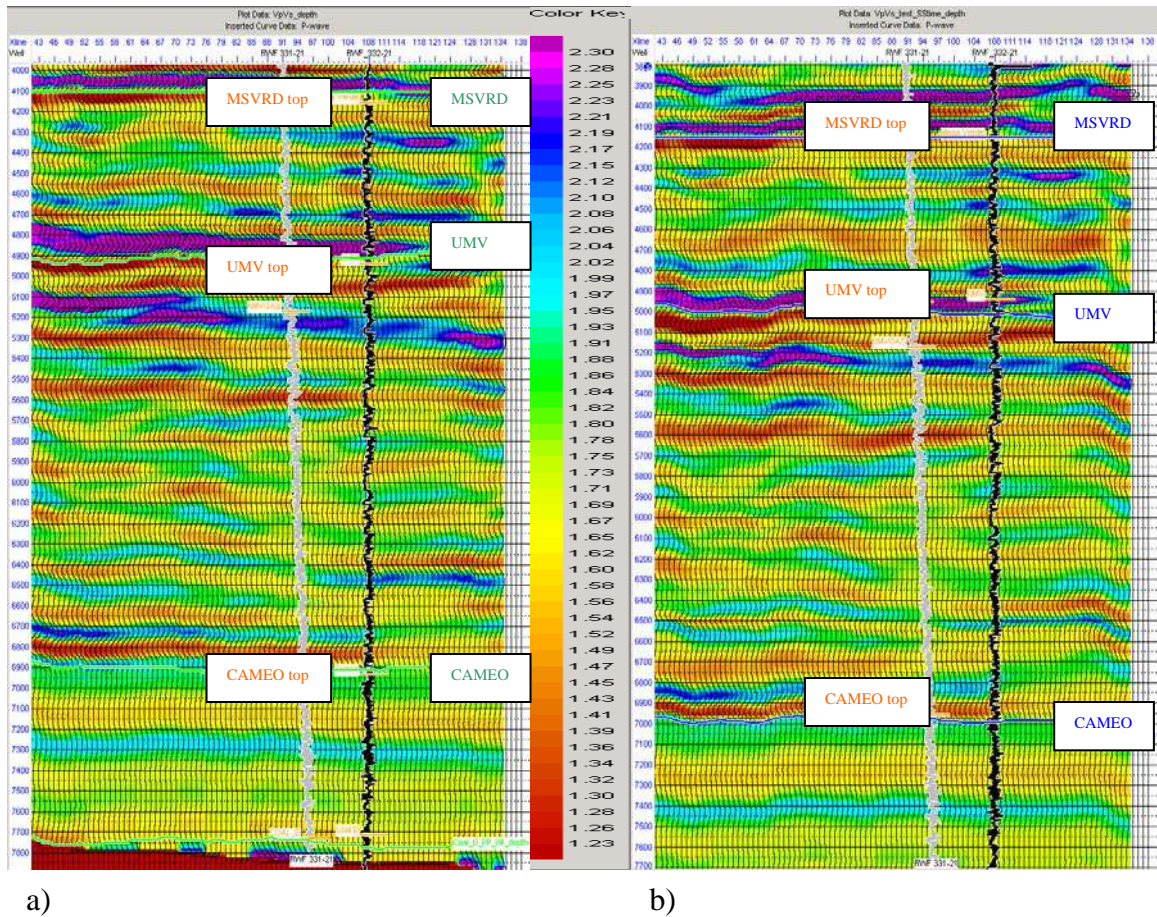


Figure 5.14 Vp/Vs section transformed to depth domain with: a) P-wave velocity; b) S-wave velocity. Shown inline 18 presents a good correlation between well tops and depth converted horizons. The same events correspond to slightly different vertical scale on two images. It can be concluded that both velocity volumes are usable for depth conversion.

can look at the sand bodies in a cross section view and compare it with extracted earlier Vp/Vs. Thus, Figure 5.16 demonstrates a line from the interpolated lithological model. The inserted curve represents the Vp/Vs ratio of the velocities obtained from the dipole sonic log, filtered down to the seismic resolution. The image clearly demonstrates lower

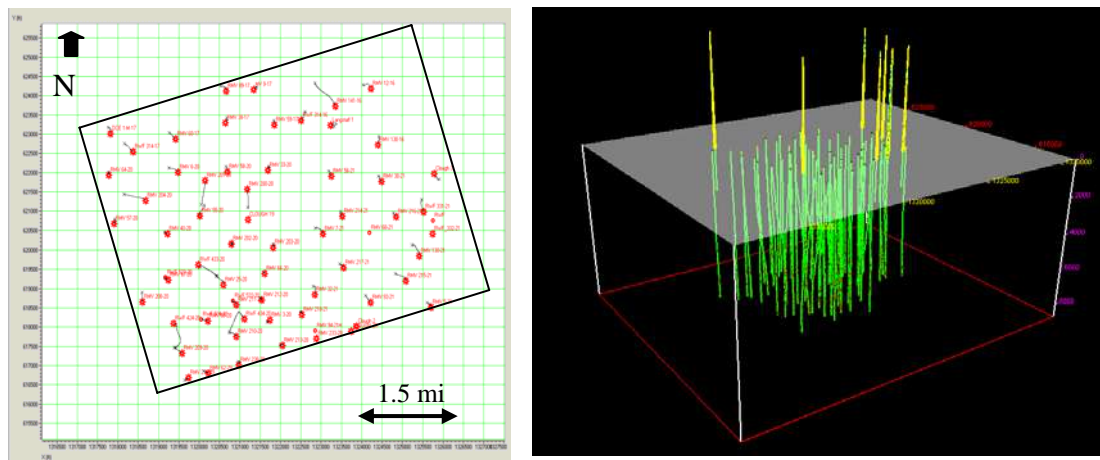


Figure 5.15 Location of the wells included in lithological model building.

Sample	R-6451.5V	R-5702V	R-5719V	R-5727.1V
Mixed layer Illite-Smectite	20%	0%	17%	18%
Illite & Mica	79%	62%	69%	70%
Kaolinite	0.1%	8.1%	2.8%	2.4%
Chlorite	0%	30%	11%	9.7%

Table 5.1 Relative abundance (percentage) of phyllosilicate mineralogy from XRD (Rojas 2005).

Vp/Vs values in the areas of sand presence. Eugenia Rojas (2005), from her extensive work, concluded that: “Vp/Vs is sensitive to gas in this reservoir and will show a marked decrease in its presence”. The plots shown in Figure 5.17 demonstrate the relationship between the results from gamma ray log, which plays the role of a lithology indicator,

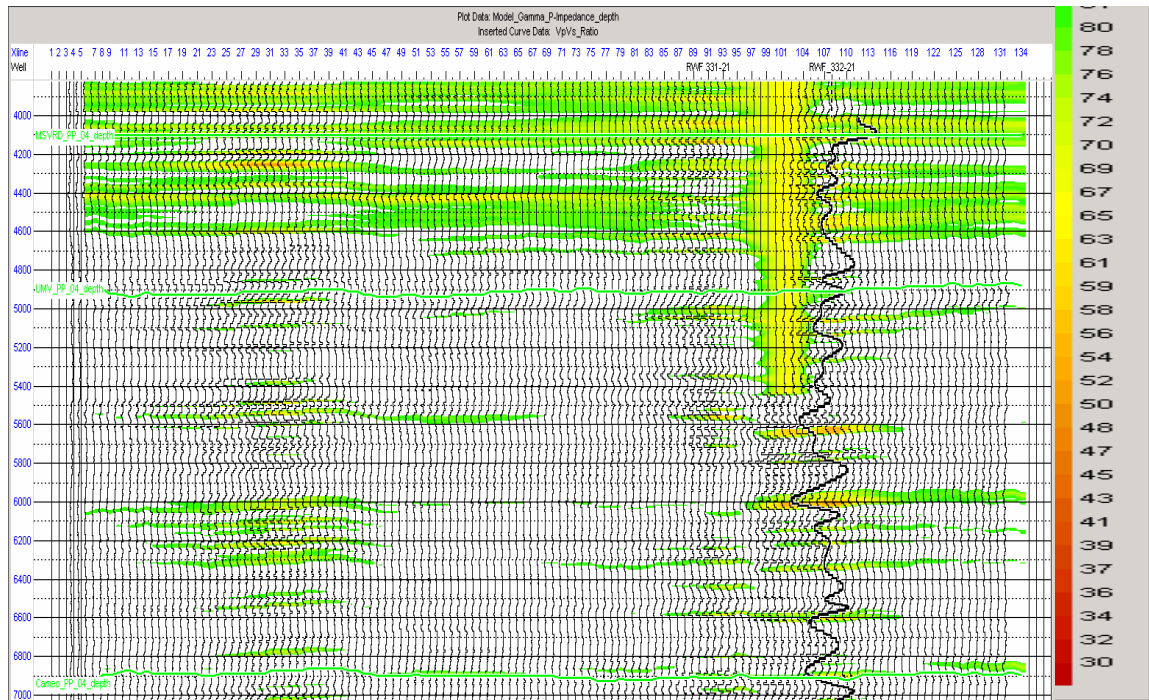


Figure 5.16 The cross-section of the model built by interpolating gamma ray log results from 73 wells. The color bar represents API values with a cutoff at 80. The black curve is the log  $V_p/V_s$  estimated from dipole sonic log. Low  $V_p/V_s$  correspond to low gamma ray zones.

and such parameters as P-, S-impedance and their ratio. The data are collected in well RWF 332-21 within the depth interval between UMV and Cameo and colored with depth. For better visualization the red curves on the plots refer to a trend line of the points distribution. Both impedances reveal a changing point of the trend line at 80 API. Usage of only P-impedance may lead to ambiguous conclusions, since the same impedance value may correspond to different API number of gamma ray, as it can be observed on the plot (Figure 5.17a). This can be explained by the sensitivity of compressional wave velocity to the fluid content, present in sand and shale formations. S-impedance (Figure 5.17b) reveals more distinguishable results, where impedance values stay relatively stable

in the sand zone but decrease rapidly in the shale zone. The trend line on Figure 5.17c remains straight declining towards lower values on both abscissa and ordinate axes implying a better sensitivity of  $V_p/V_s$  to lithological content. Therefore, I can use impedance derived  $V_p/V_s$  for the lithological description of the reservoir.

The gamma ray or lithological model is extended to the whole area of investigation. The comparison of seismic derived  $V_p/V_s$  and the extrapolated gamma ray model will demonstrate the match between  $V_p/V_s$  values and lithological content. A wrong interpretation from log data, caused by logging problems, may contribute to misfits but general trend of low  $V_p/V_s$  and sandstone distributions within the reservoir can still be investigated. Does it imply that seismic results are more reliable than log data? Probably not, impedance derived  $V_p/V_s$  computation involved only seismic reflection amplitudes, but one advantage of seismic is its spatial coverage. The log data are used as a supporting material for  $V_p/V_s$  stratigraphic interpretation. Demonstrated in Figure 5.18 volume is represented by superimposed layers of estimated  $V_p/V_s$ . It is beneficial to examine the volume by slicing it at smaller intervals to be able to differentiate  $V_p/V_s$  response to the reservoir, filled with gas sandstones under overpressure conditions. In reality, the purpose of the slicing is not the hunting for individual thin layer sandbodies, which are below the seismic resolution, but investigation of stacked sand bodies, which gives rise to low  $V_p/V_s$  response.

### **5.3.5 Data Slicing**

As discussed above low  $V_p/V_s$  is a potential indicator of sand presence. The laboratory measurements showed that tight sandstones typically have a  $V_p/V_s$  lower than 1.7, while shales have values larger than that. The presence of gas-saturated sandstones lowers the  $V_p/V_s$  even further ( $V_p/V_s$  of 1.6 or lower) and overpressure conditions can lower  $V_p/V_s$  even to the point below 1.5 (Rojas 2005). These numbers reflect lithological and environmental conditions of the reservoir. With the extracted  $V_p/V_s$



volume, it is more feasible to study the general trend of low  $V_p/V_s$  value distribution, the general orientation and possible connectivity within the reservoir.

Two independently registered data sets were used in the process of  $V_p/V_s$  estimation, PP-S11 and PP-PS1. The consideration of both of these combinations adds more confidence to the interpretation of velocity ratio volumes and conclusion about reservoir quality. Thus, if both data sets demonstrate similar patterns of low  $V_p/V_s$  within the same interval, one can interpret it as a bypassed zone. However, all available data must be included to avoid some misinterpretation due to erroneous  $V_p/V_s$  results. Referring to the depth converted  $V_p/V_s$  volumes, the reservoir interval, bounded by UMV at the top and Cameo at the bottom, is corresponding to the vertical scale roughly at 5000 and 7000 ft. I divide this thickness of 2000 ft by smaller sections, which consist of 100 ft. I also compute the arithmetic mean of  $V_p/V_s$  values at each section with an area covering the whole survey and thickness of around 100 ft, which is defined by the estimated seismic resolution (see Chapter 2). Figures 5.19 – 5.26 illustrate the  $V_p/V_s$  slices generated at different depth intervals starting with the depth 5400 ft – top of gas saturated reservoir (see Figure 1.4 in chapter 1 for details). Since there is no free water within this section and gas is not a factor of change, all the observed anomalies of low  $V_p/V_s$  (below 1.6) correspond to overpressure conditions. In addition, the lithological model calculated from gamma ray logs was sliced within the same intervals to study the lithological correlation with  $V_p/V_s$  maps. The usable high fold area of seismic, where the data produce more reliable results is projected on the depth interval slices. The short description of each of those intervals, indicating the possible target zones, is presented below.

As presented in Figure 5.19, there is a high concentration of low  $V_p/V_s$  (1.7 and below) on the western side indicating the gas saturation in this zone and probable overpressure condition in the area where  $V_p/V_s$  reaches 1.4. Low  $V_p/V_s$  area on the

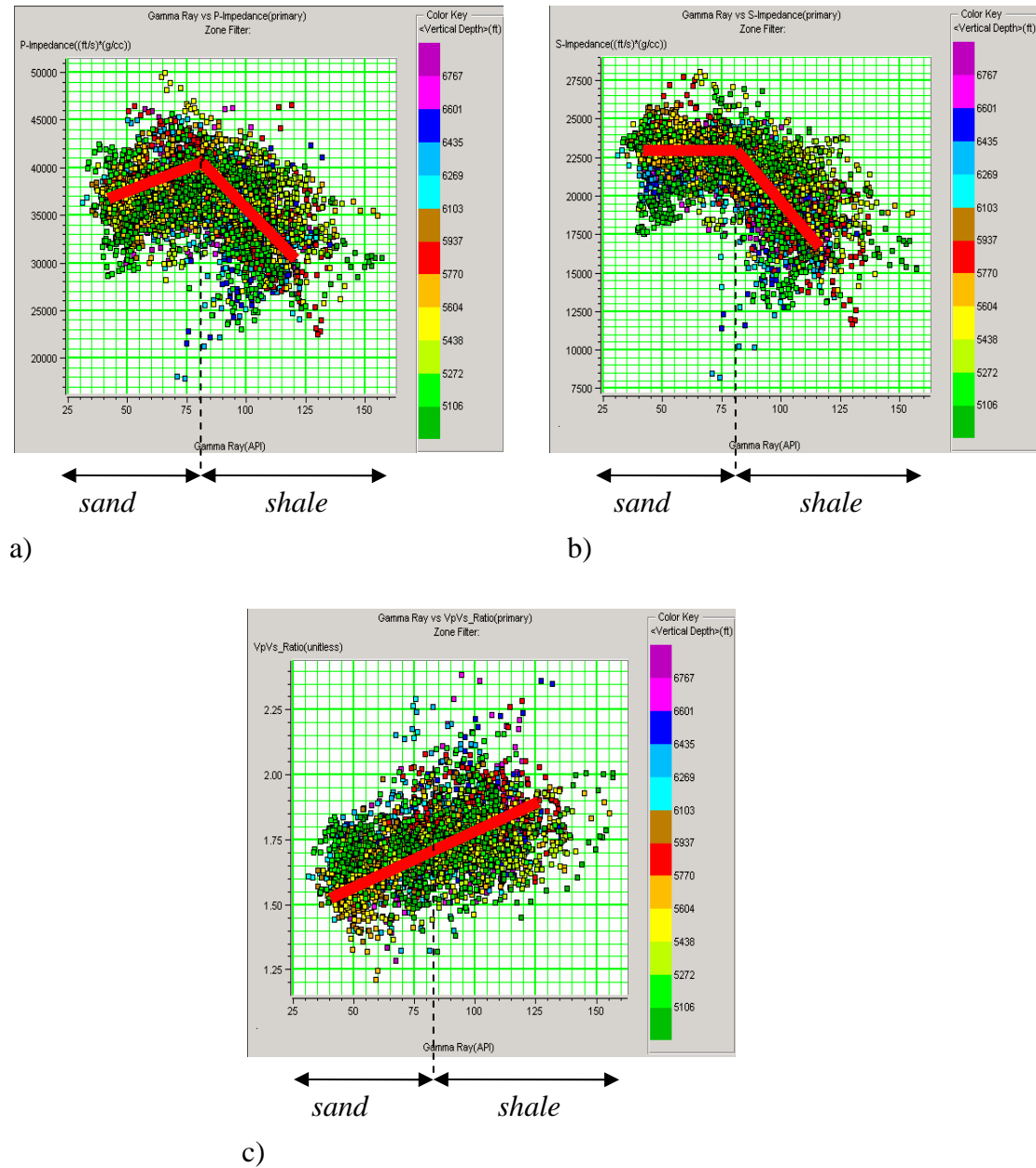


Figure 5.17 The cross plots of gamma ray versus: a) P-impedance; b) S-impedance; c) Vp/Vs. The color code is the depth interval bounded by UMV and Cameo well tops. The red line on each plot represents the average numbers and displays the general trend of the scattered points.

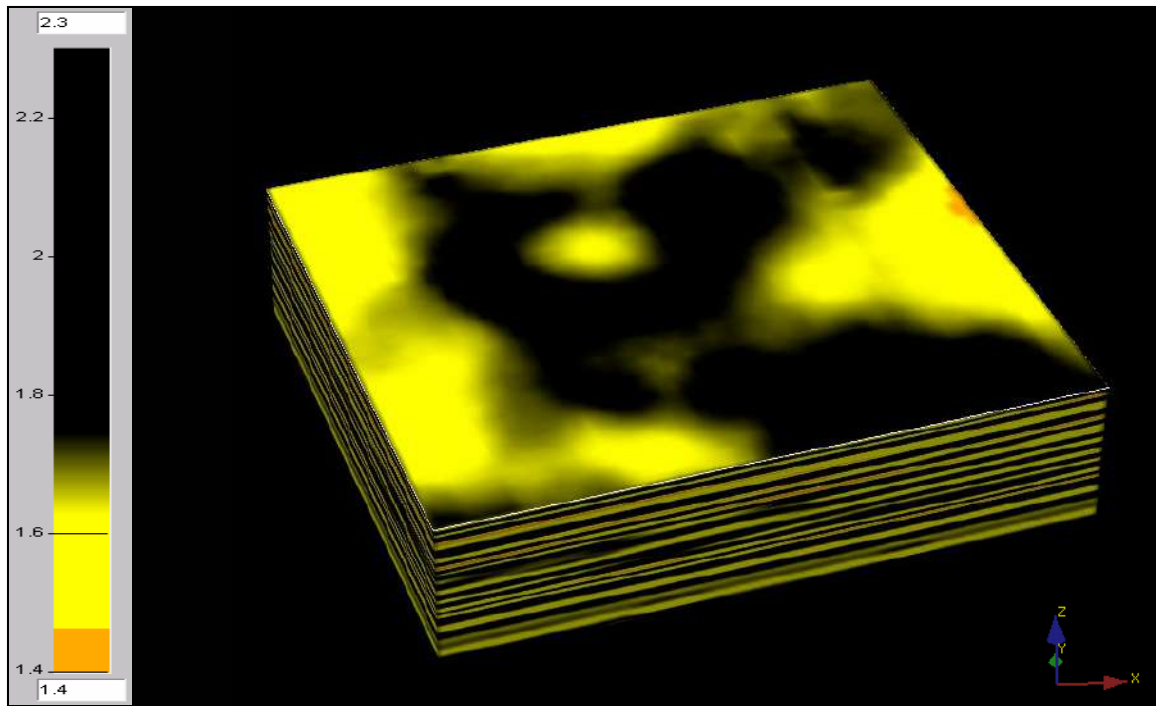


Figure 5.18 Reservoir volume sliced in the middle and colored with  $V_p/V_s$  values. The stacked layers form the volume. Each layer can be examined individually to provide more detailed and accurate interpretation.

west seems to be bounded next to well Clough 19.

The slices in Figure 5.20 from 550 to 5600 ft demonstrate the concentration of overpressure zones in the eastern part of the survey. This is a good example of heterogeneity of the reservoir and how fast the lithological changes occur within the vertical section. The gamma ray model reveals a similar picture of sandstone distribution in this interval.

The slices generated within the 5600-5700 ft interval (Figure 5.21) represent very good match with lithology in the northern and central part of the study area. The  $V_p/V_s$  maps show low  $V_p/V_s$  distribution with a general north-south trend.

Figure 5.22 displays a good correspondence of  $V_p/V_s$  and modeled sand-shale distribution in the 5700 – 5800 ft interval. Notice low  $V_p/V_s$  anomalies around well Clough 19 in the middle of the survey demonstrating a potential non-depleted interval. The next depth interval in Figure 5.23 does not reproduce that anomaly.

The depth interval of 5900 – 6050 ft shown in Figure 5.24 exhibits a very good coverage of low  $V_p/V_s$  within the area of interest. A concentration of sandstone deposits can be expected in this vertical section. Some bypassed zones detected by both velocity ratio maps are around already existing wells.

As shown in Figure 5.25, well RMV 68-20 in the eastern corner of the survey is surrounded by higher values of  $V_p/V_s$  but at interval 6300 – 6400 ft (Figure 5.26) this area can be targeted for gas.

Overall interpretation of both PP-S11 and PP-PS1, generated within the same interval,  $V_p/V_s$  maps shows the general orientation of sand rich areas. Consequently,  $V_p/V_s$  values from seismic can be tied to lithology components and zones of higher fluid pressure lowering  $V_p/V_s$ . As observed through the different levels of the reservoir, a concentration of low  $V_p/V_s$  is encountered in the western and southern parts of the survey. This observation is also confirmed by high EUR and thick net sand in the specified areas (see Figures 5.3 and 5.4).

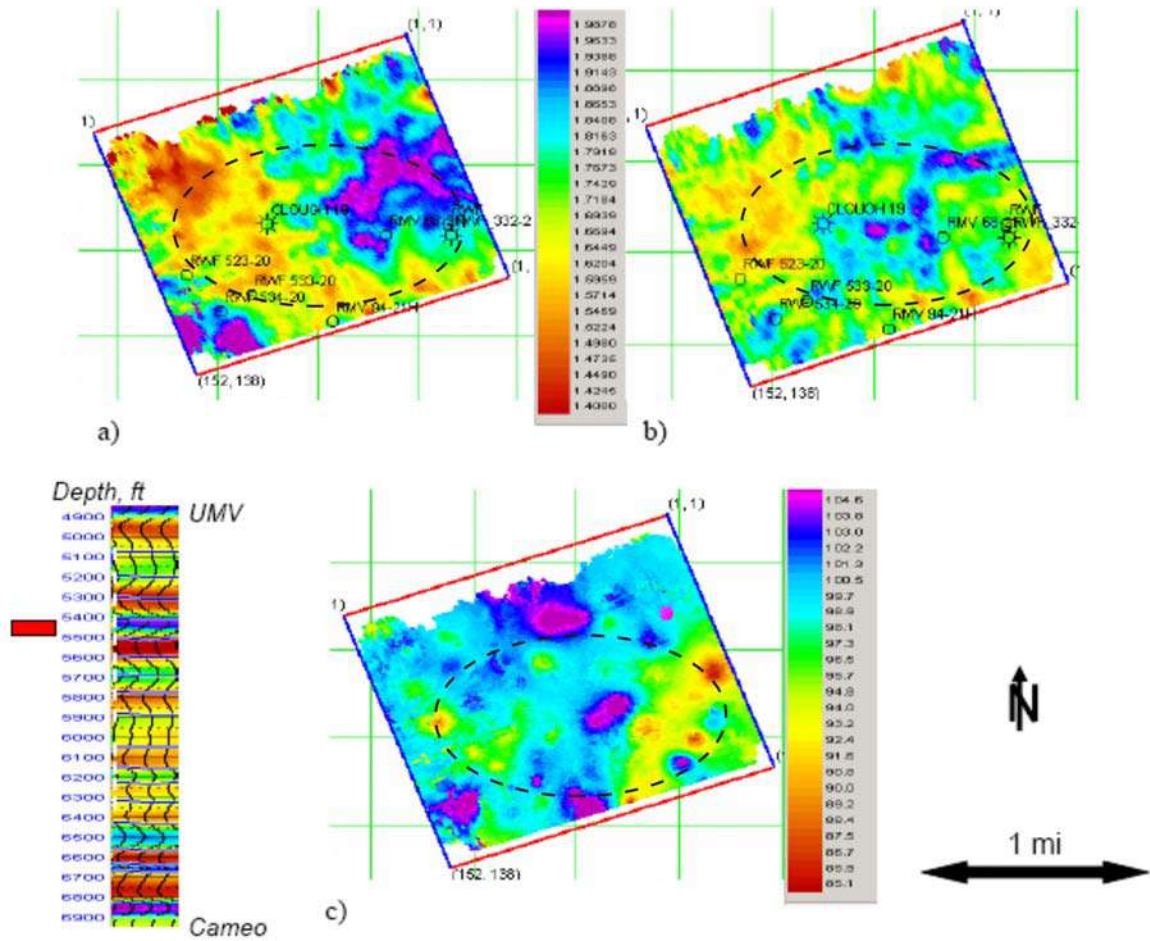


Figure 5.19 Depth interval slices generated within the 5400-5500 ft interval: a) Vp/Vs computed from PP-S11; b) Vp/Vs computed from PP-PS1; c) interpolated gamma ray model. The dashed ellipse outlines the seismic high fold coverage.

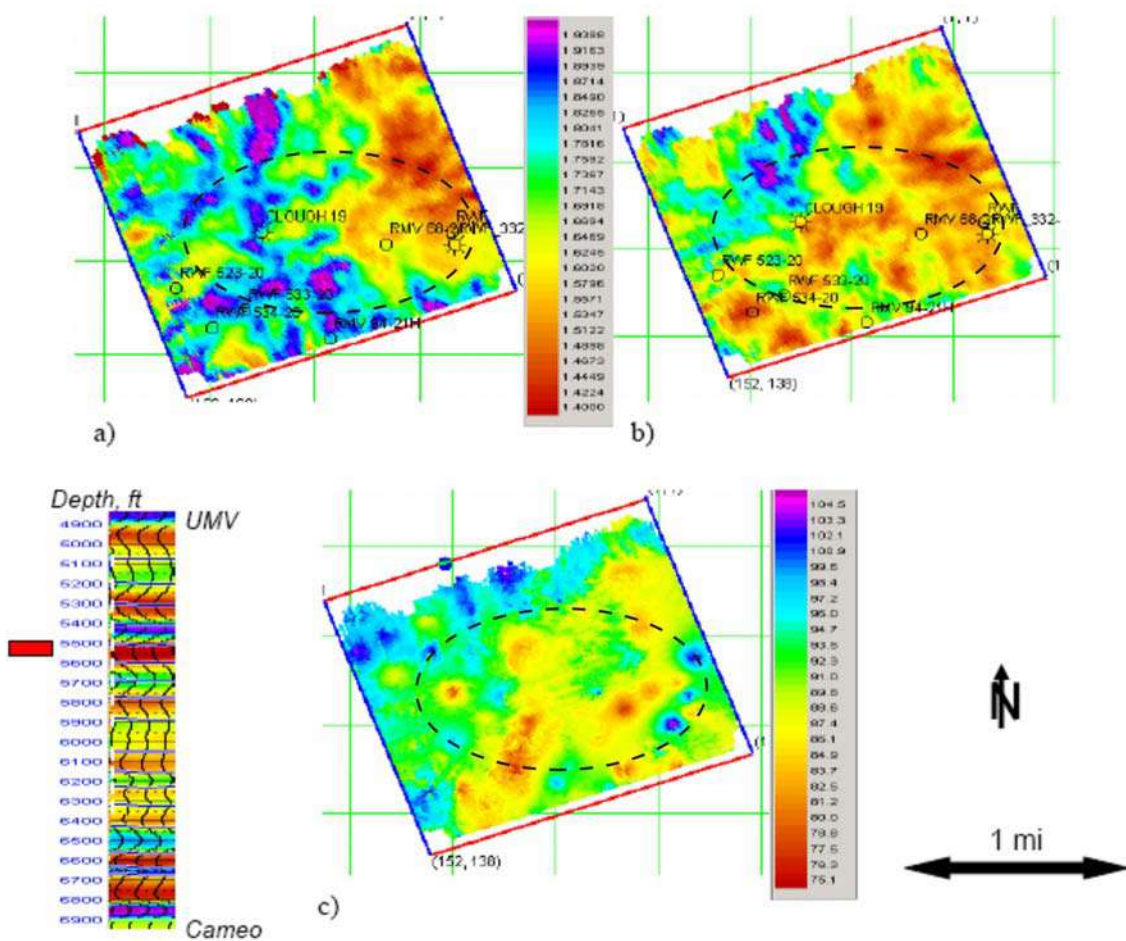


Figure 5.20 Depth interval slices generated within the 5500-5600 ft interval: a) Vp/Vs computed from PP-S11; b) Vp/Vs computed from PP-PS1; c) interpolated gamma ray model. The dashed ellipse outlines the seismic high fold coverage.



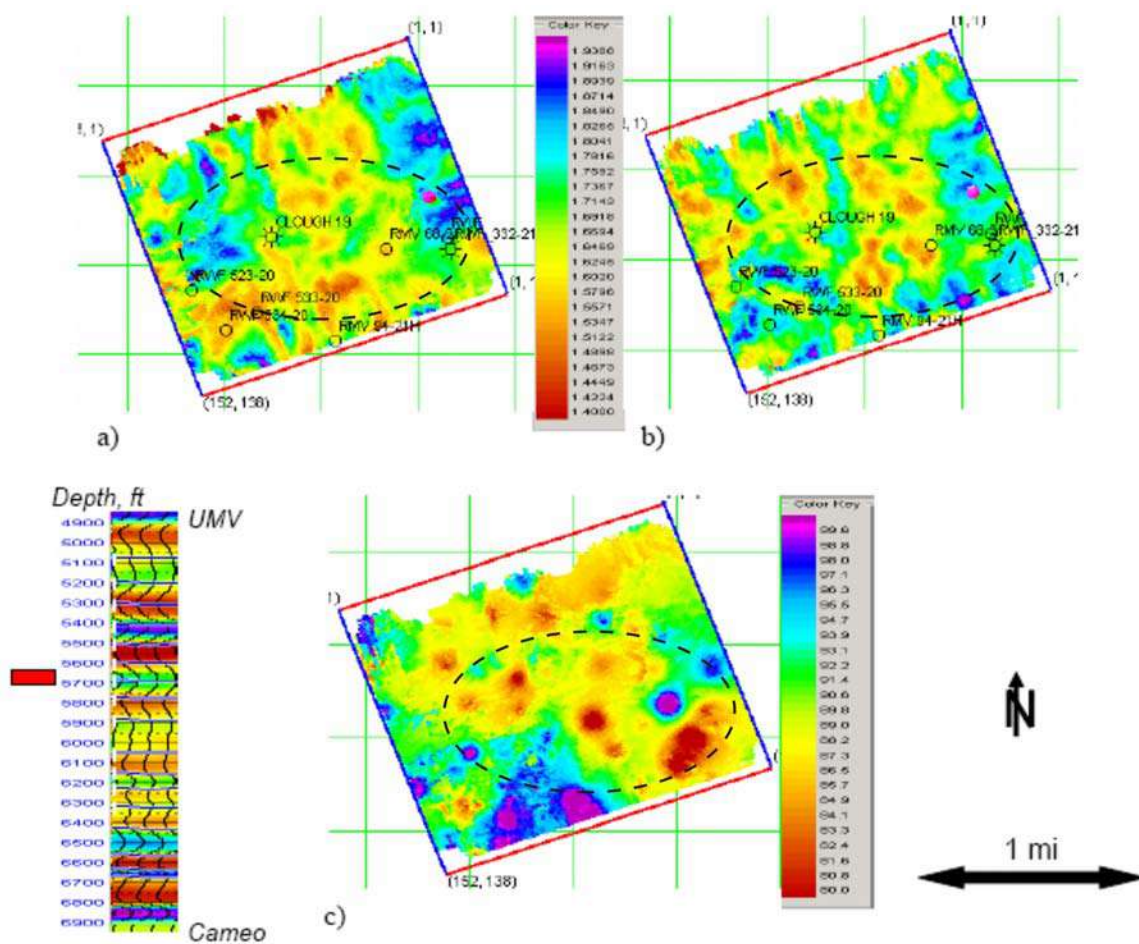


Figure 5.21 Depth interval slices generated within the 5600-5700 ft interval: a) Vp/Vs computed from PP-S11; b) Vp/Vs computed from PP-PS1; c) interpolated gamma ray model. The dashed ellipse outlines the seismic high fold coverage.

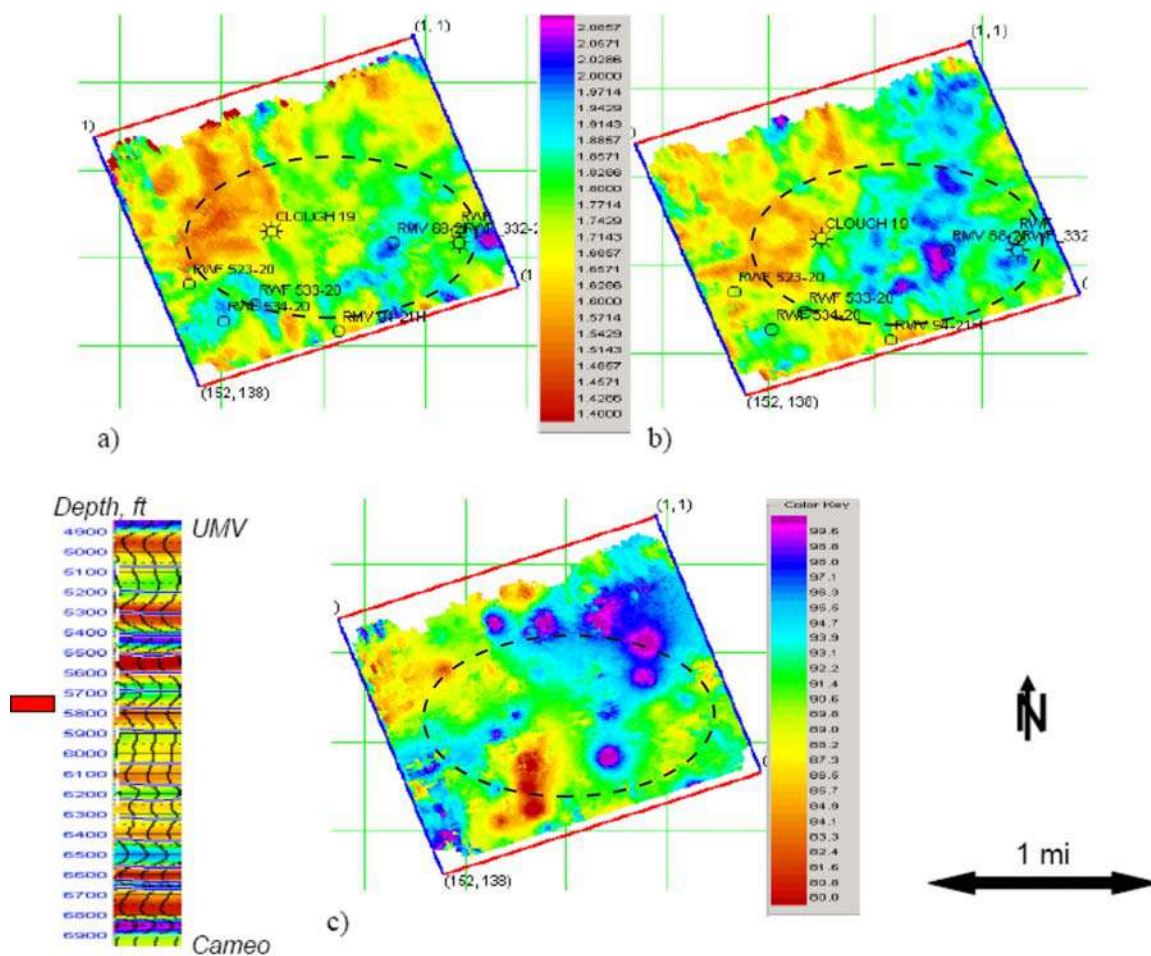


Figure 5.22 Depth interval slices generated within the 5700-5800 ft interval: a) Vp/Vs computed from PP-S11; b) Vp/Vs computed from PP-PS1; c) interpolated gamma ray model. The dashed ellipse outlines the seismic high fold coverage.



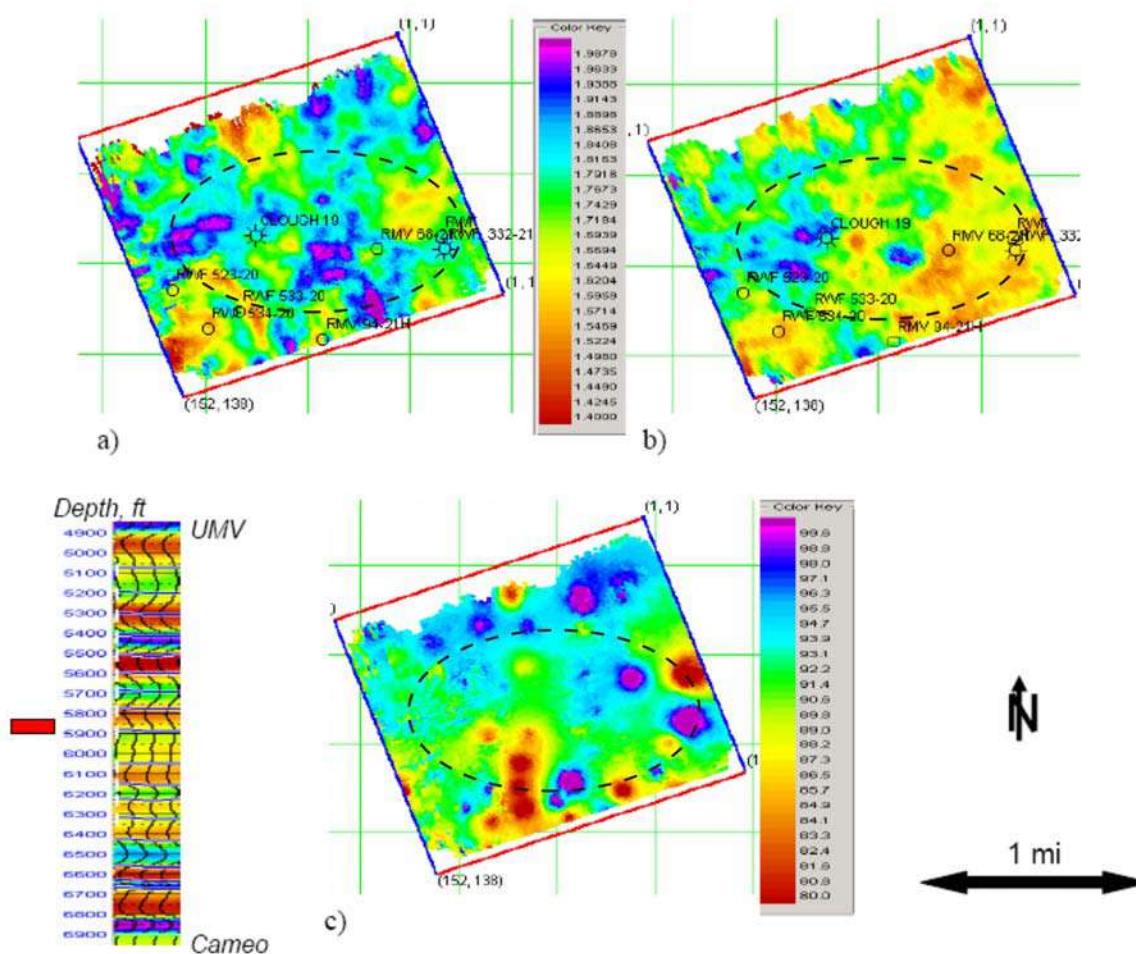


Figure 5.23 Depth interval slices generated within the 5800-5900 ft interval: a) Vp/Vs computed from PP-S11; b) Vp/Vs computed from PP-PS1; c) interpolated gamma ray model. The dashed ellipse outlines the seismic high fold coverage.

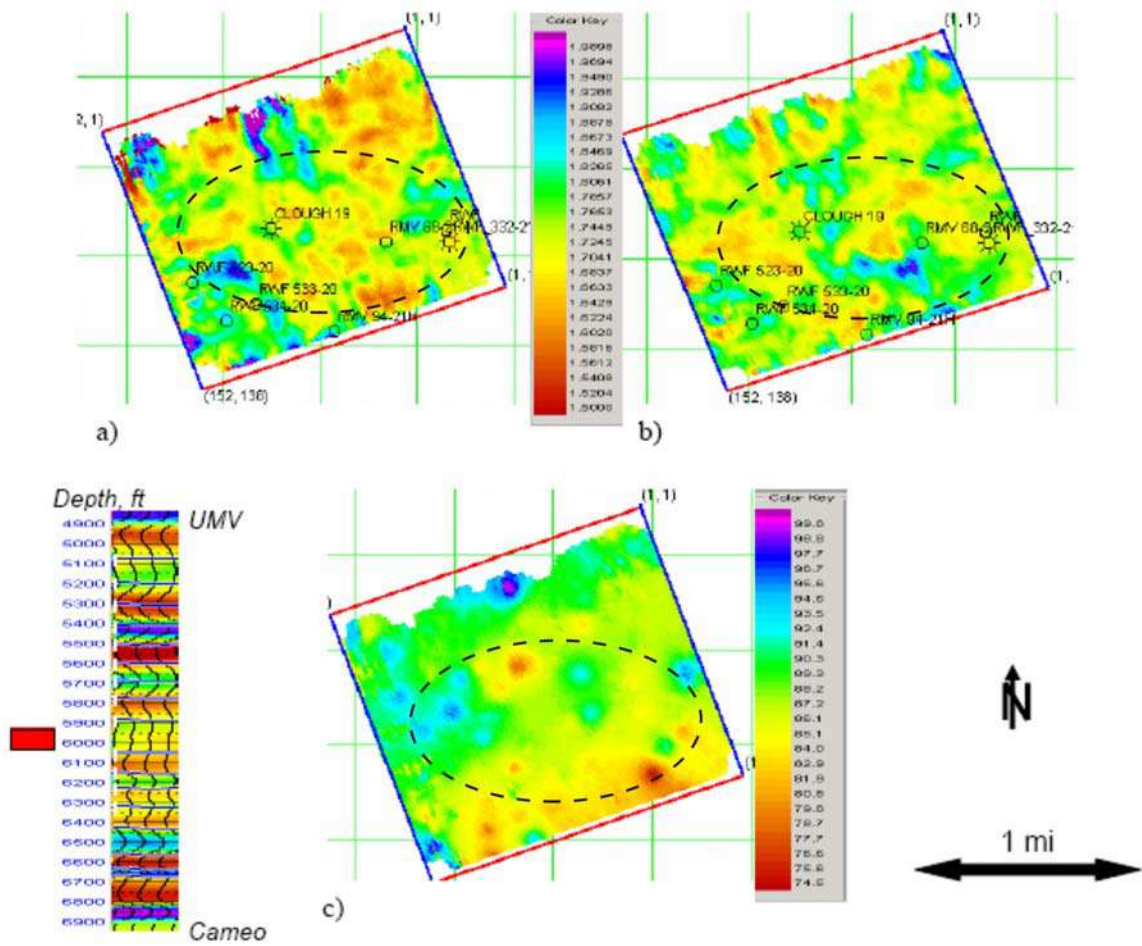


Figure 5.24 Depth interval slices generated within the 5900-6050 ft interval: a) Vp/Vs computed from PP-S11; b) Vp/Vs computed from PP-PS1; c) interpolated gamma ray model. The dashed ellipse outlines the seismic high fold coverage.

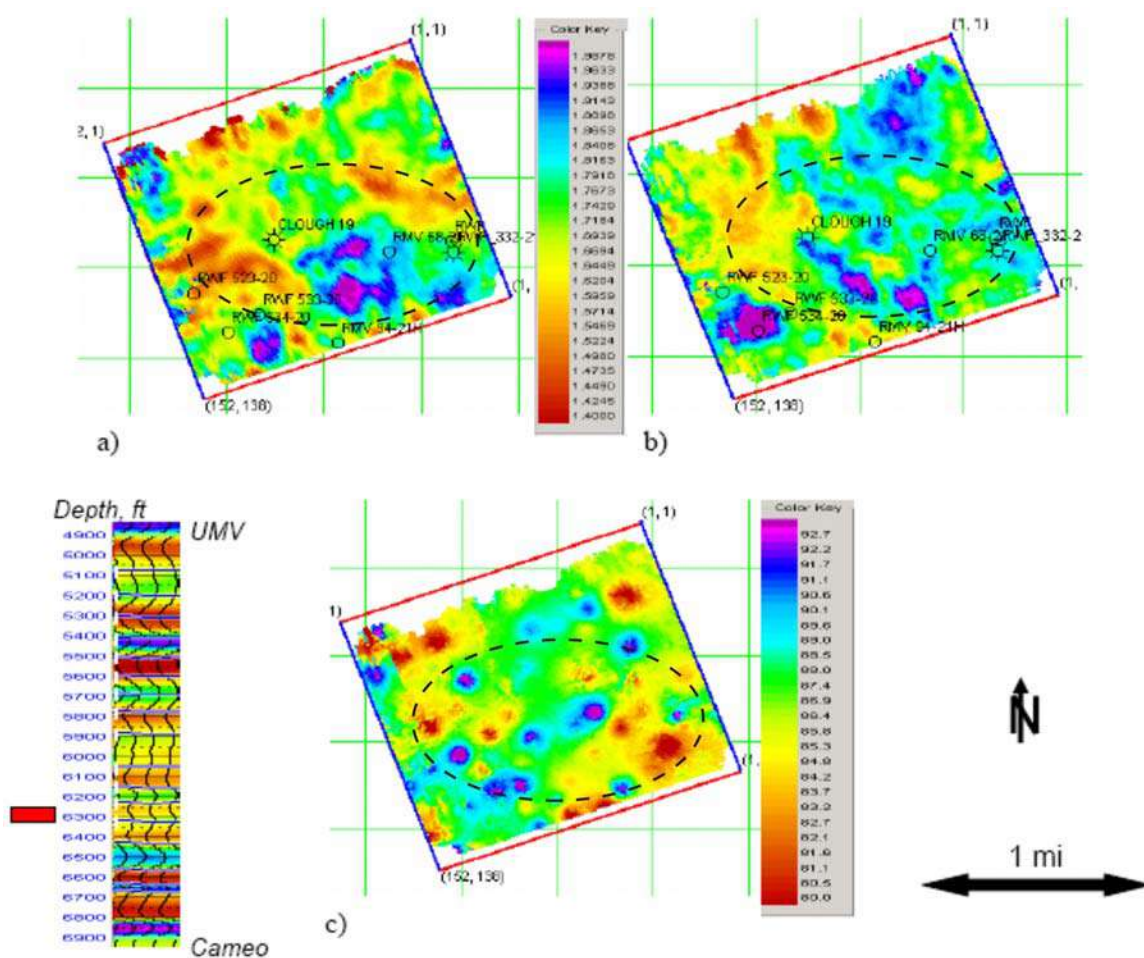


Figure 5.25 Depth interval slices generated within the 6200-6300 ft interval: a) Vp/Vs computed from PP-S11; b) Vp/Vs computed from PP-PS1; c) interpolated gamma ray model. The dashed ellipse outlines the seismic high fold coverage.

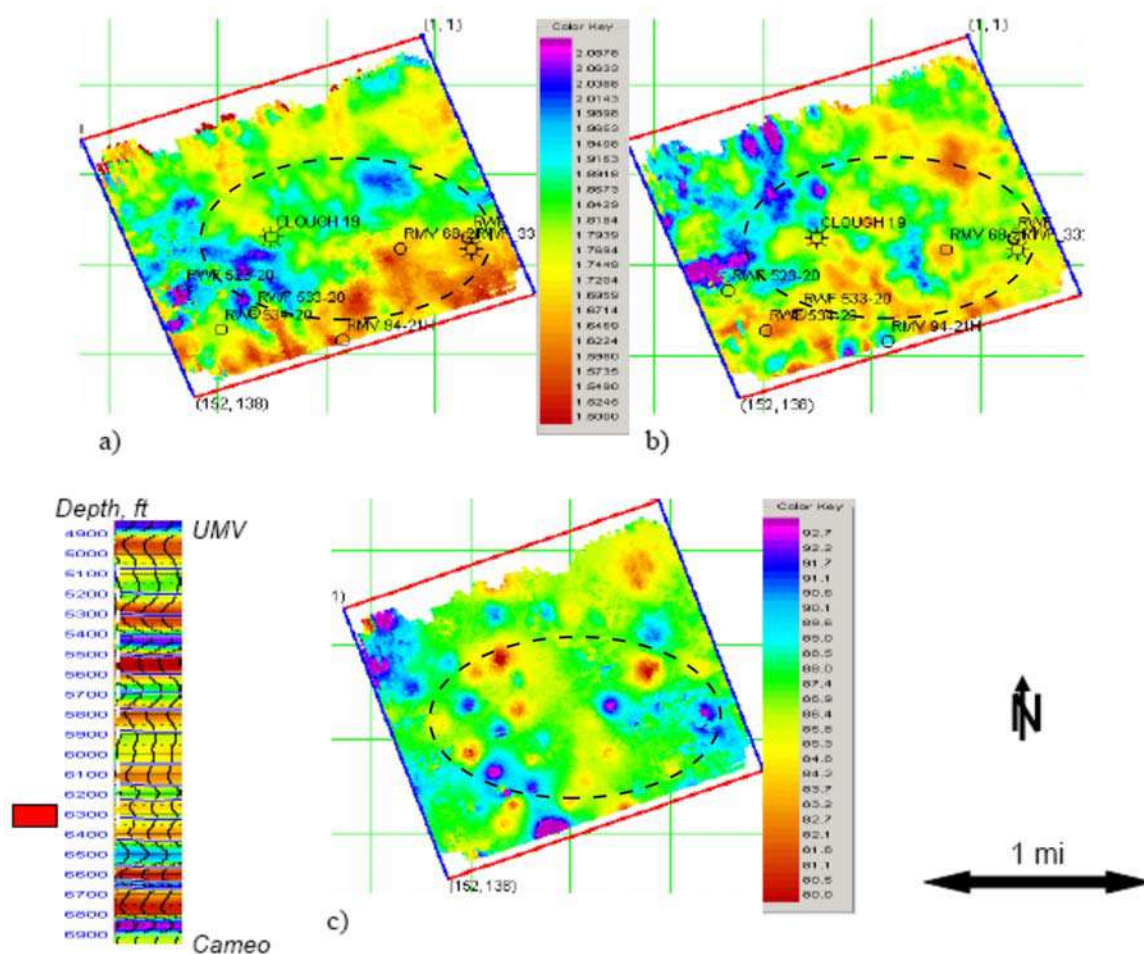


Figure 5.26 Depth interval slices generated within the 6300-6400 ft interval: a) Vp/Vs computed from PP-S11; b) Vp/Vs computed from PP-PS1; c) interpolated gamma ray model. The dashed ellipse outlines the seismic high fold coverage.

### **5.3.6 Prospect Identification**

The presented data in conjunction with 3-D viewing can help an interpreter identify prospects. Simultaneous interpretation of Vp/Vs volumes, time-lapse observations and well log data provides confident and informative results. Gas filled sandstones under overpressure conditions at Rulison field are responsible for abnormally low Vp/Vs and low gamma ray. Concurrently, it is expected to see no changes on time-lapse maps within bypassed zones.

I study the possible bypass pay around two investigated wells: RWF 332-21 and RWF 441-20. Figure 5.27 is a snapshot of a 3-D section demonstrating Vp/Vs inline and crossline represented by PP-S11 and PP-PS1 data combinations. The shown curve is gamma ray log registered in well RWF 332-21. The left deviation of the curve corresponds to the low API numbers. The time section is the percent difference in acoustic impedance calculated between 2003 and 2004. The maximum percent shown is 3% of changes. A closer look up at the segment between these three slices is shown in Figure 5.28. The area of interest is at vertical time of 961 ms, which is 5500 ft in depth equivalent. It can be noticed that at this depth the well penetrates the zone where no time-lapse anomalies are present. In Figure 5.29 is the same interval shown in terms of generated Vp/Vs volumes. Both data sets reveal Vp/Vs values below 1.6. Considering all these facts the conclusion can be made that the studied zone contains production potential.

Well RWF 441-20 is located in the middle of the survey, in the high fold area. At 1050 ms of vertical time, corresponding to approximately 6228 ft, the gamma ray log discloses low API value (Figure 5.30), permeating also the zone of low percent of impedance difference (Figure 5.31). Excluding the horizontal section in Figure 5.32, it also noticeable that the area is well corresponding to low Vp/Vs identified from both PP-S11 and PP-PS1 data sets.

Demonstrated are examples of applicable combination of the obtained and available data for bypass pay zones identification. A proper, with utilization of 3-D



viewing software, and thorough analysis of Vp/Vs cubes with incorporation of all available data assists in detecting and discovering new drilling targets.

#### **5.4 Summary**

This chapter is focused on the applications of the traveltimes and impedance derived Vp/Vs volumes. Both estimations fulfill a task of reservoir characterization.

It is important to study the volumetric changes of Vp/Vs properties in a 3-D perspective. This allows me to look at the reservoir sandbodies and their connectivity. Remembering the highly heterogeneous conditions in the reservoir, the tool of slicing the volumes provides essential information. The research confirms the applicability of Vp/Vs as a tool for exploration and development of tight gas sands. Good correlation is established between sandstone rich overpressured zones, as detected from gamma ray model, and zones with low Vp/Vs. The bypassed zones and depth intervals are detected by means of Vp/Vs analysis and confirmed by independently estimated time-lapse anomalies volumes.

The Vp/Vs results from both SS and PS wave reflection data verify the interpretation results and contribute to better understanding of the complex geology at Rulison.

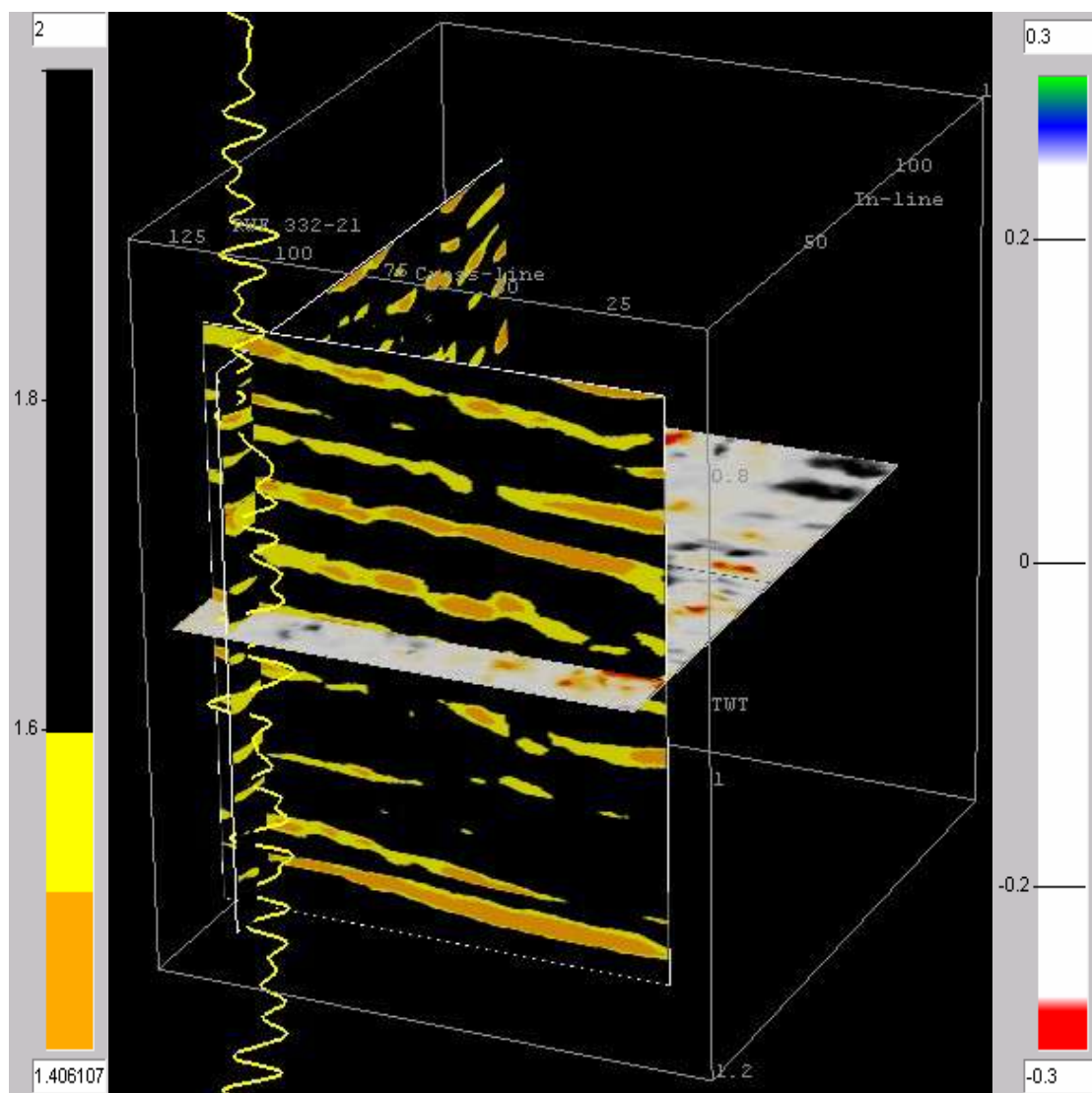


Figure 5.27 A prospect identified around well RWF 332-21 at depth 5500 ft. The vertical sections are represented by  $V_p/V_s$  values below 1.6, where inline is PP-S11 and crossline – PP-PS1 data sets. The horizontal section is percent impedance time-lapse change. The curve displays gamma ray log registered in the well.

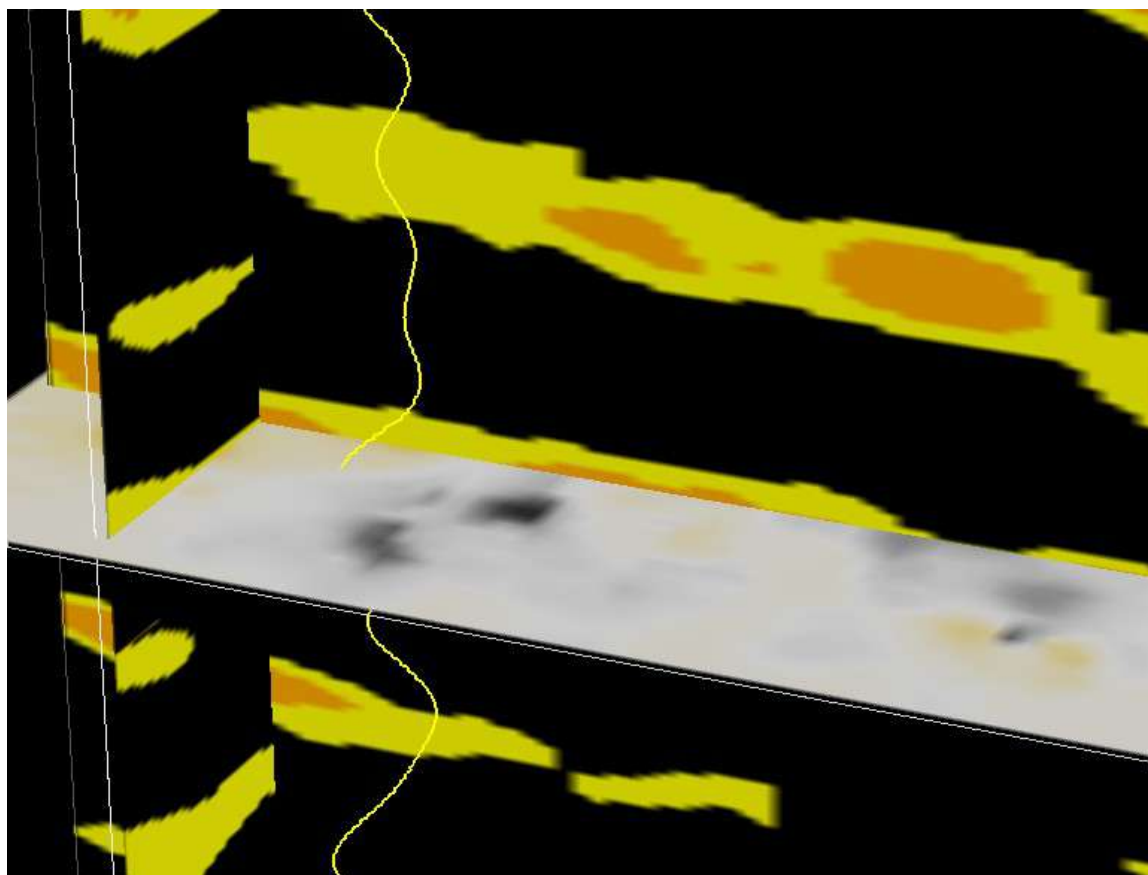


Figure 5.28 The zoomed in segment of well RWF 332-21, showing deviation of gamma ray curve towards lower values in the area of zero impedance change.



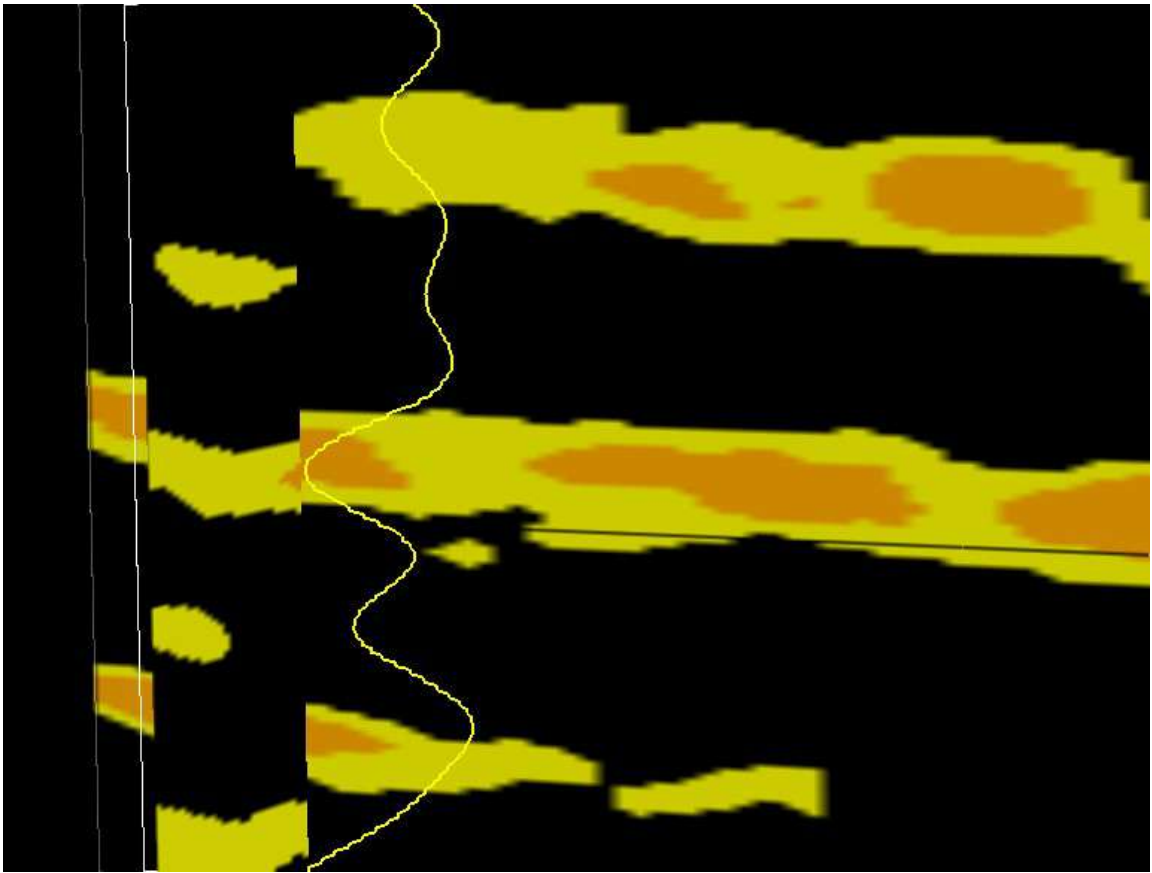


Figure 5.29 Abnormally low  $V_p/V_s$  values are very well correlated with low gamma ray from RWF 332-21 in the zone of interest.

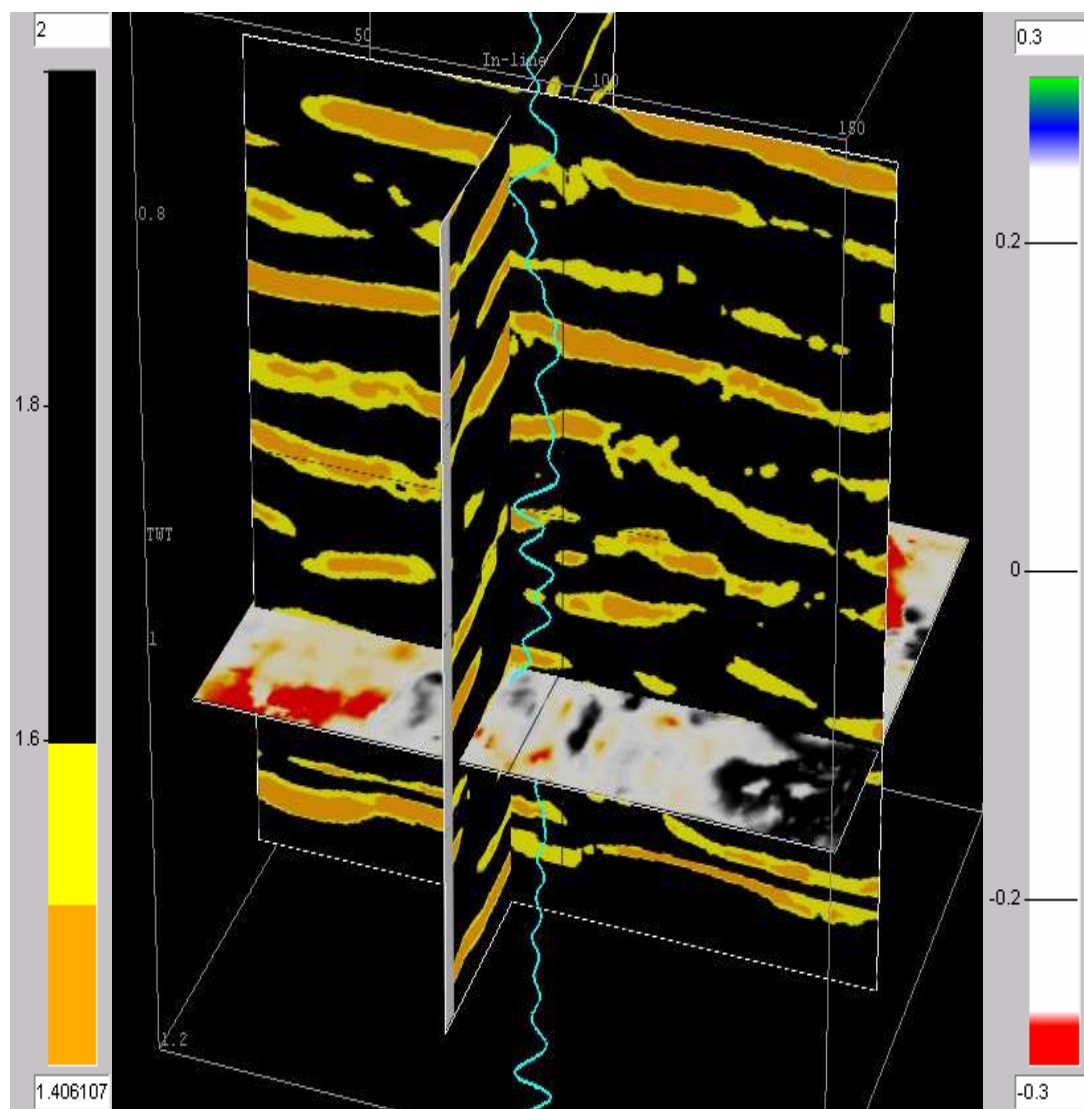


Figure 5.30 A prospect identified around well RWF441-20 at depth 6228 ft. The vertical sections are represented by  $V_p/V_s$  values below 1.6, where inline is PP-S11 and crossline – PP-PS1 data sets. The horizontal section is percent impedance time-lapse change. The curve displays gamma ray log registered in the well.

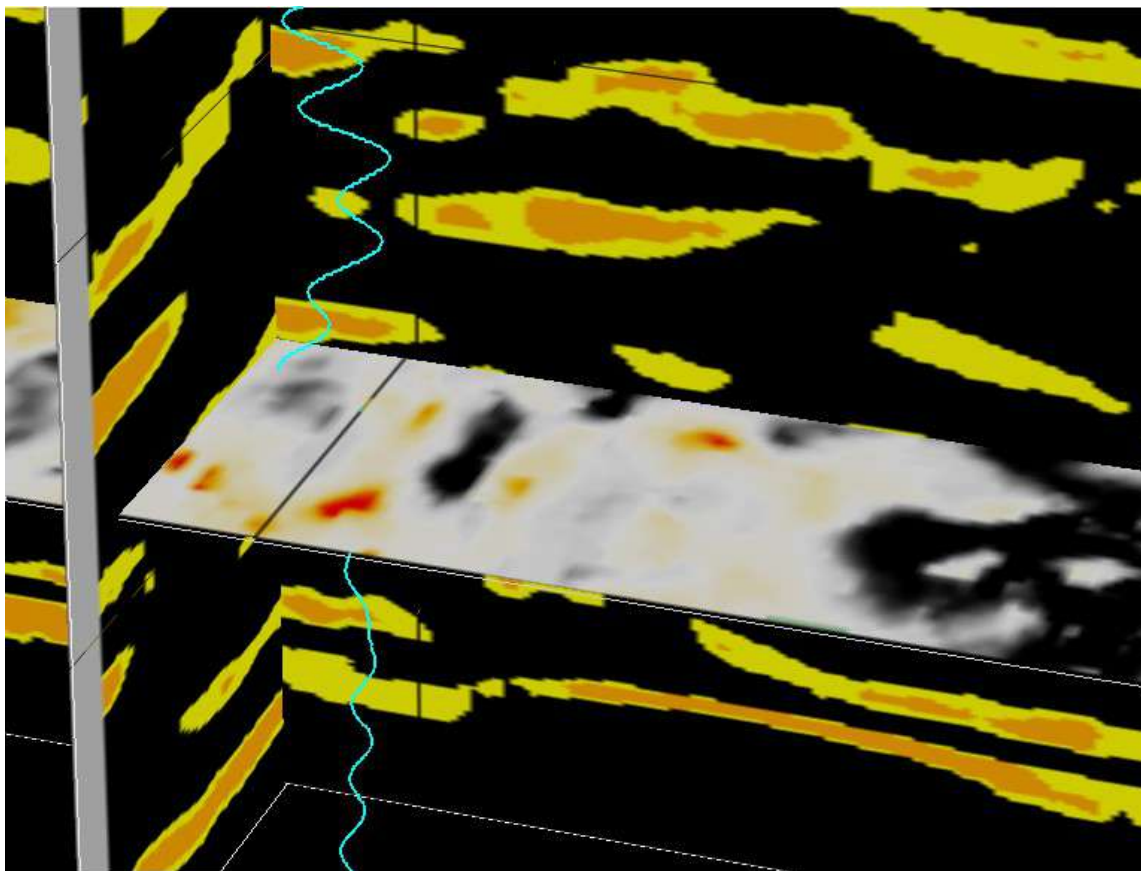


Figure 5.31 The zoomed in segment of well RWF 441-20, showing deviation of gamma ray curve towards lower values in the area of zero impedance change.

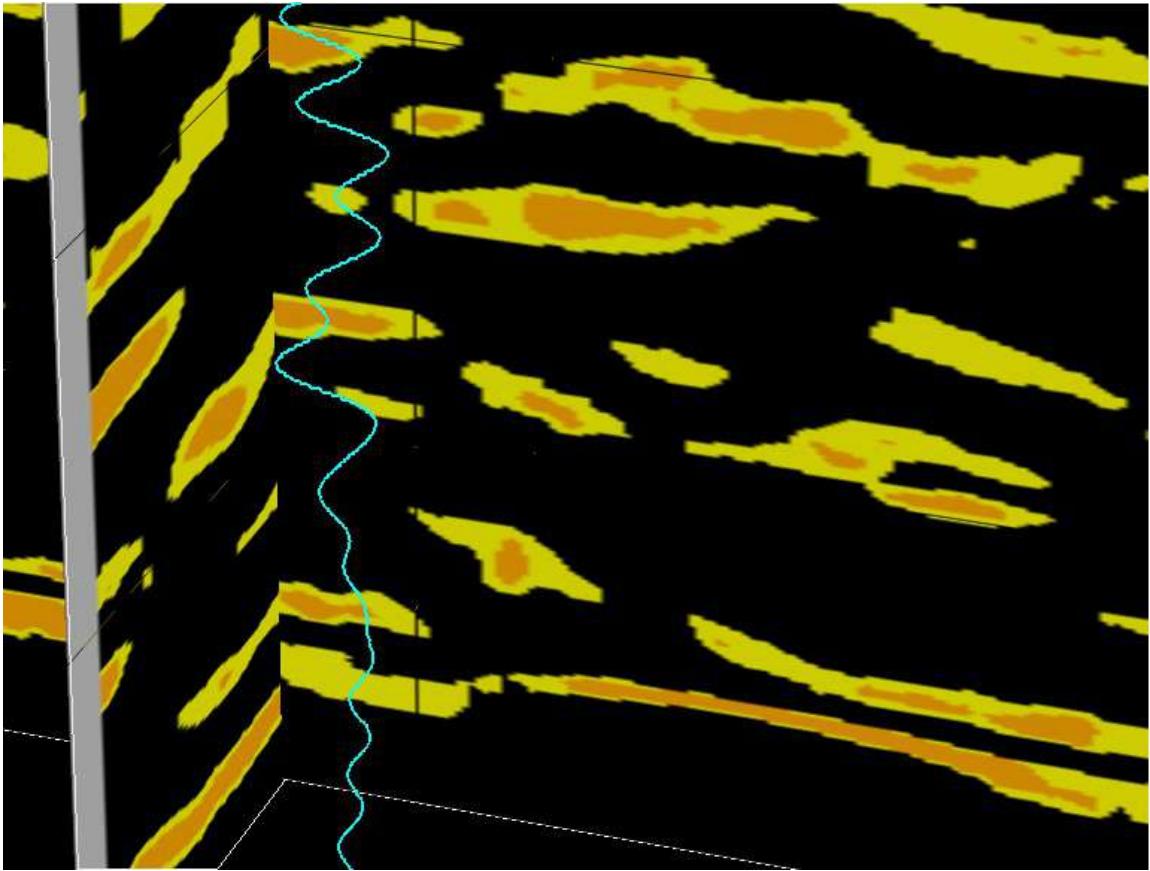


Figure 5.32 Abnormally low  $V_p/V_s$  values are very well correlated with low gamma ray from RWF 441-20 in the zone of interest.

## Chapter 6

### CONCLUSIONS AND RECOMMENDATIONS

#### **6.1 Conclusions**

From the results of applied workflow and simultaneous use of multicomponent data combinations (PP-SS and PP-PS), I draw the following conclusions:

- a) The process of  $V_p/V_s$  estimation must be performed in the time domain. The workflow for high resolution  $V_p/V_s$  estimation, I present in the research requires two input data volumes with an equivalent vertical scale. Naturally, the depth domain can be more attractive, since the final results must be viewed in depth. However, my conclusion is that it is harder and involves more uncertainties to estimate velocity volumes needed to convert seismic data from the original time domain to depth. Basically, I suggest using the original domain of the seismic data through the inversion steps and then depth converting the  $V_p/V_s$  cube.
- b) The results of impedance derived  $V_p/V_s$  reveal a good correlation with log derived data. The generated high resolution  $V_p/V_s$  can always be tied back to the wells to assess the accuracy and quality of the results. I obtain correlation coefficients of more than 0.60 for the middle part of the reservoir where most of the production is concentrated.

The ramifications of my work:

- 1) The integration of both pure S-wave and converted PS-wave data increases the interpretability and reliability of  $V_p/V_s$  results. I derive this statement from interpretation of obtained  $V_p/V_s$  volumes in Chapter 5. If two data sets reveal the

same feature on Vp/Vs maps within the same interval a more confident deduction can be made.

- 2) There is a direct correlation between Vp/Vs and reservoir quality in Rulison field. I show the dependence of Vp/Vs results on lithology. Cleaner sandstones exhibit lower Vp/Vs values.
- 3) The analysis of low Vp/Vs, time-lapse anomalies and log data enables me to identify bypassed zones. This ramification from the main conclusions is motivated by the results of 3-D representation of the Vp/Vs volume and its comparison with time-lapse observations.
- 4) Three dimensional estimates of Vp/Vs enable me to project the potential connectivity of the tight gas sandstones. Resultant Vp/Vs volumes viewed and analyzed in 3-D bring more information for better well planning.

## **6.2 Recommendations for future research**

My proposal for future work includes:

- Implementation of the workflow for Vp/Vs computation from slow pure and converted shear wave data. The combinations of PP-S22 and PP-PS2 may be useful for depicting changes of the reservoir properties due to fracturing.
- The characterization of the deeper reservoir portion. This study is focused on reservoir interval above the Cameo (5700 - 7400 ft of depth) consisting of irregularly shaped, stacked channel sandstones. Future research should cover the deeper interval (7400 - 8000 ft), which is characterized by distributary channel sandstones and Cameo coal layers.
- Study of the sensitivity of Vp/Vs to depletion of the reservoir during production by means of Vp/Vs time-lapse monitoring. Production alters reservoir parameters, specifically fluid pressure. The drop in pressure can be detected and perhaps quantified by velocity ratio mapping.

- Development of the geological reservoir model through the implementation of statistical methods using Vp/Vs volume as a background model.

## APPENDIX A

### PSEUDO DENSITY DERIVATION FOR STRATIGRAPHIC INVERSION OF POSTSTACK PS CONVERTED WAVE DATA

#### **A.1 Reflectivity approximation for near offset PS data**

By assuming that changes in elastic properties of rocks across the layer boundary are small and propagation angles are within the subcritical range, Aki and Richards (1980) approximated PS reflection coefficient as

$$R_{PS} = -\frac{V_P}{2V_S} \tan \psi \left[ A \frac{\Delta \rho}{\rho} - B \frac{\Delta V_S}{V_S} \right], \quad (\text{A.1})$$

where coefficients

$$A = 1 - 2 \frac{V_S^2}{V_P^2} \sin^2 \theta + 2 \frac{V_S}{V_P} \cos \theta \cos \psi \quad (\text{A.2})$$

and

$$B = 4 \frac{V_S^2}{V_P^2} \sin^2 \theta - 4 \frac{V_S}{V_P} \cos \theta \cos \psi. \quad (\text{A.3})$$

The parameters included in these formulas are:

$V_P$  - P-wave velocity,



$V_s$  - S-wave velocity,

$\rho$  – density,

$\theta$  - incidence angle,

$\psi$  - emergence angle.

The terms  $\frac{\Delta\rho}{\rho}$  and  $\frac{\Delta S}{S}$  describe the fractional change in density and shear wave velocity correspondently. However, the parameters  $\Delta V_s$  and  $\Delta\rho$  must be small to validate the approximation for PS reflectivity.

According to Snell's law,

$$\sin \theta = \frac{V_P}{V_S} \sin \psi , \quad (\text{A4})$$

incidence angle can be expressed through the corresponding emergence one. Then, for purely isotropic media and small emergence angle, only the linear terms in  $\sin\psi$  are kept. Thus, coefficients A and B can be rewritten as:

$$A = 1 + 2 \frac{V_S}{V_P} \cos \psi , \quad (\text{A.5})$$

$$B = -4 \frac{V_S}{V_P} \cos \psi . \quad (\text{A.6})$$

Substituting equations A.5 and A.6 into equation A.1 and performing some arithmetic operations, the last can be written as

$$R_{PS} \approx -\frac{V_P}{2V_S} \tan \psi \frac{\Delta \rho}{\rho} - \sin \psi \frac{\Delta \rho}{\rho} - 2 \sin \psi \frac{\Delta V_S}{V_S}, \quad (\text{A.7})$$

or, assuming for small angle  $\tan \psi = \sin \psi$ ,

$$R_{PS} = -2 \sin \psi \left[ \left( \frac{1}{4} \frac{V_P}{V_S} + \frac{1}{2} \right) \frac{\Delta \rho}{\rho} + \frac{\Delta V_S}{V_S} \right]. \quad (\text{A.8})$$

When the traces are stacked for the same range of angles, the angle term becomes constant and can be factored out.

$$R_{PS[\text{stack}]} = -2 * \left[ \left( \frac{1}{4} \frac{V_P}{V_S} + \frac{1}{2} \right) \frac{\Delta \rho}{\rho} + \frac{\Delta V_S}{V_S} \right] * \sum \sin \psi, \quad (\text{A.9})$$

where  $\sin \psi$  is the range of angles for one CCP gather.

## **A.2 Pseudo density derivation**

Reflection coefficient of compressional wave data for normal incidence angle can be expressed as

$$R_{PP} = 2 \left[ \frac{\Delta \rho}{\rho} + \frac{\Delta V_P}{V_P} \right] \quad (\text{A.10})$$

Both equations A.8 and A.10 represent similar dependence of PS- and PP-wave reflectivity on velocity and density, but a different relationship exists with those parameters. Pseudo density is the quantity that brings equivalent to the fractional changes of density for PP- and PS-wave data:

$$\frac{\Delta\rho}{\rho} = \left( \frac{1}{4} \frac{V_p}{V_s} + \frac{1}{2} \right) \frac{\Delta\rho}{\rho} . \quad (\text{A.11})$$

If  $\frac{\Delta\rho}{\rho} = \log \rho$ , then

$$\hat{\rho} = \rho^{\left( \frac{1}{4} \frac{V_p}{V_s} + \frac{1}{2} \right)} , \quad (\text{A.12})$$

where

$\hat{\rho}$  - pseudo density

$\rho$  - original density

## REFERENCES

- Aki, K., and Richards, P. G., 1980, Quantitative seismology: theory and methods: W. N. Freeman & Co.
- Anderson, D. L., and Liberman, R. C., 1996, Sound velocities in rocks and minerals: VESIAC state-of-the-art report: 885-4-X, University of Michigan, Ann Arbor.
- Benzing, W. M., 1978, Vs/Vp relationships in carbonates and sandstones – laboratory data: Presented at the 48<sup>th</sup> Annual International Meeting, SEG.
- Castagna, J. P., Batzle, M. L., and Eastwood, R. L., 1985, Relationships between compressional-wave and shear-wave velocities in elastic silicate rocks: *Geophysics*, 50, p. 571-581.
- Cole, R. M., and Cumella, 2003, Stratigraphic architecture and reservoir characteristics of the Mesaverde Group, southern Piceance Basin, Colorado, *in* K.M. Peterson, T.M. Olson, and D.S. Anderson, eds., *Piceance Basin 2003 Guidebook*: Denver RMAG, p. 385-442.
- Colorado Oil and Gas Conservation Commission (COGIS) Web site. 2005. COGIS – Production Data Inquiry.  
<http://oil-gas.state.co.us/>
- Crampin, S., 1978, Seismic-wave propagation through a cracked solid: Polarization as a possible dilatancy diagnostic: *Geophys. J.R. Astr. Soc.*, 53, p. 467-496.

- Domenico, S. N., 1976, Effect of brine-gas mixture on velocity in an unconsolidated sand reservoir: *Geophysics* 41, p. 882-894.
- Domenico, S. N., 1984, Rock lithology and porosity determination from shear and compressional wave velocity: *Geophysics* 49, p. 1188-1195.
- Ensley, R. A., 1984, Comparison of P- and S-wave seismic data: A new method for detecting gas reservoirs: *Geophysics* 49, p. 1420-1431
- Franco, G., 2006, Rock physics measurements for estimate anisotropy parameters in tight gas sand reservoirs: *The Reservoir Characterization Project Report*, 72 - 80.
- Geyer, R. L., and Martner, S. T., 1969, SH waves from explosive sources: *Geophysics*, 34, 893-905
- Hamilton, E. L., 1972, Compressional-wave attenuation in marine sediments: *Geophysics*, 37, 620-646.
- Hamilton, E. L., 1979,  $V_p/V_s$  and Poisson's ratio in marine sediments and rocks: *J. Acoustic Soc. Am.*, 66, 1093-1101.
- Hemborg, H. T., 2000. Gas Production Characteristics of the Rulison, Grand Valley, Mamm Creek, and Parachute Fields, Garfield County, Colorado: Turning Marginally Economic Basin-Centered Tight-Gas Sands into Profitable Reservoirs in the Southern Piceance Basin: Colorado Geological Survey, Resource Series 39, p. 1-30.

- Henry, S. G., 1997, Catch the (seismic) wavelet; Geophysical corner, online source: <http://www.searchanddiscovery.net/documents/geophysical/henry/images/henry.pdf>
- Jensen K., 2005, Seismic Investigation Of Wrench Faulting And Fracturing At Rulison Field, Colorado: MS thesis, Colorado School of Mines.
- Johnson, R. C., Crovelli, R. A., Spencer, C. W., and Mast, R. F., 1987, An Assessment of Gas Resources in Low-Permeability Sandstones of the Upper Cretaceous Mesaverde Group, Piceance Basin, Colorado: USGS Open-File Report 87-357.
- Johnson, R. C., 1989. Geologic history and hydrocarbon potential of Late Cretaceous-age, low-permeability reservoirs, Piceance Basin western Colorado: U. S. Geological Survey Bulletin 1787-E, 51 p.
- Johnson, R. C., and Roberts, S. B., 2003 The Mesaverde total petroleum system, Uinta-Piceance province. Utah and Colorado (Chapter 7), in Petroleum systems and geologic assessment of oil and gas in the Uinta-Piceance province. Utah and Colorado: USGS Digital Data Series DDS-69-B. 68 p.
- Kithas, B. A., 1976, Lithology, as detection and rock properties from acoustic logging systems: Proc. Soc. Prof. Well Log Analysis 17<sup>th</sup> Annual Logging Symposium, R1-Q10.
- Krishnamurthi, M., and Balakrishna, S., 1953, Proceedings of the Indian Academy of Sciences, 38A, 498-501.

- Kuuskraa, A. Vello, David Decker, and Heloise Lynn 1997. Optimizing Technologies for Detecting Natural Fractures in the Tight Sands of the Rulison Field, Piceance Basin. Publication of the National Energy Technology Laboratory, web site: [http://www.netl.doe.gov/publications/proceedings/97/97ng/ng97\\_pdf/NG6-3.PDF](http://www.netl.doe.gov/publications/proceedings/97/97ng/ng97_pdf/NG6-3.PDF)
- Lo, T., Coyner, K. B., and Toksöz, M. N., 1986, Experimental determination of elastic anisotropy of Berea sandstone, Chicopee shale, and Chelmsford granite: *Geophysics*, 51, p. 164-171.
- Lorenz, J. C., Heinze, D. M., Clark, J. A., Searls, C. A., 1985, Determination of widths of meander-belt sandstone reservoirs from vertical downhole data. *Mesaverde Group. Piceance Creek Basin, Colorado: AAPG Bulletin*, v.69. p.710-721.
- Magoon, L. B., and Dow, W. G., 1994, The petroleum system - from source to trap: *AAPG Memoir* 60, p. 3-24.
- McDonal, F. J., Angona, F. A., Mills, R. L., Sengbush, R. L., Van Nostrand, R. G., and White, J. E., 1958, Attenuation of shear and compressional waves in Pierre shale: *Geophysics*, 23, 421-439.
- McFall, K. S., Wicks, D. E., Kruuskraa, V. A., and Sedwick, K. B. 1986. A geologic assessment of natural gas from coal seams in the Piceance Basin, Colorado. Gas Research Institute, Topical Report. GRI-87/0060 (September 1985-September 1986), 76 p.
- Nations, J. F., 1974, Lithology and porosity from acoustic shear and compressional wave transit-time relationships: *Proc. Soc. Prof. Well Log Analysis 15<sup>th</sup> Annual Logging Symposium*, Q1-Q16

- Pickett, G. R., 1963, Acoustic character logs and their application in formation evaluation: J. Pet. Tech., p. 659-667.
- Reinecke, Kurt M., Rice, D. D., and Johnson, R. C., 1991, Characteristics and development of fluvial sandstone and coalbed reservoirs of Upper Cretaceous Mesaverde Group, Grand Valley field, Colorado: Guidebook for the Rocky Mountain Association of Geologists Fall Conference and Field Trip September, 17-20, 1991, Rocky Mountain Association of Geologists Denver, Colorado, pp. 209-225.
- Rojas, E., 2005, Elastic rock properties of tight gas sandstones for reservoir characterization at Rulison field, Colorado: MS thesis, Colorado School of Mines.
- Rumon, M. D., 2006, Shear wave time-lapse seismic monitoring of a tight gas sandstone reservoir, Rulison field, Colorado: MS thesis, Colorado School of Mines.
- Russell, B. H., 1988, Introduction to Seismic Inversion Methods: Course Notes Series, No. 2, Society of Exploration Geophysicists.
- Russell, B. H., 2005, Seismic Inversion and AVO: Presented at the Denver Geophysical Society.
- Scales J. A., Smith M. L., and Treitel S., 1997, Introductory Geophysical Inverse Theory: Samizdat Press Publication, online source - <http://samizdat.mines.edu>



Scheevel, J., and Cumella, S. P., 2005, Stratigraphic and rock mechanics control of Mesaverde gas distribution. Piceance Basin, Colorado (abs.): RMAG PTTC Fall Symposium. Low Permeability Reservoirs in the Rockies. August 29, 2005. Denver Colorado.

Spencer, C. W., 1989, Review of characteristics of low-permeability gas reservoirs in the western United States: American Association of Petroleum Geologists Bulletin, v. 73, p. 613-629.

Stewart, R., 1991, Rapid map and inversion of P-SV waves: Geophysics, 56, p. 859-862

Tatham, R. H., McCormack, M. D., 1991, Multicomponent seismology in petroleum exploration: Society of Exploration Geophysicists

TICORA Geosciences, Inc. Web site. 2002. Basin of the Month.  
<http://www.ticora.com/cbmalerts/CBMAAlertJanuary2002.pdf>

Timur, A., 1977, Temperature dependence of compressional and shear wave velocities in rocks: Geophysics, 42, p. 950-956.

Toksöz, M. N., Cheng, C. H., and Timur, A., 1976, Velocities of seismic waves in porous rocks: Geophysics, 41, p. 621-645.

Tosaya, C. A., Nur, A. M. and Daprat, G., 1984, Monitoring of thermal EOR fronts by seismic methods: Proceedings 1984 Int. Reg. Mtg, Soc. Petr. Eng. SPE #12744.

Valenciano, A. A., and Michelena, R. J., 2000, Stratigraphic inversion of poststack PS converted waves data: SEG Technical Program Expanded Abstracts, pp. 150-153

Vargas, M. F., Pranter, M. J., Davis, T. L., 2006, Characterization and 3-D Reservoir Modeling of Fluvial Tight-Gas Sandstones in the Williams Fork Formation, Rulison Field, Piceance Basin, Colorado, USA: AAPG Technical Program Abstract. Online source:  
<http://aapg.confex.com/aapg/2006am/techprogram/A100622.htm>

U.S. Geological Survey Digital Data Series 69-B, 2005, National Assessment of Oil and Gas Project: Petroleum Systems and Geologic Assessment of Oil and Gas in the Uinta-Piceance Province, Utah and Colorado, web site:  
[http://pubs.usgs.gov/dds/dds-069/dds-069-b/OPEN\\_FIRST/69B\\_MAIN\\_CONTENTS.pdf](http://pubs.usgs.gov/dds/dds-069/dds-069-b/OPEN_FIRST/69B_MAIN_CONTENTS.pdf)

Wood, A. B., 1949, Textbook of sound: G. Bell and Sons, Ltd., 361-362.

Yilmaz Ö., 2001, Seismic Data Analysis: Society of Exploration Geophysicists